Quantum Transport in Graphene Heterostructures

Andrea Franchini Young

Submitted in partial fulfillment of the requirements
for the degree of Doctor of Philosophy
in the Graduate School of Arts and Sciences

COLUMBIA UNIVERSITY
2012

ABSTRACT

Quantum transport in graphene heterostructures

Andrea Franchini Young

The two dimensional charge carriers in mono- and bilayer graphene are described by massless and massive chiral Dirac Hamiltonians, respectively. This thesis describes low temperature transport experiments designed to probe the consequences of this basic fact. The first part concerns the effect of the lattice pseudospin, an analog of a relativistic electron spin, on the scattering properties of mono- and bilayer graphene. We fabricate graphene devices with an extremely narrow local gates, and study ballistic carrier transport through the resulting barrier. By analyzing the interference of quasiparticles confined to the region beneath the gate, we are able to determine that charge carriers normally incident to the barrier are transmitted perfectly, a solid state analog of the Klein tunneling of relativistic quantum mechanics. The second part of the work describes the development of hexagonal boron nitride (hBN), an insulating isomorph of graphite, as a substrate and gate dielectric for graphene electronics. We use the enhanced mobility of electrons in hBN supported graphene to investigate the effect of electronic interactions. We find interactions drive spontaneous breaking of the emergent SU(4) symmetry of the graphene Landau levels, leading to a variety of quantum Hall isospin ferromagnetic (QHIFM) states, which we study using tilted field magnetotransport. At yet higher fields, we observe fractional quantum Hall states which show signatures of the unique symmetries and anisotropies of the graphene QHIFM. The final part of the thesis details a proposal and preliminary experiments to probe isospin ordering in bilayer graphene using capacitance measurements.

Contents

List of Figures

Acknowledgments

First and foremost, let me thank my advisor, Philip Kim, a kind and patient mentor and a living testament to the fact that you don't have to believe you are a great scientist to *be* a great scientist. You knew when to push me and when to give me an idea and leave me alone, and were always available to discuss physics despite a grueling schedule. I was always impressed by your ability to get the best work out of your other students, but it is only with the benefit of hindsight that I realize this applied equally to me.

I owe also a great debt of gratitude to Igor Aleiner. Igor has taught many generations of Columbia graduate students, me included, most of what we know about statistical mechanics and condensed matter theory. From you we learned many things we never could have gotten from the textbooks. Moreover, at two crucial points in my career, you gave me good advice: the first was to stay at Columbia for graduate school, and the second was to become an experimentalist. Staying at Columbia was an easy decision, but I did *not* want to be an experimentalist, and I owe you for having understood me better than I did at the time and put me on the right path. Since then you have been patient with my questions even when my problems have not directly interested you, and saved me countless hours of literature searching with your near- encyclopedic knowledge.

Starting from the beginning, let me thank my friends and fellow first and second year graduate students in physics, with whom I spent many late nights doing problem sets and studying for qualifying exams, among them Fabio Dominguez, Matt Toups, Aaron Angerami, Ivan Zalamea, Xiao-Yon Jun, Hong-Jun Ahn, Kyungeun Lim, and Ali Masumi. Thanks to Kin Fai Mak in particular, for having been a wonderful roommate, friend, and colleague. Discussing physics over 1AM pasta was a constant source of ideas.

My group mates and collaborators over the last five years have made working fun even in the darkest periods of seemingly hopeless experiments. Thanks Pablo and Barbaros, for an intense introduction to fabrication and the intricacies of science as a 'team sport.' Thanks Mike Purewal and Yuri Zuev for a fun first summer in the lab, and the free chess lessons. Thanks Melinda Han, for being a good friend and willing ear for ideas and complaints; the right side of my field of vision was never the same after you graduated. Thanks Dmitri Efetov; every kvetcher needs a partner, and you were a great one. And thanks Yue Zhao, Fereshte Ghahari, Vikram Deshpande, Young Jun Yu, Sebastian Sorgenfrei, Patrick Maher, and Carlos Forsythe. I've learned a lot by watching you all work in your diverse styles, and my time at Columbia would not have been the same without you.

I've had the good luck to have worked with a number of talented and enthusiastic undergraduates, among them Ethan Rosenthal, Hechen Ren, Arthur Tsoi, and Zach Kagan. All of you were fun to work with, and I learned more from working with each of you than you probably think. Zach, thanks for your enthusiasm and determination, and willingness to take on anything. Hechen,

thanks for being an equal partner through most of my time in the group–you were not only a second pair of hands but a second brain, much of the work in this thesis would not have happened without you.

Even as I type this thesis, I already miss the collaborative wonderland that is Columbia. Many of the key people in my life in the last years were from other groups and other departments, and for that I should perhaps thank the 7th floor triumvirate of Philip, Jim Hone, and Ken Shepard, as well as Tony Heinz, for creating a really unique environment for the study of graphene. Barriers to collaboration were basically null, and creativity was allowed at every level of the hierarchy—I never heard of someone being told to stop doing something they thought might work. It really felt like the center of the graphene world, and I appreciate the behind-the-scenes effort over many years that went in to making Columbia such a great place to study and work.

The most productive part of my thesis years was marked by the formation of a small subgroup of the Kim, Hone, and Shepard groups devoted to the development of graphene transfer and h-BN as a substrate for graphene devices. This group included Hechen Ren, Zach Kagan, Arthur Tsoi, Yuanda Gao, Tarun Chari, Wang Lei, Inanc Meric, and Cory Dean. Thanks for making that period immensely enjoyable, not just because it finally worked (remember, for a long time it didn't!) but because it was really fun to work with all of you. Thank you Lei, for your unique world view and sense of humor; working with you has always been interesting and you have shown me a new standard for patience and thoroughness. Inanc, I still have the impression that without you the entire NWC building would collapse into bits of tape and poorly soldered lengths of pipe. You are the type of person who multiplies the productivity of everyone around you (starting from me), and have been a wonderful colleague and friend.

Cory, you get your own paragraph. Our collaboration and friendship has been the defining event of my time as a PhD student, and I know this will not be the end of our relationship, professionally and otherwise. Thanks for turning me into a 'real experimentalist.' What I learned from you extends beyond the lathe, mill, and soldering iron; you taught me to *think* like an experimentalist, and that experiments are only hard until they are easy. Thanks, more materially, for having been the driving force behind graphene transfer, hBN, and all that followed and will follow. You are modest, and would probably disagree, but without you that revolution would not have happened and I feel smart for having figured early that I should tag along and contribute what I could. The last few years have been full of exciting physics and free of interpersonal conflicts; I'll be lucky to happen on so perfect a collaboration again.

Finally, I want to thank a few collaborators ranging farther afield, all of which have been patient with my often naive inquiries. I should thank in particular Leonid Levitov and his group at MIT, including Mark Rudner, Nan Gu, and Andrei Shytov. Thanks, Leonid, for taking the time to look at our data; your ability to look at experimental data without prejudices is incredible, and has certainly been fun and productive for me. Thanks also to Matt Foster, a patient mentor during my ill-fated theorist days and someone to whom I could always come to with questions, no matter how stupid. Most recently thanks Maxim Kharitonov for taking lots of time with me and the graphene quantum Hall ferromagnet. Thank you also to Ping Xie and Charlie Lieber at Harvard for providing the silicon nanowires and patiently putting up with my attempts to work with them.

The highlights of my education have been the relationships I have formed in my (long!) time in New York. Thank you to everyone who helped me along the way. Luckily, the world is not so large a place, and I look forward to the continuations of friendships and collaborations formed at

Columbia.

New York, New York Andrea Young

To my parents

Chapter 1

Introduction

1.1 Overview and outline

Since I began the work described in this thesis, the field of 'graphene research' has grown so diverse as to make the term almost meaningless. In large part the field has been driven by exciting possibilities for applications, which span a wide technological spectrum from analog radio frequency electronics[1] to substrates for transmission electron microscopy[2] to car windshield defoggers[3]. The vision for such simple yet potentially revolutionary applications is often beyond the purview of a first year graduate student, and was certainly beyond mine in when I started working on graphene in 2007, less than two years after the first experimental realization of high quality graphene electronic devices[4, 5] that effectively launched the field. Instead, I was attracted by graphene for its apparent theoretical simplicity, mostly, I suspect, because it was something I could understand. Electrons in typical two dimensional electronic systems (such as GaAs quantum wells) are massive, and are described by a scalar Hamiltonian. Electrons in monolayer graphene

are massless and described by a matrix Dirac Hamiltonian, in which the spin of relativistic electrons and speed of light are replaced by material analogs (the sublattice pseudsospin and Fermi velocity, respectively);

$$\hat{H}_{ML} = \hbar v_F \hat{\vec{\sigma}} \cdot \vec{k} \tag{1.1}$$

To a graduate student fresh out of quantum field theory courses taught by particle physicists, graphene felt familiar but appealingly tangible.

Graphene is a single plane of carbon atoms. For a theorist, the statement can stop there, resulting in Eq. 1.1. The work included in this thesis began as an attempt to probe the consequences of this Hamiltonian experimentally, however, and while Eq. 1.1 looks good on paper, in a physical graphene sheet there are many additional terms arising from *extrinsic* factors[6, 7]. The absence of a barrier separating the electrons in graphene from the environment is both a blessing and a curse. The direct experimental access to the electronic system has allowed chemical modifications, surface probes[8, 9], and the engineering of sharp electrostatic potentials. At the same time, nearby charges scatter electrons in graphene, and the graphene itself will physically conform to whatever it happens to be sitting on, obscuring the more subtle consequences of Eq. 1.1. From an experimental point of view, this thesis traces a few small steps in a battle against disorder in graphene. These approaches can be categorized loosely into 'flight' and 'fight,' reflecting whether experiments are designed so that disorder does not affect the desired physics, or whether disorder is purposely reduced to enable new experiments.

In Chapter 2, I will discuss the 'flight' approach. If the typical distance an electron can travel without scattering off the random disorder potential is ℓ_{mf}, one can hope to access fundamental, disorder free properties of graphene by using experimental probes on length scales smaller than

ℓ_{mf}. We did this by studying the tunneling of graphene electrons through very thin potential barriers. We found a direct demonstration of the role of the pseudospin degree of freedom inherent to the massless Dirac theory plays in scattering in graphene[10, 11]. The experiments illustrated the 'absence of backscattering' of the massless quasiparticles native to the honeycomb lattice[12] by measuring how they tunnel through a potential barrier: unlike massive quantum particles, which may tunnel through a wall some portion of the time, graphene quasiparticles will tunnel through the wall every time, provided they approach it head on. Similar experiments–indeed, the identical device and apparatus operated in a different parameter regime[11, 13]–probe the limits of the analogy with massless particles, and the physicality of the emergent Lorentz invariance of Eq. 1.1. In an effort to push the length scale far below that characterizing random scattering, these experiments culminated in the implementation of nanowire gated graphene transistors. In retrospect, the nanowire gates marked the inflection point between the 'flight' approach and the fight approach, paving the way for the shift away from frustrating attempts to apply technology developed for semiconductors to graphene device and towards a more graphene-tailored fabrication philosophy.

Chapter 3 of the thesis deals with the implementation of a technical improvement in the fabrication of graphene devices that moved us firmly towards the 'fight' approach to disorder in graphene, while simultaneously solving a number of nagging technological problems. In addition to the scattering from static impurities and ripples in the graphene, at high enough temperatures, the lattice vibrations of the substrate interact strongly with the graphene electrons–a serious problem for the room temperature operation of electronic devices (an effort in which I was also, peripherally, involved[14, 15]). Another persistent problem concerned the fabrication of reliable, thin dielectrics on graphene. Reliable dielectric layers for graphene are a technical necessity both for

high transconductance transistor applications and the creation of sharp potential barriers for mesoscopic physics exeriments. Dielectric deposition in semiconductors usually relies on some form of chemical process. This is problematic in graphene because the surface is not very reactive, and rendering it more reactive entails degrading the electronic properties. Of course this too is both a blessing in a curse, as the chemical inertness is largely responsible for the purity and robustness of graphene crystals, and the attendant high quality of the electronic system.

Graphite is a 'van der Waals material,' in that the the individual graphene layers are weakly bonded to their neighbors in the bulk crystal. It was thus natural—at least with the benefit of the hindsight with which PhD these are generally written!—to seek out a dielectric with similar chemical properties. Hexagonal boron nitride (hBN), an insulating analog of graphene, turned out to work better that we could have possibly anticipated. Not only is it exfoliatable, in the same manner as graphene, down to monolayer thickness, it is also extremely pure, owing at least in part to the extremely high temperature growth conditions under which it is synthesized[16]. Historically, our stumbling on hBN was a stroke of good luck. We were looking for a substrate to replace SiO_2 that would have much higher optical phonon energies, and a dielectric that would not degrade the mobility. hBN fit both requirements, at least in principle, and as it turned out some very high quality crystals happened to be floating around Columbia, having been used recently as a comparison material for nanomechanical measurements on graphene [17]. As it turned out, it was the (largely unanticipated) low charge trap content of the hBN that had the most dramatic effect. After about a year of development, transport and capacitance data [18, 19] showed that the graphene carrier mobility after replacement of SiO_2 with hBN improved by an order of magnitude and that thin hBN films have excellent dielectric properties. While everything good seems smart

in retrospect, it really cannot be overemphasized how lucky we were to have happened, on the first shot, upon such high quality material.

Chapter 4 describes transport studies of interaction effects at high magnetic fields in mono- and bilayer graphene that were enabled by the reduction in disorder that followed the innovations described in chapter 3. The original observations of the quantum Hall effect in monolayer [4, 5] graphene established that graphene was a two dimensional electronic system, and confirmed the appropriateness of the massless Dirac Hamiltonian in describing its charge carriers. Several theorists noticed rather quickly that the graphene could be different from that conventional quantum systems not only on the single particle level–where the QHE is essentially a reflection of the tight binding Hamiltonian—but also from the perspective of electronic interactions[20, 21]. The formation of Landau levels [22] in a two dimensional electronic system effectively quenches the kinetic energy, making a partially filled Landau level a strongly interacting physical system. The strong interactions can drive the system to form an ordered state, leading most famously to the fractional quantum Hall effect [23] but also to ferromagnetic or density wave states. In graphene, the unique Hamiltonian and lattice properties have been predicted to lead to an interesting set of ground states; but experimental probes have been limited by disorder [24]. The length scale associated with electronic interactions is the magnetic length, $\ell_B = \hbar/(eB)$, which is controlled by the size of the magnetic field–a parameter with a nonnegotiable technological upper limit for the purposes of experiments on graphene[25]. Decreasing the length scale of the disorder allowed us to access a new regime of electronic interactions in graphene. It feels as though we have just begun to scratch the surface of interacting quantum Hall effects in graphene, but already the broken symmetry states[26]—where the spin and valley degeneracies of the single particle graphene Hamiltonian

are spontaneously lifted—and fractional quantum Hall states[27] show graphene specific effects.

In the final chapter, I discuss experiments designed to probe in more detail the competing orders in graphene. Disentangling the phase diagram of interacting bilayer graphene, in particular, requires doing more than simple transport experiments. Transport experiments are inherently indirect, leading to difficulty in interpretation of data. It is therefore desirable to measure more directly ground state properties of a system, which can be simply related to basic physical quantities. In chapter 5, I develop the a theory [28] of capacitance measurements in bilayer graphene, and describe preliminary experiments[19] performed on disordered graphene devices using thin, hBN flakes as top gate dielectrics. We found that in bilayer graphene, capacitance measurements function as a probe of the pseudospin polarization. Interlayer capacitance is thus a useful addition to a graphene-specific measurement toolbox, whose potential, I think, is yet to be fully realized.

The descriptions of the experiments in the main chapters assume a basic knowledge of the theory of graphene. In the next sections, I will develop a few elementary aspects of that theory. Numerous review papers on graphene are available for further details[6, 7, 29–33].

1.2 Theoretical overview of graphene

1.2.1 Continuum Dirac model from the tight binding approximation

Monolayer graphene

Monolayer graphene consists of a single planar honeycomb net of carbon atoms. Each carbon atom has three nearest neighbors in the plane and four valence electrons. The Bravais lattice has unit lattice vectors

$$\vec{a}_1 = \left(\frac{\sqrt{3}a}{2}, \frac{a}{2}\right) \qquad \vec{a}_2 = \left(\frac{\sqrt{3}a}{2}, -\frac{a}{2}\right) \tag{1.2}$$

where $a = 2.46\mathring{A}$. Each unit cell consists of two identical carbon atoms, termed the A and B sublattices (orange and blue sites in Fig. 1.3 a). In-plane σ bonds form from the sp^2 hybridized in-plane valence electron orbitals, p_x, p_y and s. The σ bond is extremely strong, and contributes to the structural stability of graphene; however, the electrons are so tightly bound that they do not contribute to electronic transport. The remaining valence electron, consisting of the p_z orbital, forms the delocalized, covalent bond with the neighboring atoms that makes up the π band, which determines the low energy electronic structure.

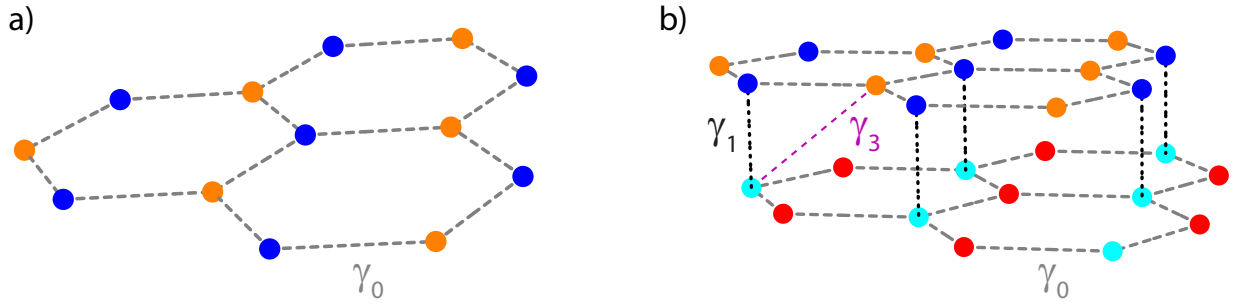

Figure 1.1: Mono- and bilayer graphene crystal lattice
Left: diagram of several unit cells of monolayer graphene. π electrons hop between neighboring atoms, with characteristic energy γ_0. Right: Bernal stacked bilayer graphene. In addition to the intraplane hopping, several interplane hopping terms determine the low energy band structure. For an appropriate energy range, the most important is γ_1, which connects the atoms in the two layers which lie directly on top of on another. Tight binding parameters have been extensively measured in graphite[34]

The π electrons are still sufficiently tightly bound that the electronic structure is well approximated by a tight-binding model[35]. Within the nearest-neighbor approximation, the tight-binding Hamiltonian is

$$\hat{H} = \gamma_0 \sum_{\langle i,j \rangle} \left(\hat{a}_i^\dagger \hat{b} + \textbf{H.C.} \right) \tag{1.3}$$

where $\hat{a}_i^\dagger$ ($\hat{a}_i$) and $\hat{b}_i^\dagger$ ($\hat{b}_i$) create (destroy) an electron on sublattice A or B, respectively, the hopping integral $\gamma_0 \simeq 3.16$ eV, and summation is over nearest neighbors on the honeycomb lattice. We write the Hamiltonian in the basis of the wavefunction amplitudes on the A and B sublattices, (ψ_A, ψ_B), taking into account the vectors connecting the nearest neighbors,

$$\vec{\delta_1} = \frac{a}{2}\left(\frac{1}{\sqrt{3}}, 1\right) \qquad \vec{\delta_2} = \frac{a}{2}\left(\frac{1}{\sqrt{3}}, -1\right) \qquad \vec{\delta_2} = \frac{a}{2}\left(\frac{2}{\sqrt{3}}, 0\right). \tag{1.4}$$

For arbitrary momentum $\vec{k}$ in the Brillouin zone,

$$\hat{H} = \gamma_0 \begin{pmatrix} 0 & \sum_j e^{i\vec{k}\cdot\vec{\delta_j}} \\ \sum_j e^{-i\vec{k}\cdot\vec{\delta_j}} & 0 \end{pmatrix} \tag{1.5}$$

with eigenvalues

$$\varepsilon_\pm(\vec{k}) = \pm\gamma_0 \sqrt{3 + 4\cos\left(\frac{\sqrt{3}ak_x}{2}\right)\cos\left(\frac{ak_y}{2}\right) + 2\cos\left(ak_y\right)}. \tag{1.6}$$

The spectrum 1.6 (portrayed in Fig1.2) is characterized by electron-hole symmetry of the bands and a degeneracy at the corners of the Brillouin zone, termed the K points:

$$\vec{K} = \left(0, \frac{4\pi}{3a}\right) \qquad \vec{K'} = \left(0, -\frac{4\pi}{3a}\right) \tag{1.7}$$

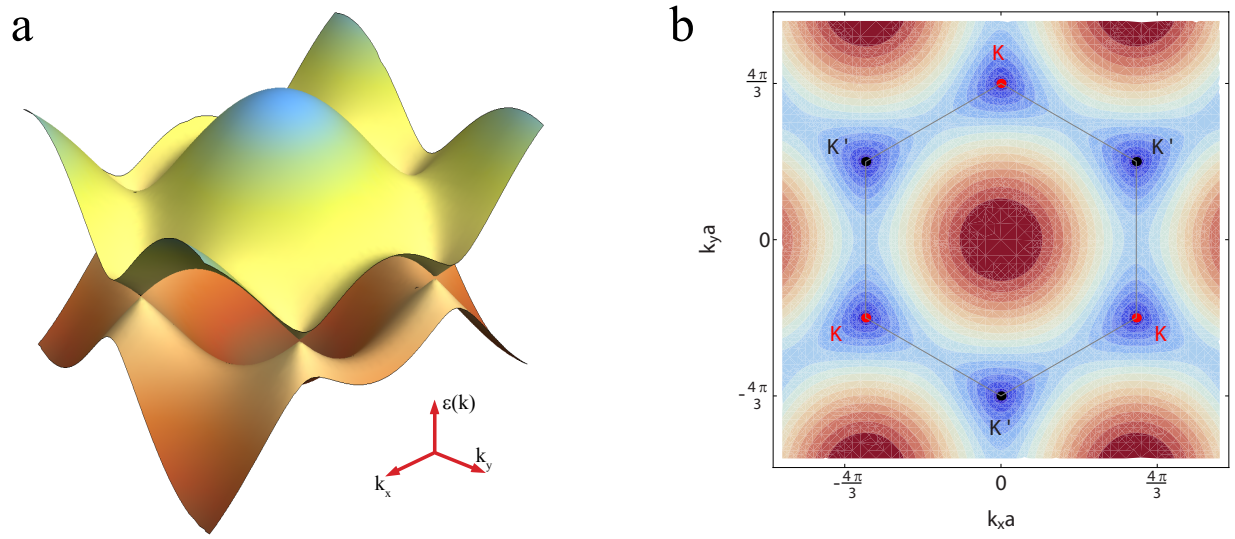

Figure 1.2: Tight binding band structure of monolayer graphene
Left panel: representation of the π-bands in monolayer graphene. The band structure has a large gap at the Γ point, but is gapless at the Brillouin zone corners. Right panel: contours of constant energy showing the degenerate $\vec{K}$ and $\vec{K}'$ points and the BZ boundary.

where $\varepsilon_{\pm}(\vec{K}) = \varepsilon_{\pm}(\vec{K}') = 0$. The electron-hole symmetry is in fact an artifact of the nearest neighbor approximation; however, the degeneracy is a fundamental property protected by the inversion symmetry of the honeycomb lattice, and survives to all orders. Each carbon atom contributes one electron to the π bands; as a result in undoped graphene the bands are exactly half filled, with the Fermi surface consisting of two 'Fermi points' at $\vec{K}$ and $\vec{K}'$. Expanding the Hamiltonian 1.5 about the K-points such that, e.g., $p \equiv \vec{K} - \vec{k}$, yields the low energy effective Hamiltonian,

$$\hat{H} = \frac{\sqrt{3}a\gamma_0}{2}\begin{pmatrix} 0 & i|\vec{p}|e^{-i\theta} & 0 & 0 \\ -i|\vec{p}|e^{i\theta} & 0 & 0 & 0 \\ 0 & 0 & 0 & i|\vec{p}|e^{i\theta} \\ 0 & 0 & -i|\vec{p}|e^{-i\theta} & 0 \end{pmatrix} = v_F \begin{pmatrix} \hat{\vec{\sigma}}\cdot\vec{p} & 0 \\ 0 & -\hat{\vec{\sigma}}\cdot\vec{p} \end{pmatrix} \tag{1.8}$$

where $v_F \equiv \frac{\sqrt{3}\gamma_0 a}{2}$, $\hat{\vec{\sigma}} = (\sigma_x, \sigma_y)$ is the vector of (appropriately chosen) Pauli matrices

$$\sigma_x = \begin{pmatrix} 0 & i \\ -i & 0 \end{pmatrix} \qquad \sigma_y = \begin{pmatrix} 0 & 1 \\ 1 & 0 \end{pmatrix} \qquad \sigma_z = \begin{pmatrix} 1 & 0 \\ 0 & -1 \end{pmatrix} \tag{1.9}$$

and the basis, $(\psi_{K,A}, \psi_{K,B}, \psi_{K',B}, \psi_{K',A})$, has been expanded to reflect the now decoupled 'Dirac valleys' at the BZ corners. Within each valley, the spectrum is linear:

$$\varepsilon(p) = \pm v_f|\vec{p}|. \tag{1.10}$$

The Hamiltonian 1.8 is formally identical to the theory of relativistic electrons first proposed by Dirac [36] in which the mass is exactly equal to zero and the physical speed of light has been replaced by the carrier Fermi velocity and, perhaps more importantly, the physical electron spin—which leads to the spinnor structure in theory of truly relativistic electrons—is replaced by a pseudospin, related to the graphene sublattices. Real spin sectors in physical graphene are decoupled in the absence of interactions, as are the valleys, leading to four identical copies, or flavors, of massless Dirac quasiparticles in graphene, one each for every combination of valley index and real spin projection.

The choice of the basis for 1.8 is for convenience, as it allows the Hamiltonian in each valley to be identical (modulo a sign, which inverts electron and hole states). However, this basis inverts the projection of pseudospin ($z \to -z$) and confuses the definition of chirality, to be considered in the next section. If we write Eq. 1.8 in the more transparent basis $(\psi_{K,A}, \psi_{K,B}, \psi_{K',A}, \psi_{K',B})$—such that the first component of a spinnor in both K and K' corresponds to the projection onto the same sublattice—we find that in fact the valleys have opposite handedness[37]:

$$\hat{H} = v_F \begin{pmatrix} \hat{\vec{\sigma}} \cdot \vec{p} & 0 \\ 0 & \hat{\vec{\sigma}}^* \cdot \vec{p} \end{pmatrix} \tag{1.11}$$

where as before $\hat{\vec{\sigma}}$ is the vector of *right handed* Pauli matrices and $\hat{\vec{\sigma}}^*$ is the corresponding vector of *left handed* Pauli matrices. The graphene literature is a bit confusing on this point. The electrons in the two valleys are both chiral, in the sense that the energy eigenstates are (trivially!) also eigenstates of the operator that projects spin onto momentum, $\frac{\hat{\vec{\sigma}} \cdot \vec{p}}{|\vec{p}|}$; in fact, the term chiral seems to be used whenever a definite relationship between pseudospin and momentum. However, the two valleys have opposite chirality—in that the chirality operator is right handed ($\hat{\vec{\sigma}} \cdot \vec{p}$) in the K valley and left handed ($\hat{\vec{\sigma}}^* \cdot \vec{p}$) in the K' valley.

Bilayer graphene

The tight binding analysis for bilayer graphene is more complicated than that for the monolayer, with significantly more parameters required to capture all features of the spectrum over a comparable range of energies. In particular, trigonal warping in bilayer arises from a nearest neighbor interlayer hopping, and plays a qualitatively important role in calculating the spectrum at both high and low energies[38]. In monolayer graphene, trigonal warping is a next to nearest neighbor effect

relevant only for very high energies. Here I will focus on the minimal model necessary to understand the experiments presented in this thesis. Although bilayer graphene crystals with arbitrary stacking order have recently become available, the experiments in this thesis are all performed on Bernal stacked bilayer graphene and I will only discuss this most common variety. In Bernal—or 'A-B' stacking—the monolayers are arranged so that the A sublattice of one lies directly on top of the B sublattice of the other (Fig. 1.3). The unit cell in bilayer graphene consists of four carbon atoms, two in each layer, denoted A1, B1, A2, and B2. The proximal atoms in the two layers interact strongly; this is captured in the tight-binding model by introducing an interlayer hopping parameter, $\gamma_1 \simeq 0.4$ eV. This term generates the largest difference between monolayer and bilayer graphene, with the other interlayer hopping term, $\gamma_3 \simeq$ eV generating trigonal warping only at very low energies. The Hamiltonian in the $(\psi_{A1}, \psi_{B1}, \psi_{A2}, \psi_{B2})$ follows from doubling Eq. 1.5 for the intralayer hopping in each layer and introducing γ_1 to couple $B1$ and $A2$,

$$\hat{H} = \begin{pmatrix} \frac{\Delta}{2} & \sum_j e^{i\vec{k}\cdot\vec{\delta}_j} & 0 & 0 \\ \sum_j e^{i\vec{k}\cdot\vec{\delta}_j} & \frac{\Delta}{2} & \gamma_1 & 0 \\ 0 & \gamma_1 & -\frac{\Delta}{2} & \sum_i e^{i\vec{k}\cdot\vec{\delta}_j} \\ 0 & 0 & \sum_j e^{i\vec{k}\cdot\vec{\delta}_j} & -\frac{\Delta}{2} \end{pmatrix}, \tag{1.12}$$

where the interlayer asymmetry parameter $\Delta = v_1 - v_2$ has been introduced in anticipation of the existence of substrate and electric fields. Expanding once again for low energies gives

$$\hat{H} = \xi \begin{pmatrix} \frac{\Delta}{2} & iv_f|\vec{p}|e^{-i\theta} & 0 & 0 \\ -iv_f|\vec{p}|e^{i\theta} & \frac{\Delta}{2} & \xi\gamma_1 & 0 \\ 0 & \xi\gamma_1 & -\frac{\Delta}{2} & iv_f|\vec{p}|e^{-i\theta} \\ 0 & 0 & -iv_f|\vec{p}|e^{i\theta} & -\frac{\Delta}{2} \end{pmatrix} \tag{1.13}$$

with $\xi = \pm 1$ for the expansion about $K(K')$ and the basis $(\psi_{A1}, \psi_{B1}, \psi_{A2}, \psi_{B2})$, for valley $\vec{K}$, or $(\psi_{B2}, \psi_{A2}, \psi_{B1}, \psi_{A1})$, for valley $\vec{K}'$. At high energies the bilayer band structure is linear, dispersing with the monolayer band velocity v_F and doubled bands offset by γ_1; however, at low energies the interlayer hopping and asymmetry parameters completely change the character of the electronic structure. For $\Delta = 0$, γ_1 splits the otherwise degenerate, monolayer-like bands into a high energy band associated with the B1-A2 dimer and a *parabolic* low energy band which is again degenerate the BZ corners. As in the monolayer, the degeneracy is protected by symmetry of the relevant sublattices, in this case $A1$ and $B2$; unlike monolayer, for bilayer these sublattices are spatially separated in the direction perpendicular to the plane. The symmetry can be broken by applying an electric field orthogonal to the graphene plane, introducing a finite interlayer asymmetry Δ. The resulting spectrum,

$$\varepsilon(p)^2 = (v_f p)^2 + \frac{\gamma_1^2}{2} + \frac{\Delta^2}{4} \pm \sqrt{(v_f p)^2 (\gamma_1^2 + \Delta^2) + \frac{\gamma_1^4}{4}}. \tag{1.14}$$

characterizes a semiconductor with a gate-tunable band gap.

While the higher subbands and Mexican hat structure of the gapped bilayer can, in principle,

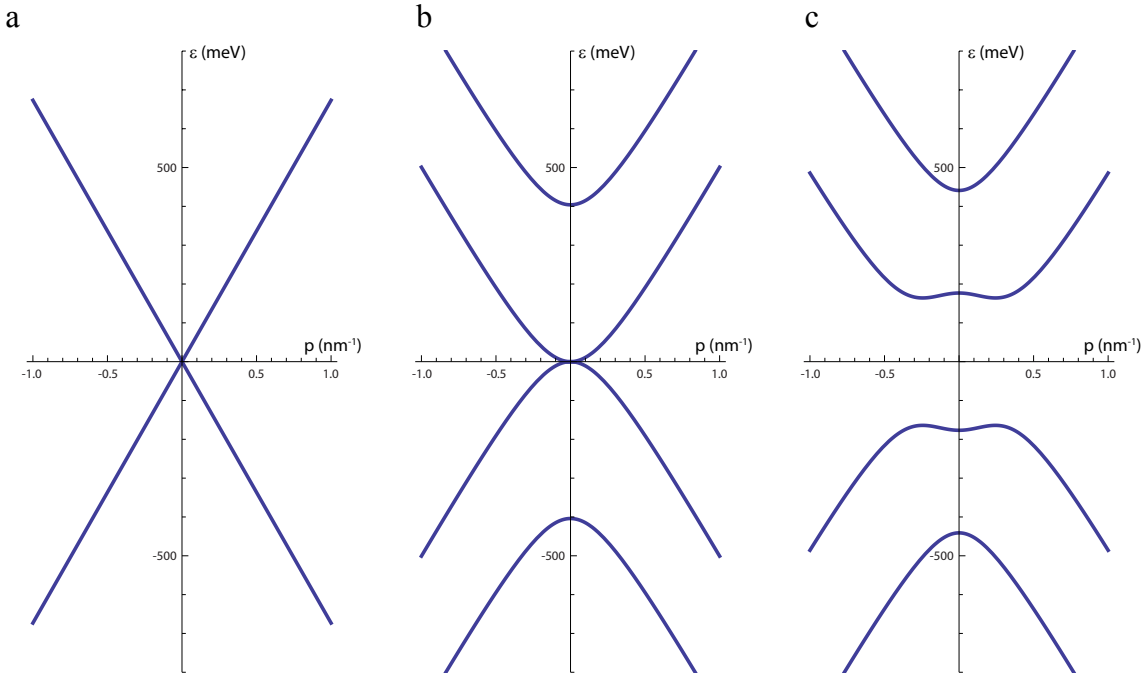

Figure 1.3: Low energy bands structure of mono- and bilayer graphene
a) Monolayer graphene band structure near a BZ corner. b) Bilayer graphene band structure near a BZ corner for $\Delta = 0$. c) Bilayer graphene band structure near a BZ corner for $\Delta \neq 0$.

be relevant for certain experiments, for the purposes of this thesis it is useful to make a further approximation, based on the fact that our experiments are carried out at energies $\varepsilon, \Delta \ll \gamma_1$. After integrating out the high energy bands (see [38] for details),

$$\hat{H} = \begin{pmatrix} \frac{\xi\Delta}{2}\left(1 + \frac{|\vec{p}|^2}{m\gamma_1}\right) & \frac{|\vec{p}|^2}{2m}e^{-2i\theta} \\ \frac{|\vec{p}|^2}{2m}e^{2i\theta} & -\frac{\xi\Delta}{2}\left(1 - \frac{|\vec{p}|^2}{m\gamma_1}\right) \end{pmatrix} \tag{1.15}$$

with eigenvalues

$$\varepsilon_{\pm} = \pm\sqrt{\left(\frac{p^2}{2m}\right)^2 + \left(\frac{\Delta}{2}\right)^2} \tag{1.16}$$

where the effective mass parameter $m = \frac{\gamma_1}{2v_f^2} \simeq \frac{m_e}{30}$, with m_e the bare electron mass. As for the four band Hamiltonian from which it is derived, this Hamiltonian is written in with opposite sublattice basis in the two valleys. The two band model captures the essential features of the bilayer intermediate energy band structure; however, it bears keeping in mind that it is far from quantitatively accurate, particulary for larger values of Δ despite being widely used both in this thesis and in the literature. The high energy dispersion is no longer linear, as it is in the full four-band model, and the Mexican hat structure at the band edge for $\Delta \neq 0$ has been replaced by a monotonic, quartic dispersion, which preserves the divergent density of states but misses the discontinuity occurring at the top of the head on whihc the 'Mexican hat' sits(see fig. 1.4).

1.2.2 Pseudospin and Chirality

The Hamiltonians of mono- and bilayer graphene are formally identical to those of Dirac electrons in relativistic quantum mechanics. As a result the quasiparticles in graphene are chiral, which means that there is a fixed relationship between pseudospin projection and carrier motion. This follows from the calculation of the eigenvectors of the Hamiltonians 1.8 and 1.15and the recollection that the basis in which the Dirac Hamiltonians are written is equivalent to the pseudospin projections. The eigenstates for monolayer graphene and bilayer graphene (for the case where $\Delta = 0$, more on $\Delta \neq 0$ later) are

$$\left|\psi^{\pm}_{ML,K}\right\rangle = = \frac{1}{\sqrt{2}} \begin{pmatrix} \pm e^{-i\theta} \\ 1 \end{pmatrix} \qquad \left|\psi^{\pm}_{BL,K}\right\rangle = \frac{1}{\sqrt{2}} \begin{pmatrix} \pm e^{-2i\theta} \\ 1 \end{pmatrix}. \tag{1.17}$$

The excitations of the K' valley are the same, but for the change of basis, related to inversion symmetry. Particles in opposite valleys have opposite chirality: in other words, pseudospin projections

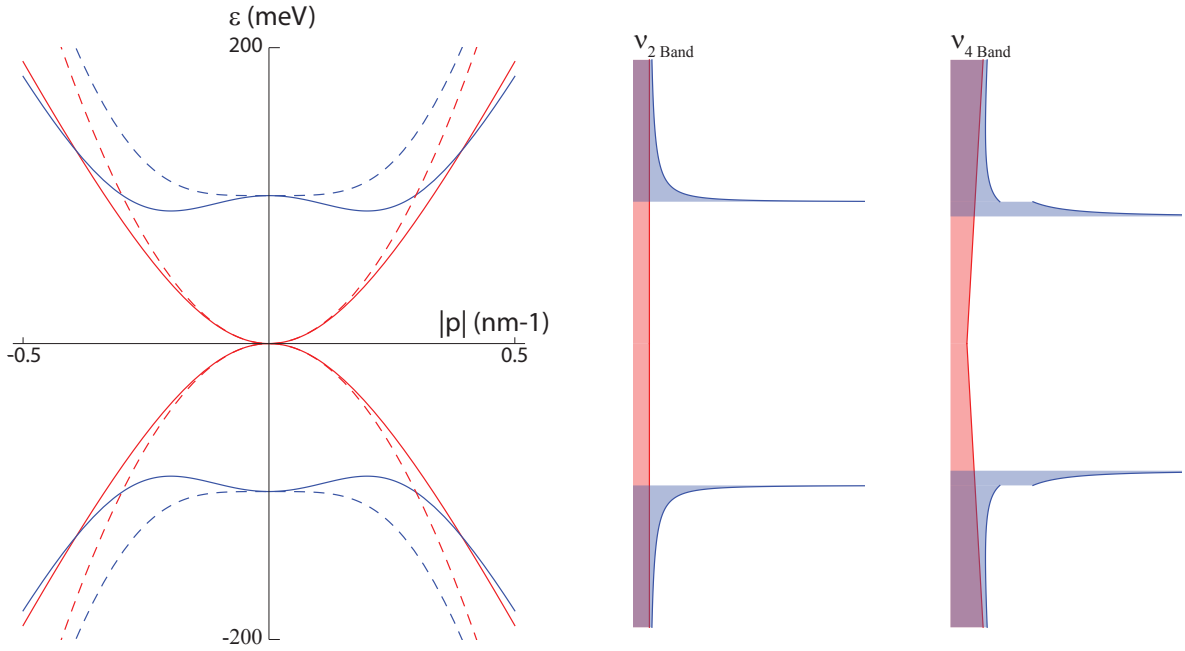

Figure 1.4: Comparison between 4 band and 2 band models for bilayer graphene
Comparison of the bilayer band structure as calculated in the four band and 2 band nearest neighbor tight binding models. In the two band model (dashed lines), the non-monotonic dependence of energy on p is replaced by a quartic dispersion. In addition, the high energy behavior is altered from linear to parabolic. Both of these changes alter the density of states, ν. In the four band model, ν is linear at high energy and, in addition to the $\sqrt{\varepsilon}$ singularity at the band edge, features a density of states discontinuity at $\varepsilon = \Delta/2$. Both of these features are lost in the two band model, which reproduces the band edge singularity but is quantitatively inaccurate elsewhere, especially for large Δ.

will be identical with the interchange of left-handed for right-handed Pauli matrices. While the details of intervalley chiral matrix elements are relevant for the general theory of impurity scattering in graphene, for the experiments in the next chapter, which are concerned with intravalley processes, we will ignore the subtleties of mixing chirality. To visualize the chirality of the charge carriers, we calculate the direction of the pseudospin as a function of the momentum, which enters the wavefunctions only through its direction, θ. This follows from taking the expectation value of the pseudospin operator $\hat{\vec{\sigma}}$, for a given eigenstate

$$\langle\hat{\vec{\sigma}}\rangle = \sum_{i=x,y,z} \langle\psi^{\pm}|\sigma_i|\psi^{\pm}\rangle = \begin{cases} \pm(\cos\theta, \sin\theta)^T & Monolayer \\ \pm(\cos 2\theta, \sin 2\theta)^T & Bilayer \end{cases} \tag{1.18}$$

Figure 1.5 shows the pseudospin projections along constant energy contours in the neighborhood of the K point for monolayer and bilayer graphene. In the monolayer, the pseudospin winds once in the process of circling the origin, independent of its energy (radius in p). In gapless bilayer, the pseudospin winding number is doubled: the pseudospin winds twice for a 2π rotation of the momentum, and is again energy independent.

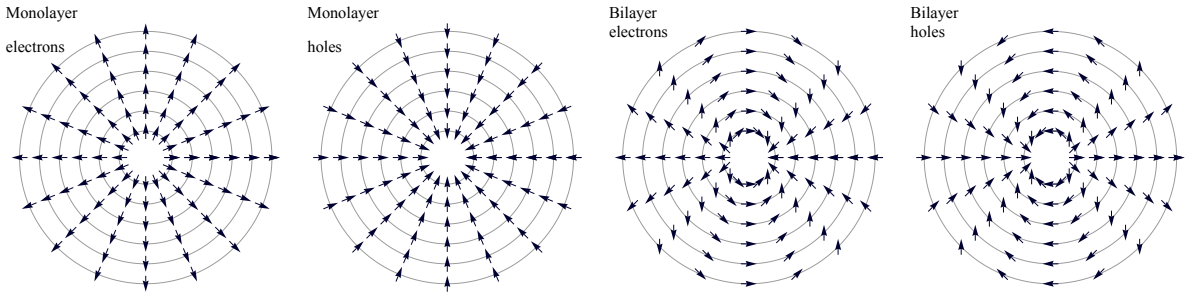

Figure 1.5: Pseudospin projections of chiral carriers in mono- and bilayer graphene
Pseudospin projections along constant energy contours for monolayer graphene and ungapped bilayer graphene. The pseudospin projection in both cases depends only on the propagation direction, and is energy independent. At the center of each circular plot is the K point and different radii correspond to momentum displacements from K. The plots can be extended to the K' point by taking electron to holes and understanding the definition of pseudospin Pauli matrices to be left-handed.

As will be discussed in the next section, the confinement of the pseudospin to the $x-y$ plane leads to dramatic effects in quasiparticle scattering. This confinement is tied to the inversion symmetry of the lattice, which is equivalent to transforming $A \leftrightarrow B$. In bilayer graphene this inversion symmetry is controlled by the parameter Δ, the interlayer potential imbalance, tunable by an external gate. This raises the question, what happens to the pseudospin for $\Delta \neq 0$? Fig. 1.6 shows the winding of the pseudospin in bilayer graphene for finite applied potential calculated in the two

band mdoel. Recalling that σ_z parameterizes the inter-sublattice imbalance in the wave functions, it is easy to see how finite Δ leads to the development of the finite $\langle\hat{\sigma}_z\rangle$. Near the band edge, the electrons are highly pseudospin polarized along the plane-perpendicular direction, and the notion of chirality is essentially meaningless—pseudospins is parallel, and out of plane, throughout the constant energy contour. At high energies, in contrast, the chirality is restored, as might be expected from the minimal change in band curvature that results at values of the energy $\varepsilon \gg \Delta$. Of course, fig. 1.6, calculated in the two band model, misses essential physics of the band edge. Nevertheless, the lesson is clear: for gapped bilayer graphene, care must be taken in understanding the role of pseudospin, which is no longer a simple property of the band structure.

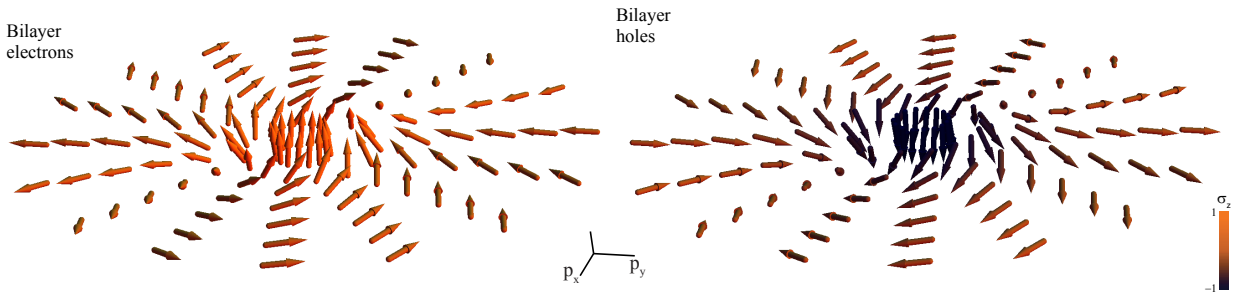

Figure 1.6: Pseudospin in gapped bilayer graphene
When $\Delta \neq 0$, pseudospin projection is no longer energy independent, as the layer imbalance induces an energy-dependent pseudospin rotation out of the sample plane. Finite overlap now exists between all pseudospin projections. Very near the band edge, carriers are almost completely pseudospin (equivalent to layer, in the two band model) polarized, leading to a loss of the chiral character of the wavefunctions; at high energies $\varepsilon \gg \Delta$ the chirality is asymptotically restored.

Chirality and scattering

Chirality plays an important role in the scattering of graphene quasiparticles. The 'absence of backscattering' inherent to the graphene single layer, calculated below, carries through to metallic

carbon nanotubes[12, 39], and it was speculated early on that this property was responsible for the high mobilities of carbon electronic materials. The next chapter of this thesis deals with a particular experiment designed to probe chiral scattering in graphene. In this section, I will show the results of some simple calculations designed to illustrate the basic physics.

Starting from the eigenvectors, Eq. 1.17, we consider the elastic scattering of mono- or bilayer graphene quasiparticles off a Coulomb scatterer, with potential $V(r)$. We assume that $V(r)$ does not have any nontrivial matric structure in the valley space, but otherwise has nonzero matrix elements for arbitrary intravalley scattering. The scattering probabilities in the first Born approximation,

$$|\langle\psi_{ML}(\vec{q})|V(r)|\psi_{ML}(\vec{q}')\rangle|^2 = \tilde{V}_{\vec{q}\vec{q}'}\delta_{|q|,|q'|}\cos^2\left(\theta_{qq'}/2\right) \tag{1.19}$$

$$|\langle\psi_{BL}(\vec{q})|V(r)|\psi_{BL}(\vec{q}')\rangle|^2 = \tilde{V}_{\vec{q}\vec{q}'}\delta_{|q|,|q'|}\cos^2\left(\theta_{qq'}\right), \tag{1.20}$$

are dominated, for isotropic momentum scattering, $V_{\vec{q}\vec{q}'} = V_0$, by the pseudospinnor matrix elements. The resulting angular dependence is plotted in Fig. 1.7. For both monolayer and bilayer graphene, chirality forbids certain transitions: in monolayer, backscattering is forbidden by the chirality, while in bilayer backscattering is allowed but right angle scattering, $\theta_{qq'} = \pm\pi_2$, is not. Naively, the contribution of chirality to the transport relaxation time–in which forward scattering plays little role but back scattering is very detrimental–will lead to different mobilities in monolayer and bilayer graphene even under identical conditions. This was thought to explain the generally higher mobility observed in monolayer flakes deposited on SiO_2. In fact, the different screening properties of bilayer and monolayer graphene are at least as important in determining

diffusive transport properties. As an aside, as of this writing bilayer graphene devices on hBN appear to show higher mobilities than monolayers[40], a fact that is not yet understood.

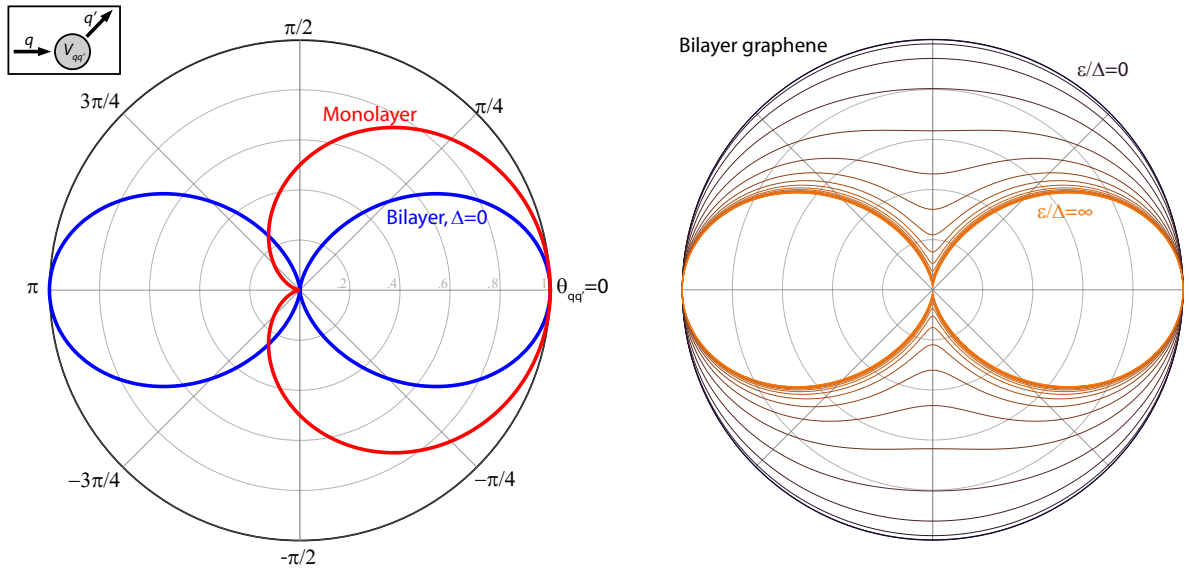

Figure 1.7: Chirality and scattering in graphenes: point scatterers
Chiral scattering matrix elements for a point defect that is smooth on the lattice scale. In monolayer graphene, momentum transfer across the Fermi results in a flipped pseudospin, resulting in an absence of backscattering. For bilayer graphene, opposite momenta have identical pseudospin, allowing backscattering but forbidding 90^o scattering. In gapped bilayer (right plot), carriers do not have a fixed chirality; however, the chirality of the ungapped band structure is preserved for sufficiently high energies. For energies near the band edge, the pseudospin points out of plane and has no effect on the scattering.

We now apply our insights about chirality to the p-n junction problem in monolayer and bilayer graphene, to be discussed at length in the next chapter. We consider transmission across a single pn junction which is, as before, infinitely sharp on the Dirac electron scale but sufficiently smooth on the lattice scale that it does not induce intervalley scattering. A long step maintains translation symmetry in the direction parallel to the barrier (say y), leading to a conservation of the

momentum in that direction k_y. Incident particles can either be transmitted (as holes) or reflected—corresponding to preserving or reversing the momentum perpendicular to the junction k_x. After providing a finite orbital matrix element for backreflection, the barrier disappears from the problem, and the transmission amplitude is completely dictated by the overlap between the spinnor part of the wavefunction of the incident electrons and holes:

$$|T|^2 = \langle \psi^+(\theta) | \psi^-(\pi - \theta) \rangle = \begin{cases} \cos^2 \theta & MLG \\ \sin^2(2\theta) & BLG \end{cases} \tag{1.21}$$

These simple equations imply that transmission through a pn junction depends strongly on the pseudospin winding number. Of particular interest is normal incidence. For monolayer graphene, the π winding number implies that back reflection entails reversing a pseudospin. This is a forbidden transition, as it is associated with a zero chiral matrix element. The oppositely propagating hole state, on the other hand, has identical pseudospin and, as a result, unit matrix element. At normal incidence, charge is transmitted with unit probability through the barrier by the reflectionless recombination of right moving electrons with left moving holes. In bilayer graphene the opposite is true. Because the pseudospin winds twice around the Fermi surface, electron backreflection is possible. Instead, it is the transmission that is forbidden: both hole states with $k_y = 0$ have the wrong pseudospin projection, leading to zero transmission.

The scattering properties of chiral carriers in mono- and bilayer graphene will be further elaborated in the next chapter, where the experimental equivalent of the gedanken experiment of Fig. 1.8 will be described. As we will see, in this simple experimental setup the perfect normal transmission of monolayer has a more dramatic effect than the perfect normal backreflection of bilayer, but both provide examples of the unique properties of the chiral Hamiltonians 1.8 and 1.15.

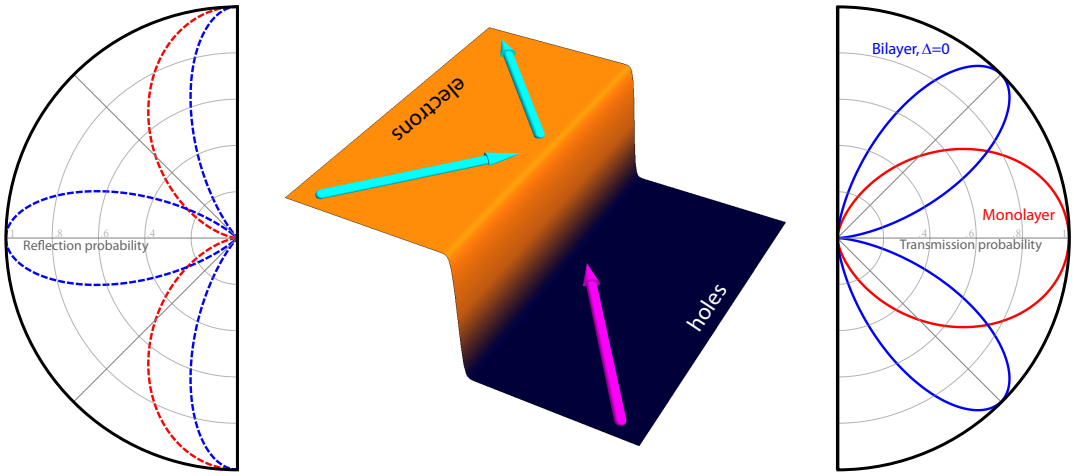

Figure 1.8: Chirality and scattering in graphenes: step potential
Transmission and reflection probabilities for a sharp potential step for mono- and bilayer graphene. The important features are at at normal incidence, where conservation of $k_y = 0$ enforces either forward or backward scattering. In monolayer, backscattering is forbidden as it would require flipping the pseudospin. Forward scattering is allowed, as the hole states with the $k_y = 0$ and opposite $-k_x$ have the identical pseudospin projection. In bilayer, the phenomenology is exactly opposite: backscattering is allowed, as electron state with opposite momenta have the same pseudospin; forward scattering is forbidden as both $k_y = 0$ hole states have the same, wrong projection of pseudospin.

1.3 Graphene in strong magnetic fields

A large part of this thesis deals with experiments performed in graphene at high magnetic fields. In this section we will derive a few basic results dealing with the formation of Landau levels (LLs) in mono- and bilayer graphene. The first section will deal with basic LL problem in graphene in the absence of interactions. The second section will briefly introduce the framework for understanding interaction effects.

1.3.1 Single particle Landau levels

We introduce the magnetic field, taken for now to be normal to the sample plane, to the Hamiltonians 1.8 and 1.15 through the minimal coupling to a (Landau gauge) vector potential $\vec{A} = -By\hat{x}$ and introduce the generalized momentum $\hat{\vec{\pi}}$

$$\hat{\vec{\pi}} = \vec{p} - \frac{e}{c}\vec{A} \tag{1.22}$$

The mono- and bilayer Hamiltonians simplify with the help of the definitions

$$\hat{a} \equiv \frac{\ell_B}{\sqrt{2}}\left(\hat{\pi}_x + i\hat{\pi}_y\right) \qquad \hat{a}^\dagger \equiv \frac{\ell_B}{\sqrt{2}}\left(\hat{\pi}_x - i\hat{\pi}_y\right) \tag{1.23}$$

$$\hat{R}_x \equiv x - \ell_B^2\pi_y \qquad \hat{R}_y \equiv y + \ell_B^2\pi_x \tag{1.24}$$

$$[\hat{a}, \hat{a}^\dagger] = 1 \qquad \left[\hat{R}_x, \hat{R}_y\right] = i\ell_B^2 \tag{1.25}$$

The commutation relation for $\hat{a}$ and $\hat{a}^\dagger$ ensure that they are creation and annihilation operators for a one dimensional harmonic oscillator; given the normalization,

$$\hat{a}|n\rangle = \sqrt{n}|n-1\rangle \qquad \hat{a}^\dagger|n\rangle = \ell_B\sqrt{n+1}|n+1\rangle \tag{1.26}$$

Because we will ultimately be interested in the sublattice structure of the wavefunctions, we use the same sublattice basis, (ψ_A, ψ_B), in the two valleys for both monolayer and bilayer graphene. The Hamiltonians, with the definitions Eq. 1.25, become very simple:

$$\hat{H}^{ML}_{\vec{K}} = \frac{\sqrt{2}v_F}{\ell_B}\begin{pmatrix} 0 & \hat{a}^\dagger \\ \hat{a} & 0 \end{pmatrix} \qquad \hat{H}^{ML}_{\vec{K}'} = -\frac{\sqrt{2}v_F}{\ell_B}\begin{pmatrix} 0 & \hat{a} \\ \hat{a}^\dagger & 0 \end{pmatrix} \tag{1.27}$$

$$\hat{H}^{BL}_{\vec{K}} = \omega_c \begin{pmatrix} \frac{\tilde{\Delta}}{2}\left(1+\frac{2\hat{a}^\dagger\hat{a}}{\tilde{\gamma}_1}\right) & \left(\hat{a}^\dagger\right)^2 \\ \hat{a}^2 & -\frac{\tilde{\Delta}}{2}\left(1-\frac{2\hat{a}\hat{a}^\dagger}{\tilde{\gamma}_1}\right) \end{pmatrix} \tag{1.28}$$

$$\hat{H}^{BL}_{\vec{K}'} = -\omega_c \begin{pmatrix} -\frac{\tilde{\Delta}}{2}\left(1+\frac{2\hat{a}\hat{a}^\dagger}{\tilde{\gamma}_1}\right) & \hat{a}^2 \\ \left(\hat{a}^\dagger\right)^2 & \frac{\tilde{\Delta}}{2}\left(1-\frac{2\hat{a}^\dagger\hat{a}}{\tilde{\gamma}_1}\right) \end{pmatrix} \tag{1.29}$$

Here $\omega_c = eB/m$ is the bilayer graphene cyclotron frequency and $\tilde{\Delta} \equiv \Delta/\omega_c$ and $\tilde{\gamma_1} = \gamma_1/\omega_c$; the two band model is strictly valid only in the limit $\gamma_1 \gg \omega_c \gg \Delta$, which again is not actually satisfied in the experiments in this thesis . As in the scalar case, the cyclotron guiding center is an integral of the motion, $[\hat{H}, \hat{R}_x] = [\hat{H}, \hat{R}_y] = 0$, leading to the massive degeneracy of the Landau levels. Solving for the eigenvectors and eigenvalues for the monolayer, we find

$$\varepsilon^{ML}_{\vec{K}}(n,\pm) = \mp\frac{v_F\sqrt{2n}}{\ell_B} \qquad \varepsilon^{ML}_{\vec{K}'}(n,\pm) = \pm\frac{v_F\sqrt{2n}}{\ell_B} \tag{1.30}$$

$$|n,\pm\rangle^{ML}_{\vec{K}} = \begin{cases} \begin{pmatrix} |n\rangle \\ \pm|n-1\rangle \end{pmatrix} & n \geq 1 \\ \begin{pmatrix} |0\rangle \\ 0 \end{pmatrix} & n = 0 \end{cases} \qquad |n,\pm\rangle^{ML}_{\vec{K}'} = \begin{cases} \begin{pmatrix} \pm|n-1\rangle \\ |n\rangle \end{pmatrix} & n \geq 1 \\ \begin{pmatrix} 0 \\ |0\rangle \end{pmatrix} & n = 0 \end{cases} \tag{1.31}$$

While for bilayer graphene with $\Delta = 0$,

$$\varepsilon^{BL}_{\vec{K}}(n,\pm) = \pm\frac{\sqrt{n(n-1)}}{m\ell_B^2} \qquad \varepsilon^{BL}_{\vec{K}}(n,\pm) = \mp\frac{\sqrt{n(n-1)}}{m\ell_B^2} \tag{1.32}$$

$$|n,\pm\rangle^{BL}_{\vec{K}} = \begin{cases} \begin{pmatrix} |n\rangle \\ \pm|n-2\rangle \end{pmatrix} & n \geq 2 \\ \begin{pmatrix} |0\rangle \\ 0 \end{pmatrix} & n = 0 \\ \begin{pmatrix} |1\rangle \\ 0 \end{pmatrix} & n = 1 \end{cases} \qquad |n,\pm\rangle^{BL}_{\vec{K}'} = \begin{cases} \begin{pmatrix} \pm|n-2\rangle \\ |n\rangle \end{pmatrix} & n \geq 2 \\ \begin{pmatrix} 0 \\ |0\rangle \end{pmatrix} & n = 0 \\ \begin{pmatrix} 0 \\ |1\rangle \end{pmatrix} & n = 1 \end{cases} \tag{1.33}$$

The Landau level solutions for the two systems have many similarities (see figure 1.9). First, the energy spectra contain both negative and positive energy states, and are electron hole symmetric (again, this last is an artifact of the approximate Hamiltonians used). They are depicted in Figure. 1.9. Second, energy spectra for the two valleys are identical, making each LL twice again as degenerate. Combined with the spin degeneracy, there are four flavors of electron ($|K,\uparrow\rangle$,$|K,\downarrow\rangle$,$|K',\uparrow\rangle$, and $|K',\downarrow\rangle$, where $\uparrow$ and $\downarrow$ correspond to opposite real spin projections) allowing a quadruple occupancy of each cyclotron guiding center and a quadrupled LL degeneracy. Unlike the physical spin, however, the valley degenerate wavefunctions have different microscopic orbital structure, encoded in the different probability amplitudes on the two sublattices in the different valleys for a given n. Finally, both mono- and bilayer graphene feature a zero LL (ZLL) that does not disperse with magnetic field. The combination of the zero modes with the LL degeneracies leads to the anomalous quantum Hall sequences,

$$\sigma_{xy}^{ML} = \pm 4\left(n + \frac{1}{2}\right) \qquad \sigma_{xy}^{BL} \pm 4n \tag{1.34}$$

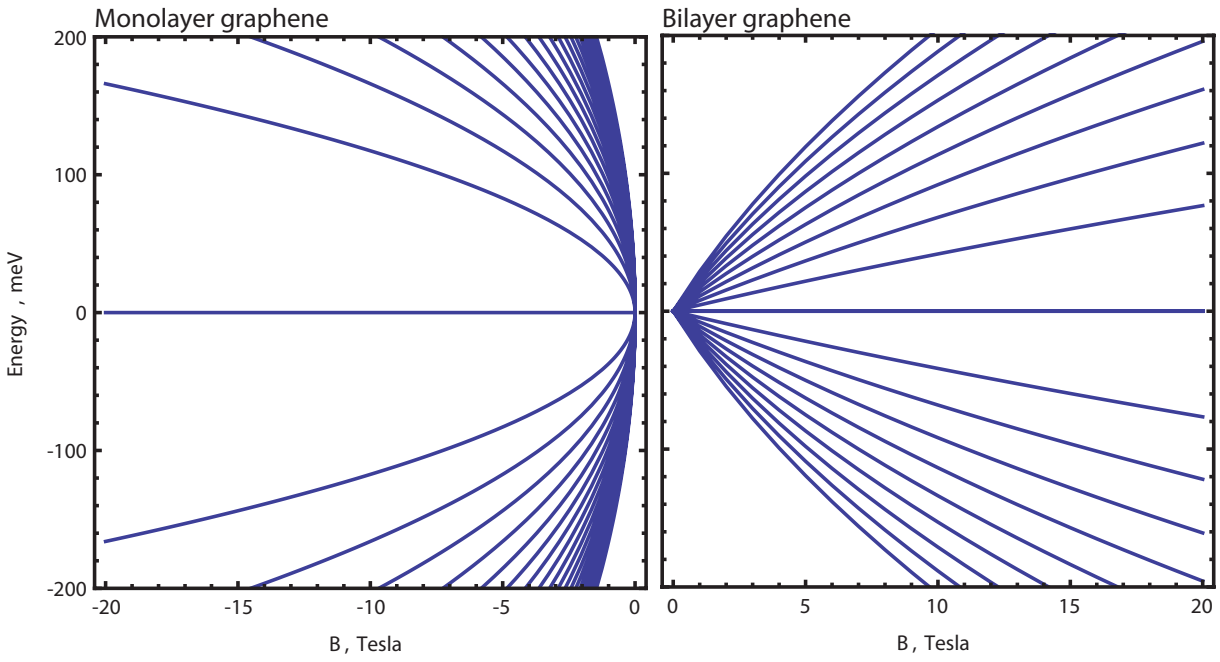

Figure 1.9: Cyclotron energies in mono- and bilayer graphene
Landau Level spectrum over the experimentally relevant range of energy and perpendicular magnetic field, ignoring the effects of Zeeman and electric field splittings ($g = 0$ and $\Delta = 0$.) The monolayer graphene two band model, Eq. 1.8, is highly accurate over the entire density range, while for bilayer the sublinearity of the cyclotron energies is a consequence of the $\mathfrak{O}(\omega_c/\gamma_1)$ corrections to the two band model. Not included in the calculations are e-h asymmetric next-to-nearest neighbor terms, or trigonal warping.

Within the ZLL, the valley wavefunctions take on a dramatically different orbital character. Whereas for the non-zero LLs, the electron is spread equally over the two sublattices (although the distribution can vary locally, $\langle x|n\rangle \neq \langle x|n-1\rangle$), in the ZLL the valley wavefunctions are completely localized on a single sublattice. It is worth trying to visualize this: the LL wavefunctions

$\langle x|n\rangle$ have characteristic scale $\ell_B \gg a$; however, in the ZLL populating a single guiding center in the K valley means creating a particle that is spread over many unit cells but has zero probability of being found on the B sublattice! As discussed in the next section, the anomalous orbital structure of the ZLL changes the nature of the many-body ground states, with observable consequences. The ZLL is particularly anomalous in bilayer graphene, where the additional $|0\rangle, |1\rangle$ degeneracy is strongly orbital nature: unlike the valley isospin, which is spin-like at long wavelengths (in the sense that its orbital structure occurs only for length scales $a \ll \ell_B$), the bilayer ZLL orbital degeneracy has structure at the leading length scale in the problem. This is a unique property of bilayer graphene, with no analog in other electronics systems.

The same magnetic field that creates the LLs cannot be prevented from exerting a Zeeman effect on the real spins, leading to a splitting of the otherwise degenerate LLs into two spin branches separated by $E_Z = g\mu_B B_T$, where $g = 2$ is the electron gyromagnetic ratio in graphene and B_T is the total magnetic field, which need not be oriented in any particular way relative to the graphene plane. In monolayer graphene, no such single-particle aligning field exists for the valley degree of freedom, as this would be require a term in the monolayer Hamiltonian proportional to σ_z in the $A - B$ space, equivalent to a potential modulation commensurate with the lattice. In bilayer graphene, as for zero magnetic field, the interlayer asymmetry can play this role, layer (read as 'sublattice' for the two band model)-unbalancing the eigenfunctions. The lowest order electric field induced splitting in the higher LLs is generated by the $\hat{a}^\dagger\hat{a}$ type diagonal terms, and consequently is rather small (by an additional factor of ω_c/γ_1, which must be small for the two band model to be justifiable). The octet ZLL has a large sublattice splitting, of order Δ, and a second order splitting of the $n = 0$ and $n = 1$ states which is smaller by a factor of ω_c/γ_1.

$$\varepsilon_{n\geq 2} = \pm\omega_c\sqrt{n(n-1)} - \xi\Delta\frac{\omega_c}{\gamma_1} \tag{1.35}$$

$$\varepsilon_0 = \frac{\xi\Delta}{2} \tag{1.36}$$

$$\varepsilon_1 = \frac{\xi\Delta}{2} - \xi\Delta\frac{\omega_c}{\gamma_1} \tag{1.37}$$

For the $n \geq 2$ LLs, the competition between electric field and magnetic field induced splittings seems sufficient, for now, in understanding the experimental data (presented later on in the thesis). In the octet, in contrast, electronic interactions are thought to completely alter the energy spectrum[41], making the single particle considerations discussed here largely irrelevant.

It is worth commenting on the validity of certain approximations used for both monolayer and bilayer graphene. For the monolayer, the linear tight binding model Hamiltonian 1.8 is and extremely good approximation, as is the LL Hamiltonian derived from it. The spectrum in monolayer graphene does not deviate appreciably from linear over an energy range of order one electron volt. In bilayer graphene, in contrast, the two band approximation is almost never valid. At low energies, such as those accessed in experiments on very clean suspended graphene, the trigonal warping term γ_3 becomes important, while at not-too-high energies the higher subbands enter at order ω_c/γ_1. This factor can be of order unity for rather small values of experimental parameters: $\omega_c/\gamma_1 \sim 1$ at $B_\perp \sim 5\mathrm{T}$. Experimentally, we are interested in the regime where disorder does not dominate the physics, $\omega_c > \Gamma$ (where Γ is the LL level broadening that characterizes the strength of the disorder), restricting us to fields above a few Tesla. As the two band model breaks down, bilayer loses some its similarity to monolayer. In the full unit cell basis, Eq. 1.38, the LL

Hamiltonian now contains coupling to the neglected sublattices:

$$\hat{H} = \xi \begin{pmatrix} \frac{\Delta}{2} & \frac{\sqrt{2}v_F}{\ell_B}\hat{a}^\dagger & 0 & 0 \\ \frac{\sqrt{2}v_F}{\ell_B}\hat{a} & \frac{\Delta}{2} & \xi\gamma_1 & 0 \\ 0 & \xi\gamma_1 & -\frac{\Delta}{2} & \frac{\sqrt{2}v_F}{\ell_B}\hat{a}^\dagger \\ 0 & 0 & \frac{\sqrt{2}v_F}{\ell_B}\hat{a}^\dagger & -\frac{\Delta}{2} \end{pmatrix} \tag{1.38}$$

with LL wave functions of the form $|\psi\rangle_n > (\alpha\,|n\rangle\,, \beta\,|n-1\rangle\,, \gamma\,|n-1\rangle\,, \delta\,|n-2\rangle)^T$, $|\alpha|^2 + |\beta|^2 + |\gamma|^2 + |\delta|^2 = 1$, for $n \geq 2$. The LL wavefunctions in the higher LLs lose some of their unique character whenγ_1 is not large compared to other energy scales: $|n-1\rangle$ now exists on both layers, making the layers more symmetric looking, and their tunability with gate potentials, particularly as pertains the the LL structure factors[42], decreases. Importantly, the octet modes survive unaltered (for $\Delta = 0$), as they are zero modes protected by the inversion symmetry of the lattice and are not affected by the degree of the tight binding approximation taken.

Chapter 2

Phase coherent transport in graphene heterojunctions

2.1 Bipolar junctions: Klein tunneling

2.1.1 Review of Klein tunneling in relativistic quantum mechanics

One-dimensional scattering is one of the canonical problems of introductory quantum mechanics. For massive, non-relativistic particles, the scattering from a finite potential step helps to elucidate fundamental concepts of quantum mechanics, such as uncertainty and tunneling. Little wonder, then, that within little more than a year of Dirac's discovery of the equation for relativistic electrons [36], now known as the Dirac equation, Oskar Klein calculated the barrier transmission problem for relativistic electrons [43]. Klein's result was considered paradoxical at the time. In non-relativistic quantum mechanics, the transmission probability of a particle with energy ε incident on a potential barrier of height $V > \varepsilon$ along the x direction is exponentially decaying with distance, $|T|^2 \sim \exp(-\kappa x)$ where $\kappa > 0$ is a kinetic factor depending on incident particle's energy and

barrier height as usual; in contrast, Klein found that for the relativistic case, the transmission probability does not decay with distance even for $V \gg \varepsilon$, $|T|^2 \sim \left(4\alpha/(1+\alpha)^2\right)^2$ (like κ, here $\alpha \geq 1$ is a kinematic factor obtained from Dirac equation).

The so-called Klein paradox is in two parts. First, far past the barrier, the scattering states are antiparticles, or, in the context of condensed matter, holes—a theoretical consequence of the Dirac equation not experimentally confirmed at the time of Klein's calculation [44]. Incident particles do not tunnel in the sense of propagating a short distance as evanescent waves; rather, they propagate as antiparticles whose inverted energy-momentum dispersion relation allows them to move freely under the barrier. The second and more subtle paradox is that, even given the existence of holes, tunneling into the barrier should be accompanied by exponential decay of the transmission probability due to the strong repulsive potential at the step. This problem was clarified in 1931 by Sauter[45], who calculated the transmission of particles over a step with a finite width, finding the expected exponential decay:

$$U(x) = \begin{cases} 0 & x < 0 \\ Fx & 0 \leq x \leq L \\ V & x > L \end{cases} \qquad |T|^2 \sim e^{-2\pi^2 \frac{hc}{F\lambda_C^2}} \tag{2.1}$$

where $\lambda_C = h/(mc)$ is the Compton wavelength and the electric field $F = V/L$. The Klein result of $|T|^2 \sim 1$ obtains for barriers that are sharp compared to the Compton wavelength. The origin of the exponential damping is the existence of regions in the center of the barrier where $\varepsilon - m < V < \varepsilon + m$ and which, as a result, cannot support either electron or hole propagating states (Fig. 1.8). To leading exponential order, the transmission is then given by $T \sim \exp i \int p(x) dx$,

where the momentum of the particle in the barrier $p(x) = \pm\sqrt{(U(x) - \varepsilon)^2 - m^2}$ and the integral runs across this classically forbidden region.

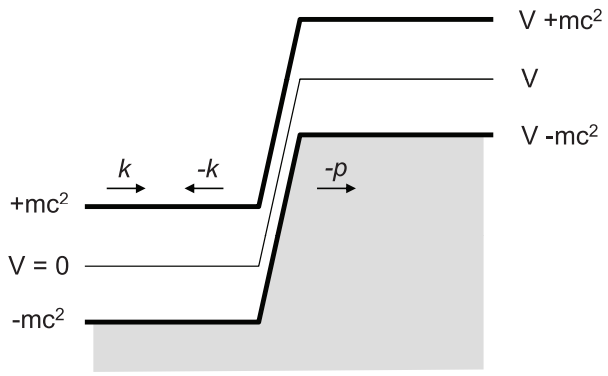

Figure 2.1: Klein tunneling for massive particles
An electron of energy ε scattering off a Klein-Sauter step of height $V > 2m$. The electrons are shown with solid arrowheads; the hole state has a hollow arrowhead. The particle continuum (slanted background) and the hole continuum (shaded background) overlap when $m < \varepsilon < V - m$.

While the problem of particles tunneling through and even being generated by sharp potential barriers would continue to be applied to physical systems as varied as supercritical atoms and black holes [46], the Klein problem, in its simplest formulation, remained a thought experiment and textbook problem for more than 70 years. The main obstacle in the experimental realization is the creation of potentials varying on the scale of the Compton wavelength, a rather tall order for 'bare' electrons, whose Compton wavelength is $\sim 10^{-12}$ m. In the context of particle physics, such a barrier—effectively achieved in high energy collisions—quickly leads to physics dominated by the creation of new particles. As discussed in the next section, however, graphene offers a condensed matter realization of the original gedanken experiment in both the Klein and Sauter limits through

the study of relativistic single particle tunneling through controllable potential barriers. [1]

2.1.2 The Klein tunneling problem in graphene

The approach outlined in the previous section requires only small modifications to apply to the case of carrier transport across graphene heterojunctions. While the direct calculation for the case of graphene was done by Katsnelson et al. [47], a similar approach taking into account the chiral nature of carriers was already discussed a decade ago in the context of electrical conduction in metallic carbon nanotubes [12]. In monolayer graphene, the free particle states described by Eq. 1.1 are chiral, meaning that their pseudospin is parallel (antiparallel) to their momentum for electrons (holes). This causes a suppression of backscattering in the absence of pseudospin-flip nonconserving processes, leading to the higher conductances of metallic over semiconducting carbon nanotubes [39]. To understand the interplay between this effect and Klein tunneling in graphene, we introduce external potentials $\vec{A}(\vec{r})$ and $U(\vec{r})$ in the Dirac Hamiltonian,

$$\hat{H} = v_F \vec{\tau} \cdot \left(\vec{\nabla} - e\vec{A}(\vec{r}) \right) + U(\vec{r}). \tag{2.2}$$

In the case of a 1-dimensional (1D) barrier, $U(\vec{r}) = U(x)$, at zero magnetic field, the momentum component parallel to the barrier, p_y, is conserved. As a result, electrons normally incident to a graphene p-n junction are forbidden from scattering obliquely by the symmetry of the potential, while chirality forbids them from scattering directly backwards: the result is perfect transmission as holes [47], and this is what is meant by Klein tunneling in graphene (see (Fig. 2.2) (a)). The rest of this section is concerned with gate induced p-n junctions in graphene; however, the necessarily

[1] A comprehensive and pedagogical review of the early history of the Klein tunneling problem—from which much of the material in this section is distilled—can be found in [46].

transmissive nature of graphene p-n junctions is crucial in understanding the minimal conductivity [48] and supercritical Coulomb impurity [49] problems in graphene, and necessarily plays a role in efforts to confine graphene quantum particles [50]. Moreover, p-n junctions appear in the normal process of contacting [51–55] and locally gating [14, 56] graphene, both of which are indispensable for electronics applications.

Even in graphene, an atomically sharp potential cannot be created in a realistic sample. Usually, the distance to the local gate, which is isolated from the graphene by a thin dielectric layer determines the length scale on which the potential varies. The resulting transmission problem over a a Sauter-like potential step in graphene was solved by Cheianov and Fal'ko [57]. Substituting the Fermi energy for the potential energy difference $\varepsilon - U(x) = \hbar v_f k_f(x)$ and taking into account the conservation of the momentum component $p_y = \hbar k_F \sin\theta$ parallel to the barrier, they obtained a result, valid for $\theta \ll \pi/2$, that is nearly identical to that of Sauter (Fig. 2.2(b))

$$k_F(x) = \begin{cases} -k_F/2 & x < 0 \\ Fx & 0 \le x \le L \\ k_F/2 & x > L \end{cases} \qquad |T|^2 \sim e^{-2\pi^2 \frac{\hbar v_F}{F\lambda_F^2} \sin^2\theta}. \tag{2.3}$$

As in the massive relativistic problem in one-dimension, the transmission is determined by evanescent transport in classically forbidden regions where $k_x(x)^2 = k_F(x)^2 - p_y^2 < 0$ (Fig.2.2). The only differences between the graphene case and the one dimensional, massive relativistic case are the replacement of the speed of light by the graphene Fermi velocity, the replacement of the Compton wavelength by the Fermi wavelength, and the scaling of the mass appearing in the transmission by the sine of the incident angle. By considering different angles of transmission in the barrier problem in two dimensional graphene, then, one can access both the Klein and Sauter

regimes of $T \sim 1$ and $T \ll 1$.

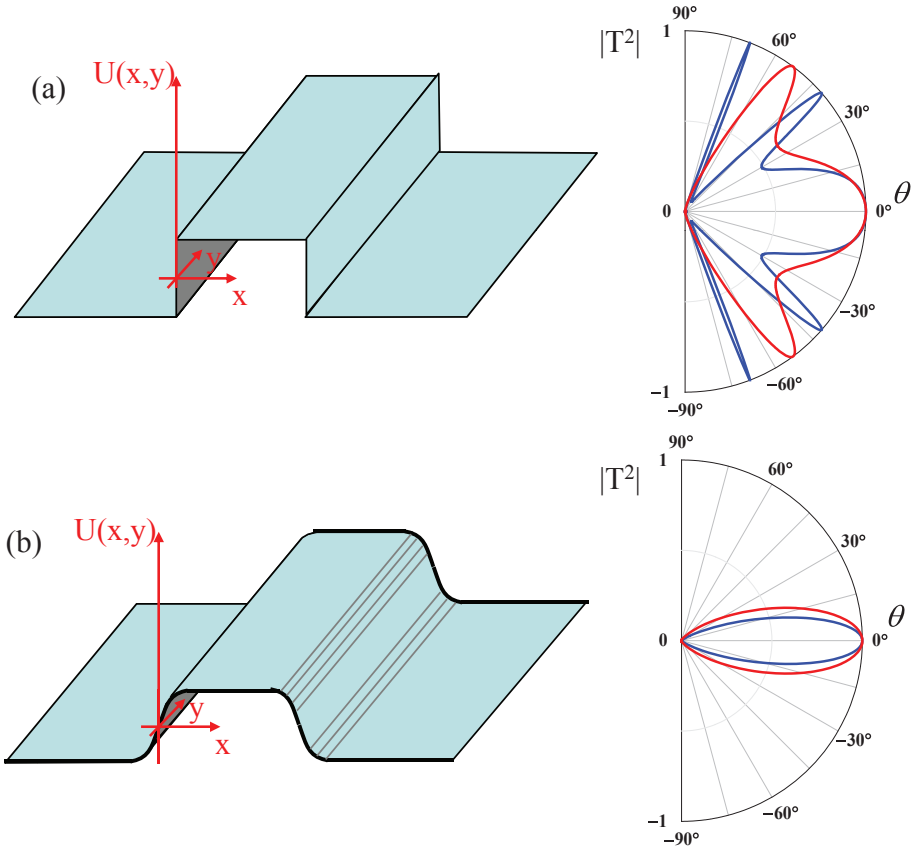

Figure 2.2: Transmission through bipolar heterojunctions: the effect of smooth potentials Potential landscape and angular dependence of quasiparticle transmission through (a) an atomically sharp pnp barrier and (b) an electrostatically generated smooth pnp barrier in graphene, with their respective angle-dependent transmission probability. Red and blue lines correspond to different densities in the locally gated region.

The current state of the experimental art in graphene does not allow for injection of electrons with definite p_y [10, 58–63]. Instead, electrons impinging on a p-n junction have a random distribution of incident angles due to scattering in the diffusive graphene leads. Eq. 2.3 implies that in

realistically sharp p-n junctions, these randomly incident electrons emerge from the p-n junction as a collimated beam, with most off-normally incident carriers scattering; transmission through multiple p-n junctions leads to further collimation [64]. Importantly, even in clean graphene, taking into account the finite slope of the barrier yields qualitatively different results for the transmission: just as in the original Klein problem, the sharp potential step [47, 65–70] introduces pathologies—in the case of graphene, high transmission at $\theta \neq 0$—which disappear in the more realistic treatment [57, 64, 71].

In fact, the expressions in Eq. 2.1 and 2.3 are exact for small angles—although the semiclassical approximation used to obtain them is valid only to leading exponential order, the prefactor of T is constrained to a pure phase by the absence of backscattering [12, 39] mentioned above. This allows a quantitative calculation of the ballistic conductance of a graphene p-n junction via the Landauer formula [57]

$$G = \frac{4e^2}{h} \int \frac{W k_F d\theta}{2\pi} |T(\theta)|^2 \approx \frac{2e^2}{\pi h} W \sqrt{\frac{F}{\hbar v_F}}. \tag{2.4}$$

For non-phase coherent transport, Eq. 2.4 represents the principal consequence of graphene Klein tunneling p-n junctions.

2.1.3 Non-phase coherent transport

Graphene's gapless spectrum allows the fabrication of adjacent regions of positive and negative doping through the use of local electrostatic gates. Such heterojunctions offer a simple arena in which to probe the peculiar properties of graphene's massless Dirac charge carriers, including chirality [47, 57] and emergent lorentz invariance [13, 32, 72]. Technologically, graphene p-n

junction are relevant for various electronic devices, including applications in conventional analog and digital circuits [14, 73] as well as novel electronic devices based on electronic lensing [74–77]. In the latter part of this section, we will discuss current experimental progress towards such gate-engineered coherent quantum graphene devices.

Producing clean locally gated samples is the principal experimental challenge which must be overcome in order to observe Klein tunelling physics in graphene. In particular, if the electrons scatter within the p-n junction, Eq. 2.4 does not hold, as it relies on translational symmetry in the y-direction and ballistic electron motion. The condition for the validity of Eq. 2.4 is then that the mean free path ℓ_{mf} should be larger than the p-n junction width L. Crucially, it was noticed from the first experiments that disordered graphene p-n junctions in general are less resistive than ballistic ones [58, 78], providing a metric for experimental progress. To fulfill $\ell_{mf} > L$, experimental designs have tried to maximize device mobility while minimizing dielectric thickness, which controls the electric field the p-n junction. Efforts to achieve high mobility locally gated structures have been manifold, encompassing a zoo of gate dielectrics including cross-linked PMMA [58, 63, 79], buffered [10, 59, 80] and direct [81] atomic layer deposited high-κ oxides, evaporated SiO_2 [82, 83], vacuum [61, 62], and single crystal hexagonal boron nitride [19]. These various techniques lead to mobilities between 100 and 10,000 $cm^2/V{\cdot}sec$ and effective dielectric thicknesses between 5-300 nm.

The typical experimental geometry for studying transport in graphene p-n junctions presents a challenge for quantitative study due to the series resistance of the graphene leads (GLs), which contribute to the total resistance even in four terminal measurement schemes. As the voltages on the local top gate and global back gate are tuned, the densities in the locally gated region (LGR)

under the top gate and the graphene leads—the region between the top gate and metal contacts—can be independently tuned, approximately over a range $|n| < 10^{13}$ cm^{-2}. Experimental results for non-phase coherent pnp structures junctions can be summarized by the statement that resistance of the device is higher in the presence of p-n junctions; i.e., $R_{p(-|n|)p} > R_{p(|n|)p}$. Because even in diffusive devices the resistance of graphene increases with decreasing doping, the higher resistance of p-n junction containing channel is not in itself necessarily a consequence of Eq. 2.4. Rather, quantitative analysis of the p-n junction resistance is required.

Due to the electron-hole symmetry of the band structure, the resistance of graphene in most experiments is roughly symmetric with respect to charge conjugation, $R(|n|) \approx R(-|n|)$. This fact can be used to extract the resistance of the p-n junction itself by constructing the 'odd' resistance, $R_{Odd} = R_{p(-|n|)p} - R_{p(|n|)p}$ [58], which measures the isolated resistance of the p-n junctions for potential profiles not too different from those of a parallel plate capacitor. For p-n junctions much shallower than the mean free path ($\ell_{mf} \lesssim L$), charge carriers equilibrate constantly along the channel via scattering; the resulting resistance can be explained by a phenomenological model that takes into account the position dependence of the density and, by extension, the resistivity, $R = \int \rho(x)dx$, $\rho(x) = (\sigma_0^2 + (n(x)e\mu)^2)$ where σ_0 is the fitting parameter corresponding to the minimal conductivity [58]. Early experiments were all firmly in the diffusion dominated limit [58–60, 84].

Subsequently, simultaneous attempts were made to study Klein phenomena by narrowing the p-n junctions and pnp structures [10, 63] as well as by increasing the device mobility by using air-bridge top gates [61, 62]. In both approaches, the details of the potential profile—which, given the inherent requirement that the dielectric thickness be comparable to the length of the top gated

region, deviate strongly from the parallel plate capacitor model—are crucial in analyzing the data in terms of Klein tunneling. This is due to the fundamental problem that in the presence of any scattering, the ballistic and diffusive contributions to the conductance cannot be reliably separated. Nevertheless, in the best samples, a good agreement with the Eq. 2.4 was found [62, 63].

2.1.4 Phase coherent transport in ballistic Fabry-Perot cavities

Transport measurements across single p-n junctions, or a pnp junction in which transport is not coherent, can at best provide only indirect evidence for Klein tunneling by comparison of measured resistance of the p-n junction or junctions against Eq. 2.4. Moreover, because such experiments probe only incident-angle averaged transmission, they cannot experimentally probe the structure $T(\theta)$. Thus, although references [62] and [52] show that the resistance of nearly ballistic p-n junctions are in agreement with the ballistic theory, to show that angular collimation occurs, or that there is perfect transmission at normal incidence, requires a different experiment. In particular, there is no way to distinguish perfect transmission at $\theta = 0$ from large transmission at all angles, begging the question of whether "Klein tunneling" has any observable consequences outside the context of an angle resolved measurement or its contribution to bulk properties such as the minimal conductivity. In fact, as was pointed out by Shytov et al. [49], an experimental signature of this phenomenon should manifest as a sudden phase shift at finite magnetic field in the transmission resonances in a ballistic, phase coherent, graphene pnp device.

Although graphene p-n junctions are transmissive when compared with p-n junctions in gap-full materials (or gapless materials in which backscattering is allowed, such as bilayer graphene), graphene p-n junctions are sufficiently reflective, particularly for obliquely incident carriers, to

cause transmission resonances due to Fabry-Perot interference. However, in contrast to the canonical example from optics, or to one dimensional electronic analogues [85], the relative phase of interfering paths in a ballistic, phase coherent pnp (or npn) graphene heterojunction can be tuned by applying a magnetic field. In this section I will describe the observation of conductance oscillations in extremely narrow graphene heterostructures where a resonant cavity is formed between two electrostatically created bipolar junctions. Analysis of the oscillations confirms that p-n junctions have a collimating effect on ballistically transmitted carriers[47, 57]. The phase shift observed in the conductance fringes at low magnetic fields is a signature of the perfect transmission of carriers normally incident on the junctions[86] and thus constitutes a direct experimental observation of "Klein Tunneling."[43, 45]

Previous experiments on graphene p-n junctions [14, 58–63, 87] were limited in scope by the diffusive nature of the transport beneath the local electrostatic gates; we overcome such limitations by fabricating extremely narrow ($\sim$20 nm) local gates strongly capacitively coupled to the graphene channel (Fig. 2.3a-b). Graphene sheets were prepared by mechanical exfoliation on Si wafers covered in 290 nm thermally grown SiO_2. Ti/Au contacts 5 nm/35 nm thick were deposited using standard electron beam lithography, and local gates subsequently applied using a thin (~ 10 nm) layer of hydrogen silsesquioxane (HSQ) as an adhesion layer[60] for low-temperature atomic layer deposition of 20 nm of HfO_2, a high-k dielectric ($\varepsilon \sim 12$) (see Fig. 2.3b). Palladium top gates not exceeding 20 nm in width were deposited in order to ensure that a sizeable fraction of conduction electrons remained ballistic through the LGR. Leakage current was measured to be ≤ 100 pA up to $V_{TG} = \pm 15$ V. All data except Fig. 2.6c was taken from the device depicted in Fig 2.3a, which had a measured mobility $\sim$ 5,000 cm^2/V sec. The conductance of the graphene devices was

measured in a liquid helium flow cryostat at 4.2- 100 K using a standard lock-in technique with a current bias of .1-1 μA_{rms} at 17.7 Hz. Unless otherwise specified, all measurements were done at 4.2 K. The ratio $C_{TG}/C_{BG} \approx 12.8$, with C_{TG} and C_{BG} the capacitances of the top and back gate, respectively, was determined from the slope of the Dirac ridge with respect to the applied voltages, and similar values were obtained from the analysis of the period of the Shubnikov-de Haas oscillations in magnetic field, which also served to confirm the single layer character of the devices.

Finite element electrostatics simulations were carried out for the measured device geometries described above with the thickness and dielectric constant of the HSQ adjusted such that the simulations matched the observed values of C_{TG}/C_{BG}. The shape of the potential and the strength of the electric field E used in fitting the experimental data were constrained to lie within the confidence interval of the simulations, which in turn were largely determined by uncertainty in the device geometry. Electrostatics simulations based on finite element analysis show that the carrier densities in the locally gated region (LGR) and the 'graphene leads' (GL)—n_2 and n_1, respectively—can be controlled independently by applying bias voltages to the top gate (V_{TG}) and the back gate (V_{BG}). The width of the LGR, L, is defined as the distance between the two zero density points. As in previous studies[60], the conductance map as a function of V_{TG} and V_{BG} (Fig. 2.3c) can be partitioned into quadrants corresponding to the different signs of n_1 and n_2, with a lowered conductance observed when $n_1 n_2 < 0$. The mean free path in the bulk of the sample, $l_m \gtrsim$100 nm, was extracted from the relation $\sigma = \frac{2e^2}{h} k_F l_m$ between the conductivity and Fermi momentum, k_F. Since $L \lesssim 100$ nm within the experimentally accessible density regime, we expect a significant portion of the transport to be ballistic in the LGR.

In the bipolar regime, the diffusive resistance of the LGR is negligible in comparison with the highly resistive p-n junctions; as a result, the conductance does not increase with increasing magnitude of the charge density in the LGR.[62] We note that the magnitude of this conductance step is only $\sim 60\%$ as large as expected for a fully ballistic heterojunction even after taking into account the enhancement of the junction transparency due to nonlinear screening;[88] this suggests that there is still a large diffusive component to the transport through the heterojunction. Nevertheless, each trace exhibits an oscillating conductance as a function of V_{TG} when the carriers in the LGR and GL have opposite sign.

The regular structure of these oscillations is apparent when the numerical derivative of the measured conductance is plotted as a function of n_1 and n_2 (Fig. 2.3a). While there is a weak dependence of the oscillation phase on n_1 reflecting the influence of the back gate on the heterojunction potential profile, the oscillations are primarily a function of n_2, confirming their origin in cavity resonances in the LGR. The oscillations, which arise due to interference between electron waves in the LGR, are not periodic in any variables due to the strong dependence of the LGR width, L, and junction electric field, E, on the device electrostatics. Still, the conductance maxima are separated in density by roughly $\Delta\ n_2 \sim 1 \times 10^{12}$ cm^{-2}, in agreement with a naive estimate $\Delta\ n_2 \sim \frac{4\sqrt{\pi n_2}}{L}$ for the resonant densities in a cavity of width $L \sim 100$ nm. The application of an external magnetic field shifts the phase of the oscillations, with individual oscillation extrema moving towards higher density $|n_2|$ and the transmission resonances appearing to be adiabatically connected to the high field Shubnikov-de Haas oscillations (Fig.2.5d).

In the context of the graphene p-n junction, this "Klein tunneling" manifests as the combination of the absence of backscattering with momentum conservation parallel to a straight p-n

interface: normally incident particles, bound to conserve their transverse momentum, $k_y = 0$, and forbidden from scattering directly backwards, are predicted to tunnel through such symmetric potential barriers with unit probability. In contrast, particles obliquely incident on a barrier which is smooth on the atomic lattice scale encounter classically forbidden regions where the real part of the perpendicular momentum vanishes. These regions, which form about the center of individual p-n junctions, transmit obliquely incident carriers only though quantum tunneling, leading to an exponential collimation of ballistic carriers passing through graphene pn junctions as per Eq. 2.3 [57]. The quantum interference experiments presented in this section allow a measurement not only of the magnitude but also the phase of the transmission and reflection coefficients. Interestingly, whereas the bulk of conduction in a fully ballistic graphene p-n junction is expected to be dominated by normally incident carriers, the absence of backscattering precludes the contribution of such trajectories to the Fabry-Perot resonances due to perfect normal transmission at both interfaces. Rather, the oscillatory conductance receives its largest contributions from particles incident at angles where neither the transmission probability, $|T^2|$, nor the reflection probability, $|R|^2 = 1 - |T|^2$, are too large (see, e.g., marker 1 in Fig. 2.3c). Only transmission near such angles contributes to the oscillatory conductance, ensuring the survival of the oscillations despite the incident angle averaging and allowing the determination of the width of the angle of acceptance of an individual collimating p-n junction.

In a ballistic heterojunction, the application of a magnetic field bends the carrier trajectories, resulting in an addition of an Aharonov-Bohm phase to the interference and a modification of the angle of incidence at each pn junction. As was pointed out recently[86], such cyclotron bending provides a direct experimental signature of reflectionless tunneling, which manifests as a phase

shift in the transmission resonances of a ballistic, phase coherent, graphene heterojunction at finite magnetic field. These resonances are described by the etalon-like ray tracing diagrams shown in Fig 2.5b. The Landauer formula for the oscillating part of the conductance is obtained from the ray tracing scheme shown in Figure 2.5b. The transmission amplitude through the entire junction is taken to be a product of the transmission amplitudes at the two interfaces with a phase factor corresponding to the semiclassical phase accumulated between the junctions. This semiclassical phase difference for neighboring trajectories is

$$\theta_{WKB} = \mathrm{Re} \int_{-L/2}^{L/2} \sqrt{\pi |n(x)| - \left(k_y - \frac{e}{\hbar} Bx\right)^2}, \tag{2.5}$$

where we take the real part to account for the fact that in general the classical turning points shift from their values of $\pm L/2$ defined for $k_y = 0$, $B = 0$. In addition, there is a nonanalytic part of the phase associated with the the vanishing of the reflection coefficients at opposite interfaces [86] which can be nontrivial at finite magnetic field,

$$\Delta\theta_{rf} = \pi \left(H\left(-k_y + \frac{eBL}{2\hbar}\right) - H\left(-k_y - \frac{eBL}{2\hbar}\right)\right), \tag{2.6}$$

where $H(x)$ is the step function ($H(x) = 1$ for $x > 0$, $H(x) = 0$ otherwise). This phase jump is equivalent to a sign change in the reflection coefficient as the incidence angle crosses zero, and implies that the transmission probability at normal incidence is unity.

At a p-n junction, assumed to be smooth on the lattice scale, the transmission amplitude is exponentially peaked about normal incidence. [57] The principal effect of a weak magnetic field on the transmission through a single p-n junction is to modify the incident angle at the two junctions

due to cyclotron bending of the trajectories. Choosing the Landau gauge where $\vec{A} = Bx\hat{y}$ with k_y the conserved transverse momentum in the center of the junction ($x = 0$), the transmission and reflection amplitudes at the junctions located at $x = \pm L/2$ are [86]

$$T_{\pm} = \exp\left(-\frac{\pi\hbar v_F}{2eE}\left(k_y \pm \frac{eBL}{2\hbar}\right)^2\right) \qquad R_{\pm} = \exp\left(i\pi H\left(-k_y \mp \frac{eBL}{2\hbar}\right)\right)\sqrt{1-|T_{\pm}|^2} \tag{2.7}$$

Defining the total phase $\theta = \theta_{WKB} + \Delta\theta$, and taking into account the damping, due to scattering, of the particle propagators between the junctions, we can write the Landauer conductance of the heterojunction via the canonical Fabry-Perot formula as

$$G = \frac{4e^2}{h}\sum_{k_y}\left|\frac{T_+T_-}{1-|R_+||R_-|e^{i\theta}}\right|^2 \tag{2.8}$$

It is difficult to separate diffusive from ballistic effects in the bulk conductance. However, the contribution of diffusive effects to quantum interference effects are strongly suppressed at $B = 0$, rendering useful the definition $G_{osc} \equiv G - \overline{G}$, where $\overline{G}$ denotes the conductance averaged over the accumulated phase. Multiple reflections are suppressed both by the finite mean free path as well as the collimating nature of the junctions; as $|T_{\pm}|, |R_{\pm}| \leq 1$, higher order products of transmission and reflection coefficients are necessarily decreasing. Utilizing this fact, we can expand the denominator in Eq. (2.8) and subtract all nonoscillating terms to get the leading contribution to the quantum interference,

$$G_{osc} = \frac{8e^2}{h}\sum_{k_y}|T_+|^2|T_-|^2|R_+||R_-|\cos(\theta)\, e^{-2L/l_{LGR}}. \tag{2.9}$$

where we have introduced the damping factor $e^{-2L/l_{LGR}}$ to account for the loss of ballistic electrons to the diffusive channel due to impurity scattering. This formula does not take into account inhomogeneities in the applied local gate potential due to the uneven width of the top gate or thickness and crystallinity of the dielectric. Such disorder can lead to significant damping of the oscillations even in a completely ballistic sample [86], and makes the estimate for the mean free path derived from matching the observed amplitude of the oscillations a lower bound. Nevertheless, that the mean free path in the LGR is shorter than that in the GL is consistent with experiments which find a strong enhancement of the Raman D-band in graphene after it is covered in HSQ and irradiated with electrons at energies and doses comparable to those used during top gate fabrication. [89]

At zero magnetic field, particles are incident at the same angle on both junctions, and the Landauer sum in Eq. (2.9) is dominated by modes which are neither normal nor highly oblique, as described above. As the magnetic field increases, cyclotron bending favors the contribution of modes with $k_y = 0$, which are incident on the junctions at angles with the same magnitude but opposite sign (see marker 2 and 3 in Fig.2.5b). In the case of perfect transmission at zero incident angle, the reflection amplitude changes sign as the sign of the incident angle changes,[86] causing a π shift in the phase of the reflection amplitudes. Equivalently, this effect can be cast in terms of the Berry phase: the closed momentum space trajectories of the modes dominating the sum at low field and high k_y do not enclose the origin, while those at intermediate magnetic fields and $k_y \sim 0$ do (Fig. 2.3b). Due to the Dirac spectrum and its attendant chiral symmetry, there is a topological singularity at the degeneracy point of the band structure, $k_x = k_y = 0$, which adds a non-trivial Berry phase of π to trajectories surrounding the origin. As a consequence, the

quantization condition leading to transmission resonances is different for such trajectories, leading to a phase shift in the observed conductance oscillations (i.e., a π jump in $\Delta\theta_{rf}$) as the phase shifted trajectories begin to dominate the Landauer sum in Eq. (2.9).[4, 5] For the electrostatics of the devices presented in this section, the magnetic field at which this phase shift is expected to occur is in the range $B^* = \sim$250–500 mT, in agreement with experimental data (see Fig. 2.6). As the magnetic field increases further, the ballistic theory predicts the disappearance of the Fabry-Perot conductance oscillations as the cyclotron radius, R_c, shrinks below the distance between p-n junctions, $R_c \lesssim L$, or B$\sim$ 2 T for our devices. We attribute the apparent continuation of the oscillations to high magnetic field to the onset of disorder mediated Shubnikov-de Haas type oscillations within the LGR.

In order to analyze the quantum interference contribution to the ballistic transport, we extract the oscillating part of the measured conductance by first antisymmetrizing the heterojunction resistance[58] with respect to the density at the center of the LGR, $G_{odd}^{-1}(|n_2|) = G^{-1}(n_2) - G^{-1}(-n_2)$, and then subtracting a background conductance obtained by averaging over several oscillation periods in n_2, $G_{osc} = G_{odd} - \overline{G_{odd}}$. The resulting fringe pattern shows a marked phase shift at low magnetic field in accordance with the presence of the Klein backscattering phase, with two different regions—of unshifted and shifted oscillations—separated by the magnetic field B^* (see Fig 2.6a). To perform a quantitative comparison between the measured G_{osc} and Eq. (2.9), we first determine the potential profile in the heterojunction devices from numerical electrostatics simulations, which information is then input into (2.9) to generate a fringe pattern for comparison with experimental data. We choose the free fitting parameter $l_{LGR} = 67$ nm for this comparison to best fit the oscillation amplitudes. Considering possible degradation of the graphene in and around

the LGR during the fabrication of the local gates,[89] this value is consistent with the estimate for the bulk mean free path. The resulting theoretical calculation exhibits excellent quantitative agreement with the experimental result at both zero and finite magnetic field (Fig. 2.6a-b) both in the magnitude and period of the oscillations. We emphasize that the value of L—which largely determines both the phase and amplitude of the oscillations—varies by almost by a factor of three over the accessible density range, yet Eq. (2.9) faithfully describes the observed experimental conductance modulations in n_2 as well as in B. Such remarkable agreement confirms that the observed oscillatory conductance, which is controlled both by the applied gate voltage and the magnetic field, results from quantum interference phenomena in the graphene heterojunction. Moreover, the oscillations exhibit a phase shift at $B^* \sim 0.3$ T which is the hallmark of perfect transmission at normal incidence, thus providing direct experimental evidence for the "Klein tunneling" of relativistic fermions through a potential barrier.

The measured data can be used to approximately solve the inverse scattering problem. In we Fig. 2.8a we compare the measured data with numerical simulations to extract the strength of the electric field in an individual pn junction. It follows from robust semiclassical arguments [57] that, in the experimentally realized situation of p-n junctions smooth on the scale of the lattice constant, the collimation at an individual junction should be a Gaussian function of k_y (see eq .2.7). The important parameter is the electric field, E, in the junctions, which is given, after taking into account the absence of linear screening in graphene near the charge neutrality point, by [88]

$$eE = 2.1\hbar v_F n'^{2/3}. \tag{2.10}$$

where n' is the density gradient across the junction. As is evident from the simulations (Fig. 2.8c),

the nonlinear screening correction to the electric field gives a better fit to the experimental data than either the non-exponential collimation produced by atomically sharp barriers—which appears to contain higher order resonances—or the weaker field that results from neglecting nonlinear screening near the Dirac point.

To make this comparison more quantitative, we perform several simulations in which the nonlinear screening result, (2.10), is scaled by some prefactor, η. For a rough comparison, the linear screening corresponds to $\eta \lesssim .5$, while the step potential corresponds to $\eta \gg 20$. As explained in the main text, the magnetic field dependence contains an abrupt phase shift at finite magnetic field as the finite k_y modes cease to contribute to the oscillations and $k_y = 0$ modes—which carry with them the additional Berry phase of π—become the dominant contribution to the oscillatory conductance. With increasing magnetic field, a fully ballistic model predicts the gradual ebbing of these phase shifted oscillations as the cyclotron radius becomes comparable to the junction size. The field at which the π-phase shift manifests is tied to the degree of collimation of the transmission at each p-n interface. Because this phase shift is rather abrupt, we can define the transition magnetic field, B^*, as the field at which the values of the the oscillation prefactor $|T_+|^2|T_-|^2|R_+||R_-|$ for zero and finite k_y modes become comparable, giving $B^* \propto \sqrt{\frac{\hbar e E}{e^2 v_F L^2}}$. Since B^* depends strongly on the junction electric field, it allows us to extract this field from the experimentally observed oscillation phase shift. Defining B^* as the field at which $G_{osc}(n_2, B = B^*) = 0$ for fixed density n_2 such that $G_{osc}(n_2, B = 0)$ is an extremum, we can estimate $\eta = .9 \pm .3$.

In accordance with the ballistic theory, the oscillations peak at zero magnetic field, and then have a second maximum after the phase shift at finite magnetic field. The relative height of these

two maxima can be used to estimate the electric field E. Higher collimation suppresses the contribution of the modes near $k_y = 0$ at finite B, since this feature is entirely generated by modes not normally incident at either interface. Higher collimation thus corresponds to an effectively more one-dimensional channel for interference effects, leading to the more effective destruction of the oscillations by the Lorentz force, which serves to push the particles out of the narrower acceptance angles at each junction. By taking the average value of G_B^{Max}/G_0^{Max} and comparing it with the simulations for a variety of values of η, we can extract $\eta \approx 1.6 \pm .3$. We note that the apparent discrepancy between this and the method previously outlined is likely due to the contribution of momentum non-conserving processes to the oscillations at finite B, leading to an overestimate of η. While neither of the methods above is free of systematic errors, they confirm the importance of nonlinear screening in determining transport through graphene p-n junctions.

Finally, we turn our attention to the temperature dependence of the quantum coherence effects described iabove, which we observe at temperatures as high as 60 K (Fig. 2.6d). An elementary energy scale analysis suggests that the phase coherence phenomena should be visible at temperatures of order $\frac{\hbar v_F}{L} \sim 100$ K, when thermal fluctuations become comparable to the phase difference between interfering paths. In addition, the oscillation amplitude is sensitive to the carrier mean free path, and we attribute the steady waning of the oscillations with temperature to a combination of thermal fluctuations and further diminution of the mean free path by thermally activated scattering. The mean free path in clean graphene samples can be as large as $\sim$1 μm,[90] and a reduction of the width of the heterostructure L by an order of magnitude is well within the reach of modern fabrication techniques; consequently, technological improvements in the fabrication of

graphene heterojunctions should lead to the observation and control of quantum coherent phenomena at much high temperatures, a crucial requirement for realistic, room temperature quantum device applications.

2.2 Unipolar junctions: Landau level collapse

In the intermediate magnetic fields where the cyclotron orbit becomes smaller than the carrier mean free path, Landau level quantization is appreciable but QHE does not yet emerge. In the presence of an inhomogenous potential profile such as exists in the presence of a local top gate, this regime allows the investigation of the interplay between perpendicular magnetic and in-plane electric fields in graphene. In particular, in was noticed by Lukose and collaborators [72] that the emergent Lorentz symmetry of the single particle graphene Hamiltonian, Eq. 1.1 allows for a transformation of magnetic into electric fields. They identified two regimes for a 1D linear potential $U(x) = -eEx$, in analogy with relativistic electromagnetism. For $\beta \equiv \frac{cE}{v_f B} < 1$, the electric field can be eliminated by a "Lorentz boost" in which the speed of light parameter equal to the Fermi velocity in graphene, v_f. The electronic spectrum in this regime is discrete, and is described by Landau levels with a spectrum modified by the in plane electric field, $\varepsilon \propto \sqrt{Bn}(1-\beta^2)^{3/4}$. As the magnetic field is lowered, or the electric field increases, the Landau levels collapse, leading to a continuous spectrum for $\beta \geq 1$. In this regime, it is the magnetic field that can be eliminated [32, 86], leading to the prediction of an anomalous magnetoconductance of ballistic graphene p-n junctions, $G(B) = (1-\beta^2)^{3/4}$. Unfortunately, experimental evidence for this is complicated by the increased importance of impurity scattering at intermediate and high magnetic fields [58].

This collapse of the Landau levels has other experimental consequences. In transport, Shubnikov de Haas type resonances occur at when closed orbits fulfill a a Bohr-Sommerfeld quantization condition $\int_{x_1}^{x_2} p_x(x)dx = \pi(n+1/2-\gamma)$, where x_1 and x_2 are the two classical turning points, n is an integer, and the Berry phase contribution γ is $1/2$ for the Dirac fermions in graphene. In

the presence of an inhomogenous potential, we can introduce the position-dependent Fermi momentum, $k_F(x) = (\varepsilon - U(x))/v_F$, we obtain (for monolayer graphene)

$$\int_{x_1}^{x_2} \sqrt{(k_F(x))^2 - (p_y - eBx)^2} dx = \pi n. \tag{2.11}$$

For linear $U(x)$, this gives the Landau level spectrum (2) for $B > B_c$. As B approaches B_c, one of the turning points moves to infinity, indicating a transformation of closed orbits into open trajectories [13]. The experimental consequence is that, in the presence of a potential barrier, SdH resonance, rather than tracing lines towards zero field and zero density, should abruptly terminate at some finite magnetic field.

To realize the collapse of Landau levels in an electron system, several conditions must be met. First, it must be possible to create a potential barrier that is steep on the scale of the cyclotron orbit radius. Second, the system must be ballistic on this length scale, in order to suppress the broadening of Landau levels due to disorder. The experimental observation of the LL collapse in the intermediate magnetic field regime was reported [10] and explained [13] recently in the same devices in which FP oscillations are observed. The effect occurs in the unipolar regime, where the narrow potential barrier is repulsive and competes with magnetic confinement. Landau level collapse corresponds to a deconfinement transition as the field is lowered. The observed transport measurements exhibit Shubnikov-de Haas (SdH) oscillations which, in the unipolar regime, abruptly disappear when the strength of the magnetic field is reduced below a certain critical value. This behavior is explained by the semiclassical analysis of the transformation of closed cyclotron orbits into open, deconfined trajectories (Fig. 2.9).

Another experimental consequence of Landau level collapse in graphene is a modification of

cyclotron resonance in the presence of an in-plane electric field. The well known Kohn's theorem for cyclotron resonance [91] states that for particles with a parabolic spectrum, in-plane fields—including those due to Coulomb interactions between particles—do not affect the cyclotron resonance frequencies. This theorem rests on Galilean invariance of the single particle continuum theory—a condition that is explicitly violated in graphene—and both theorists and experimentalists have taken this as cause to use cyclotron resonance as a probe of many body effects in graphene [92–94]. The strong electric fields present in graphene p-n junctions, however, offer another venue in which to observe violation of Kohn's theorem.

The same Lorentz transformation used in [72] to eliminate and in-plane electric field can be used in to remove the built in p-n electric field. In the presence of a time dependent perturbation representing the electromagnetic radiation used to perform cyclotron resonance experiments, the result is a spatial dependence of the perturbation, $H' \propto e^{i\omega t} \rightarrow e^{i\omega(t-\beta x/v_F)}$. Expressing the coordinate in terms of creation and annihilation operators in the space of Landau Levels,$\hat{a}$ and $\hat{a}^\dagger$, it becomes clear that the perturbation mixes all Landau levels, $H' \propto \sum_{n,m} c_{nm}(\hat{a})^n(\hat{a}^\dagger)^m$ with a suitable choice of the constants c_{nm} [95]. The conclusion is that a static electric field changes the selection rules for cyclotron resonance, in addition to collapsing the spectrum. While far field cyclotron resonance measurements [94, 96] cannot hope to detect a signal from the tiny region of a p-n junction, there is some hope that newly available tip assisted infrared spectroscopy [97] might be applied to probe this emergent quasi-relativistic Lorentz physics in graphene.

2.3 Reaching for the ballistic limit with Si/SiO_2 nanowire gates

The temperature dependence of the Fabry-Perot oscillations raises the question of the ultimate limit for quantum coherent transport in graphene. One factor that surely limits the device performance at low temperatures is the effective size of the Fabry-Perot cavity, roughly estimated as $T^* \sim \hbar v_F/L$, where L is the cavity width. Pushing this energy scale as high as room temperature is a challenge for conventional lithographics techniques. We circumvent conventional lithographic limits by using Si/SiO_2 core-shell nanowires to create extremely narrow top gates. The nanowires are 25-50 nm in diameter, and are covered in 2-3 nm of native silicon oxide, which forms the gate dielectric. The nanowires are deposited on the graphene in two ways. The first method is AC dielectrophoresis[98]. A large electrode is deposited parallel to but separated from the graphene flake edge at a distance of $\sim$2 μm. A large AC voltage (5 V at 10 kHz) is applied to the electrode and the chip is immersed in a suspension of nanowires in isopropyl alcohol. The graphene flake is monitored in real time in an optical microscope until a suitable nanowire is seen attached to the dielectrophoresis electrode and spanning the graphene. Method two relies on the mechanical transfer process described in chapter 2: the nanowires are dispersed in IPA and dropped onto a polymer-stack, after which the stack is removed and the nanowires transfered to a graphene piece.

Figure 2.10 shows an electron micrograph of a nanowire gated device (in this case produced by method 1). Transport data at zero magnetic field shows high-contrast, large period conductance oscilaltions in the bipolar regime. The narrower cavity means that a much larger change in density under the top gate is required to shift the phase accumulated between the pn junction by the same amount, leading to larger period oscillations; meanwhile, the narrowness of the cavity also increases the amplitude by increasing the ratio L/ℓ_{mf}.

We fabricated both mono- and bilayer devices. Fig. 2.11 shows the magnetic field dependence of the Fabry-Perot oscillations for mono- and bilayer devices. As with the lithographically patterned samples, FP oscillations in the monolayer show a marked Klein tunneling phase shift[10, 11, 86]. No such phase shift is visible in the bilayer, in line with the absence of a Klein tunneling phase shift for the 2π winding number spectrum[99]. Both data sets show the strong bending of the SdH resonance in the unipolar regime. The presence of LL collapse in both mono- and bilayer is in line with the semiclassical argument of Eq. 2.11, in which the competition between magnetic confinement and electrostatic deconfinement is a generic behavior of a gated 2D electron gas.

Temperature dependence of the Fabry-Perot resonances reveals them to be much more robust than in the lithographically patterned devices. Fig.2.12 shows differentiated conductance maps at difference temperatures for the bilayer graphene nanowire gated device, at a graphene-lead density of n_{BG} $\sim 3.1\times10^{12}$ cm^{-2}. The outstanding question is whether or not the oscillation temperature dependence is accounted for by a simple thermal broadening in the Landauer Formula,

$$G(T) = \frac{4e^2}{h}\int d\varepsilon \left(-\frac{\partial f(\varepsilon,T)}{\partial \varepsilon}\right)\sum_{k_y}|T_{Total}|^2. \tag{2.12}$$

and whether it is indeed possible to resolve this effect at room temperature in yet cleaner, narrower devices.

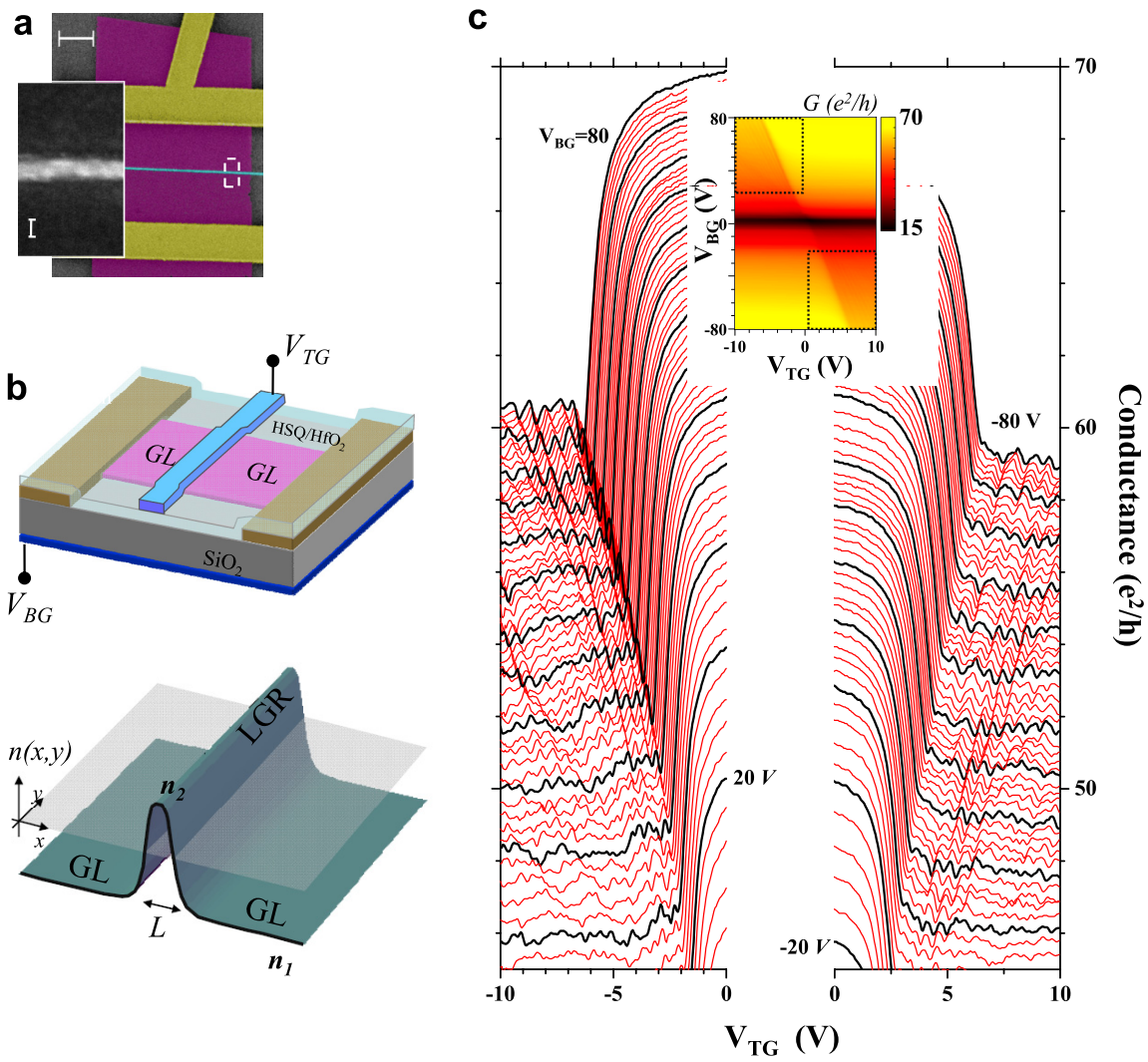

Figure 2.3: Graphene heterojunction device schematics and conductance measurements
a False color scanning electron microscope image of a typical graphene heterojunction device. Electrodes, graphene, and top gates are represented by yellow, purple and cyan, respectively. The scale bar is 2 μm. Inset: high magnification view of top gate. The scale bar is 20 nm. **b** Schematic diagram of the device geometry. The electrostatic potential created by the applied gate voltages, V_{BG} and V_{TG}, can create a graphene heterojunction of width L bounded by two p-n junctions. **c** The inset shows the conductance as a function of V_{TG} and V_{BG}. The main panels show cuts through this color map in the regions indicated by the dotted lines in the inset, showing the conductance as a function of V_{TG} at fixed V_{BG}. Traces are separated by step in V_{BG} of 1 V, starting from ± 80 with traces taken at integer multiples of 5 V in black for emphasis.

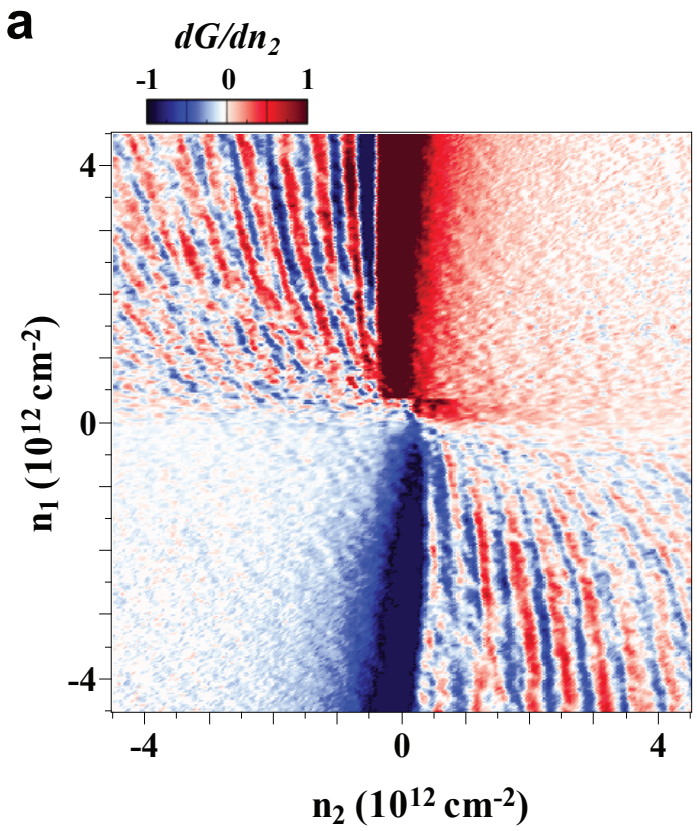

Figure 2.4: Fabry Perot oscillations
dG/dn_2 as a function of the densities in the GLs and LGR, n_1 and n_2. Scale bar is in arbitrary units. Fringes corresponding to the Fabry-Perot oscillations are visible in the regions where $n_1 n_2 < 0$.

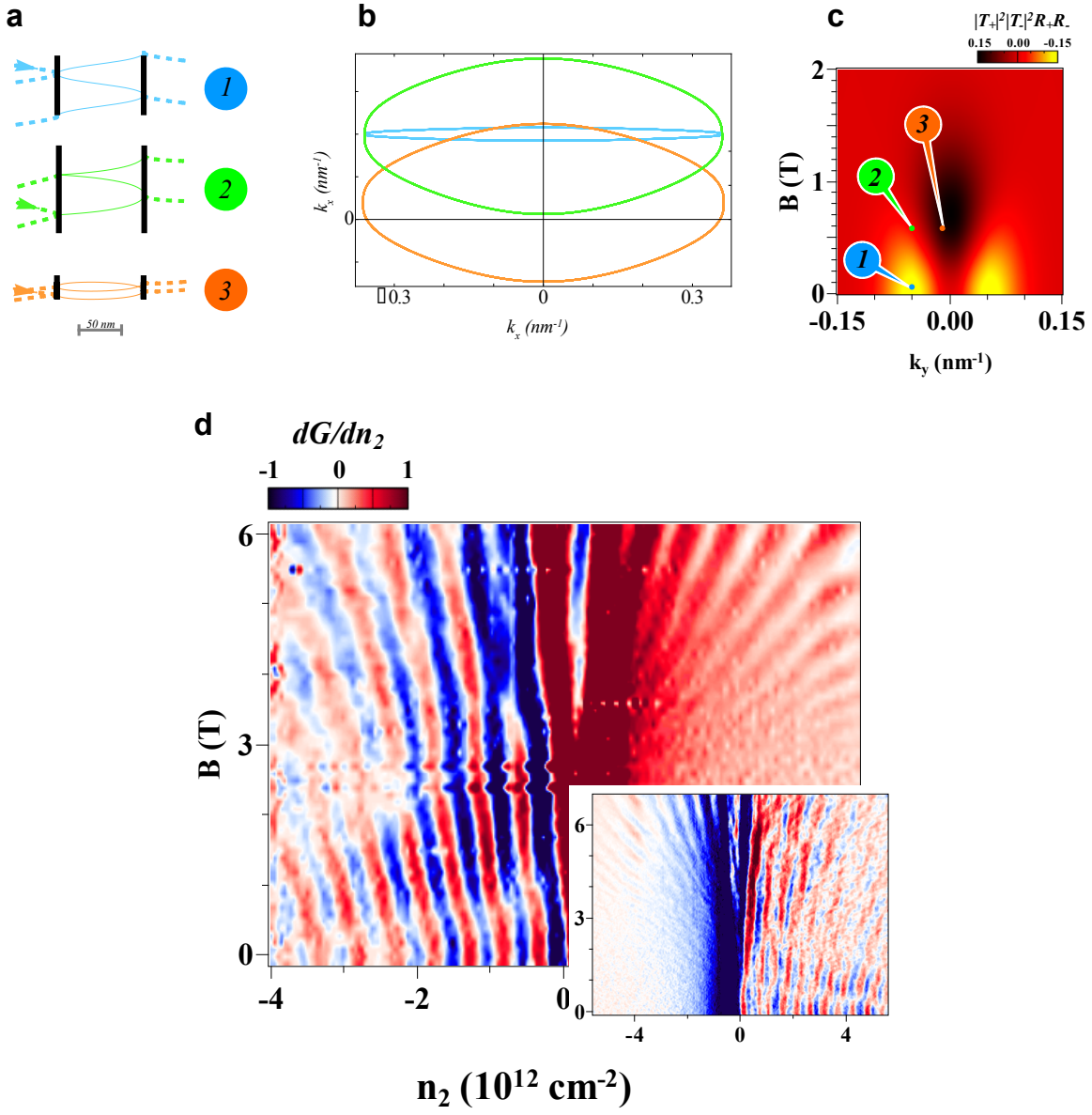

Figure 2.5: Crossover from Fabry Perot to Shubnikov de Haas oscillations
Trajectories contributing to quantum oscillations in real (**a**) and momentum space (**b**). The dominant modes at low magnetic field (1) give way, with increasing B, to phase shifted modes with negative reflection amplitude due to the inclusion of the non-trivial Berry phase (3), near $k_y = 0$. The original finite k_y modes are not yet phase shifted at this field (2), but no longer contribute to the oscillatory conductance due to collimation. **c** The prefactor in the Landauer sum, $|T_+|^2|T_-|^2R_+R_- = |T_+|^2|T_-|^2|R_+||R_-|e^{i\Delta\theta_{rf}}$, as a function of B and k_y, plotted for the V_{BG}=50V and $n_2 = 3.5 \times 10^{12}$ cm^{-2}. Regions of negative sign correspond to trajectories containing the Klein backscattering phase shift. **d** Main panel: Magnetic field dependence of dG/dn_2 at $V_{BG} = 50$ V. Inset: Similar data taken at $V_{BG} = -50$ V. The magnetic phase is proportional to the sign of the carriers; as a result, the oscillation extrema move in opposite directions for opposite signs of carriers in the LGR.

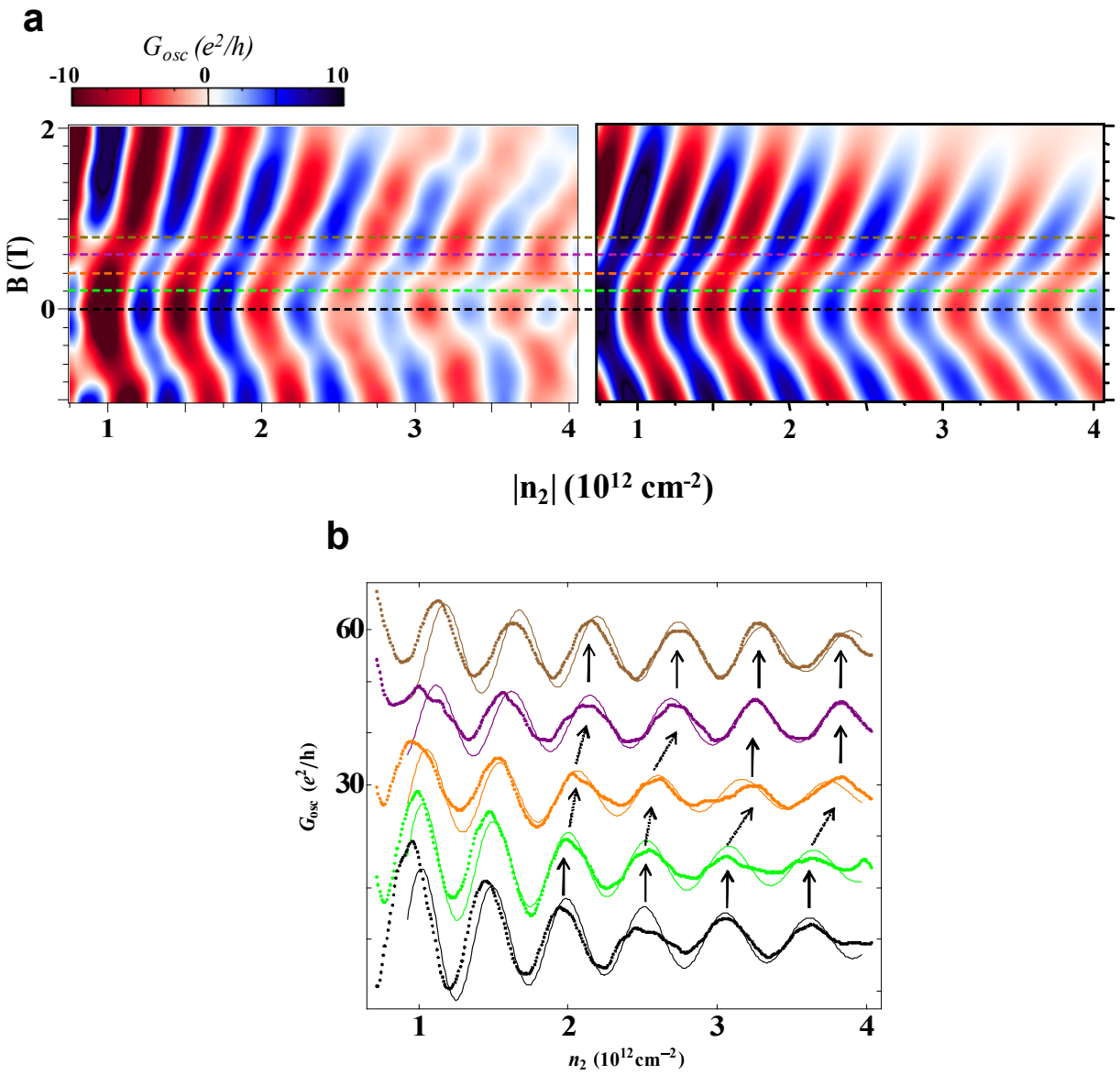

Figure 2.6: Comparison of the Fabry-Perot oscillations with a theoretical model
a Magnetic field and density dependence of the oscillating part of the conductance at $V_{BG} = 50$ V. G_{osc} as extracted from the experimental data (left panel) shows good agreement with a theoretical model accounting for nonlinear screening[88] (right panel) over a wide range of densities and magnetic fields. **b** Cuts taken at $B = 0$, 200, 400, 600, and 800 mT, corresponding to the colored dashed lines in a; the dots represent data, the smooth lines the result of the simulations. The sudden phase shift that signals the presence of perfect transmission is indicated by dashed arrows. Curves are offset for clarity.

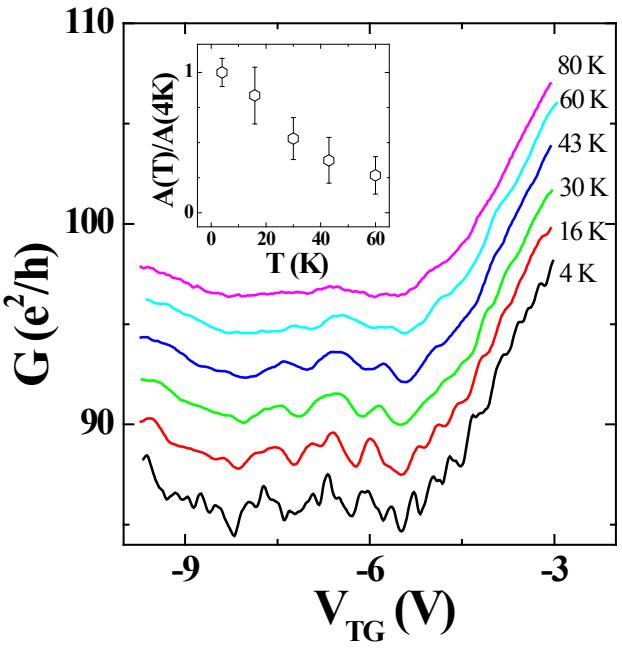

Figure 2.7: Temperature dependence of the Fabry Perot oscillations
Temperature dependence of the oscillation amplitude in a device similar to that presented in the rest of the section. Main panel: The oscillations (different curves are offset for clarity) weaken with rising temperature, and are not observed above 80 K. At 4 K, the conductance modulations contain both the ballistic oscillations as well as aperiodic modulations due to mesoscopic conductance fluctuations which quickly disappear with increasing temperature. Inset: Averaged amplitude of several oscillations, normalized by the amplitude at $T = 4$ K.

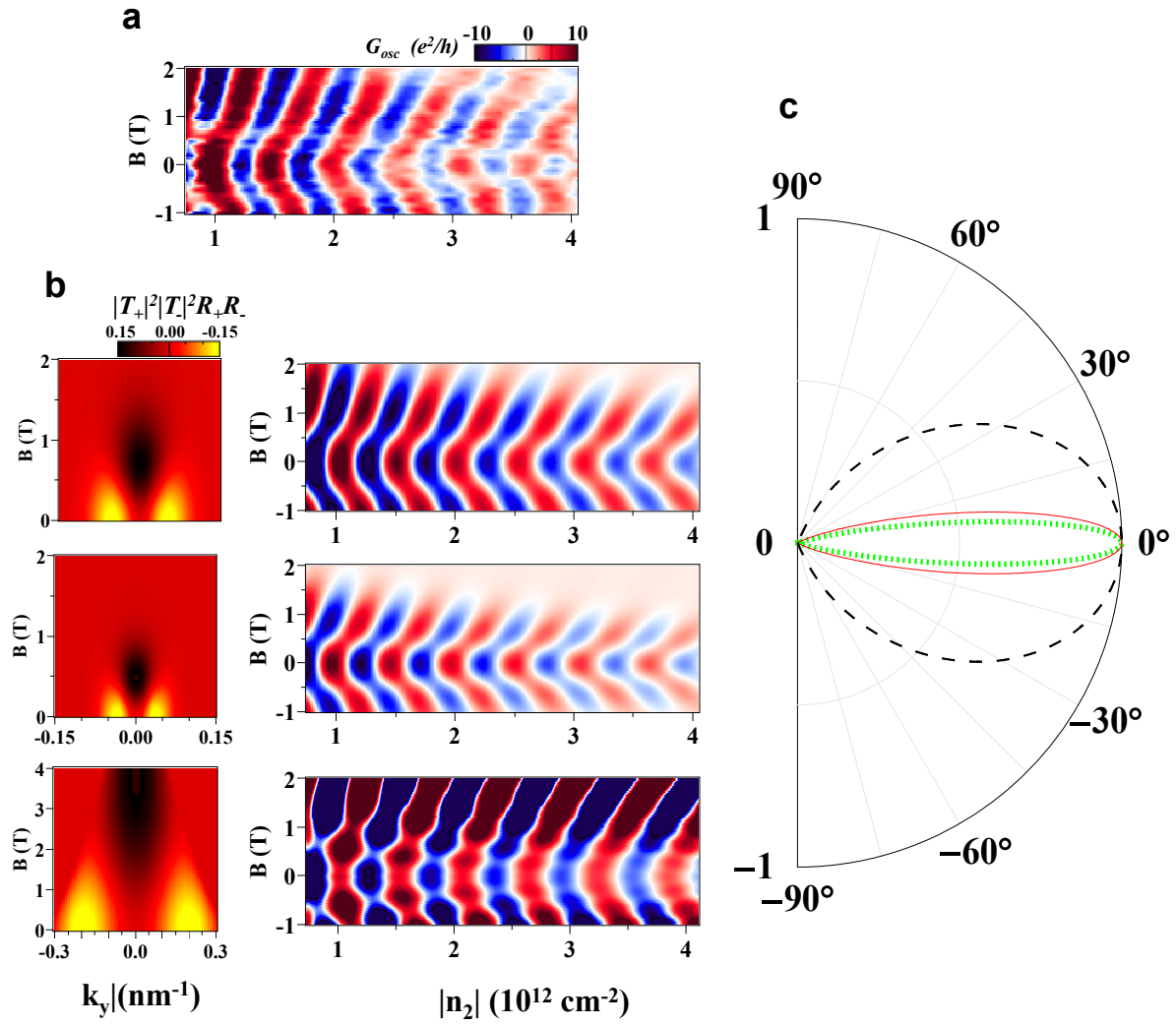

Figure 2.8: Fitting the pn junction electric field from the Fabry-Perot oscillations
a Top panel: oscillatory conductance as a function of n_2 and magnetic field at V_{BG}=50V. **b** The oscillation prefactor $|T_+|^2|T_-|^2R_+R_-$ (column 1) and resulting oscillatory conductance (column 2) as a function of magnetic field for a variety of collimation models. The best fit to the data is achieved by accounting for the nonlinear screening (top panel); the simulations resulting from naively linearizing the potential between the extrema (middle panel) and considering the algebraic collimation resulting from a step potential (lower panel; note the different scale in left) show features incompatible with the observed data. The width of the central region is adjusted to be 46-48 nm in the simulations in order to match the phase of the zero field oscillations. The amplitude is fit by setting the mean free path in the Landauer formula to be 67 nm in the top panel, 60 nm in the central panel, and 300 nm for in the lower panel. **c** Transmission probability as a function of angle at zero magnetic field for the pn junctions with (red, solid) and without (green, dotted) nonlinear screening, and for the step potential (black, dashed).

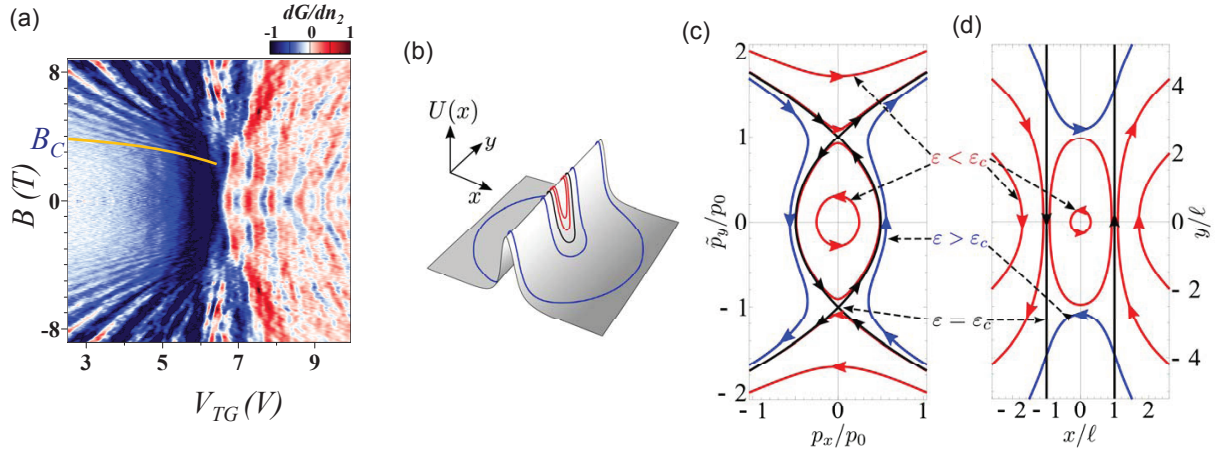

Figure 2.9: Landau level collapse in unipolar graphene junctions
(a) dG/dV_{tg} as a function of B and V_{tg}. Shubnikov-de Haas (SdH) oscillations are observed at high B. The fanlike SdH pattern is altered by the barrier: in the pp'p region it curves, weakens, and is washed out at fields $|B| < B_c$, while in the pnp region a crossover to FP oscillations occurs. Data are taken at $V_{bg} = 70$ V. (b) Closed orbits for the Thomas-Fermi potential obtained from the density profile, with $B = 9, 7, 5, 3, 1$ T and $p_y = 0$. Long trajectories, extending far outside the gated region, do not contribute to SdH oscillations as electrons scatter before completing an orbit. (c) Trajectories for the potential $U(x) = -ax^2$ and $p_y = 0$. Three types of trajectories are shown in momentum space (b) and position space (c): subcritical (red), critical (black), and supercritical (blue). The saddle points in momentum space correspond to motion along straight lines $x = \pm\ell_{mf}$, where the Lorentz force is balanced by the electric field. Reproduced from [13].

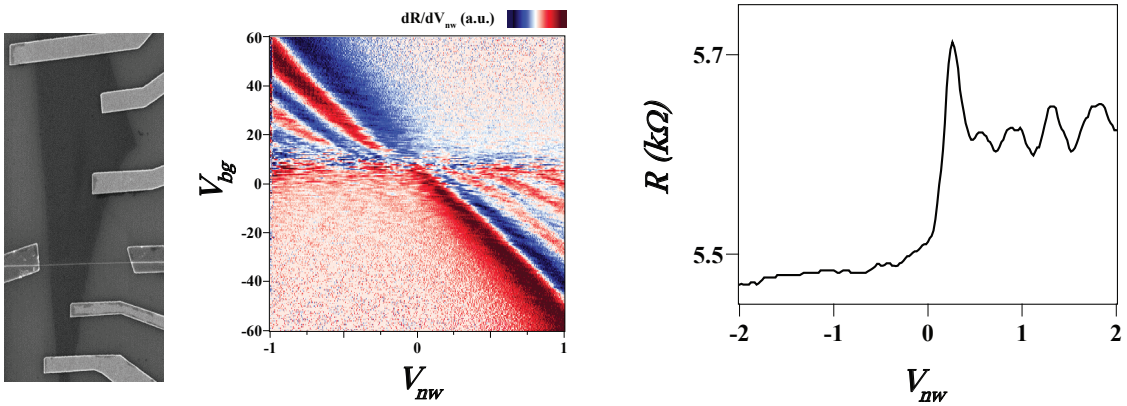

Figure 2.10: Graphene with nanowire gates

Electron micrograph of a naowire gated graphene device. Differentiated conductance dR/dV_{nw} map in the device in the micrograph. Oscilaltions have high contast and large period. The oscillation amplitude is $\sim 20\%$ of the step height, in line with expectations for a ballistic FP cavity.

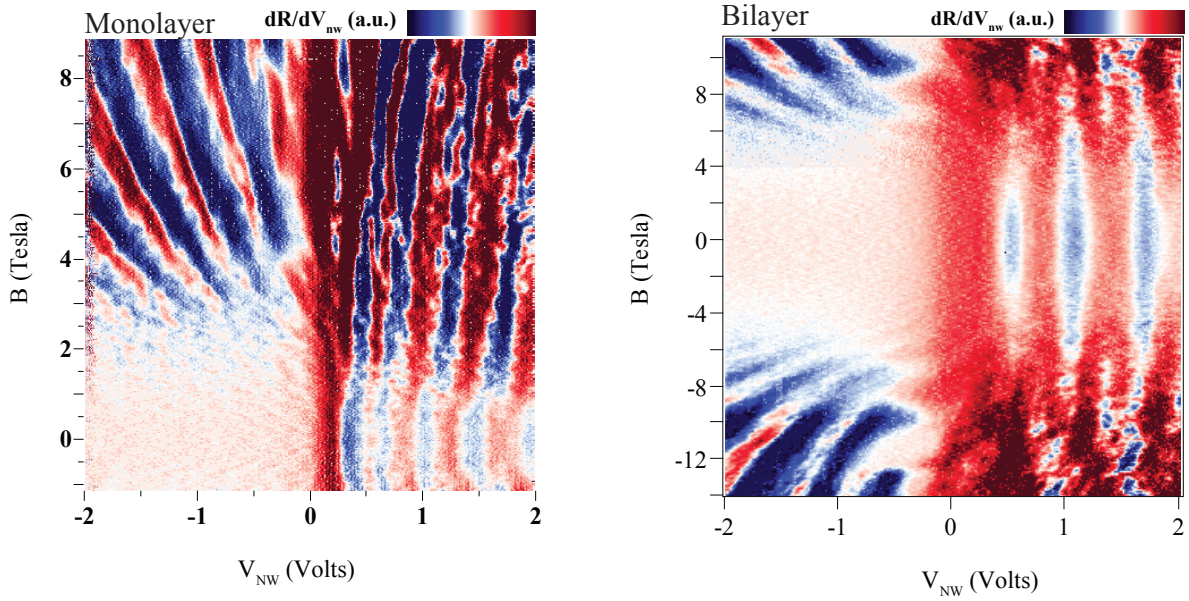

Figure 2.11: Nanowire gated graphene: MLG and BLG FP oscillations
Magnetic field dependence of dR/dV_{nw} in mono- and bilayer graphene devices. The monolayer device was fabricated on SiO_2; the bilayer graphene samples was fabricated on hBN. Sample mobilities were 10,000 and 14,000 for the mono- and bilayer, respectively. Both measurements were performed at T=1.6K.

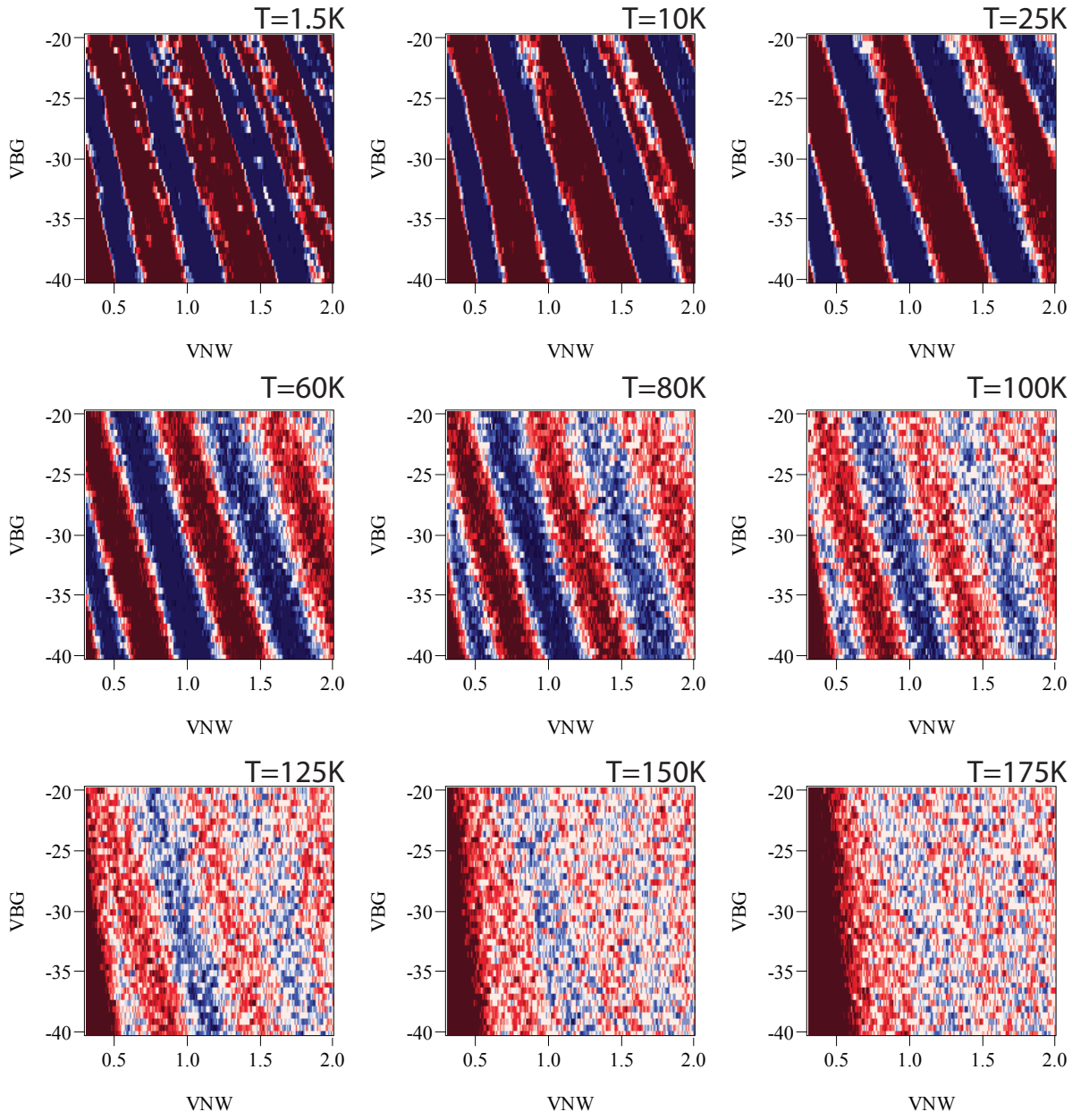

Figure 2.12: Temperature dependence of Fabry Perot oscillations in bilayer graphene I dR/dV_{nw} in the bilayer on hBN device at various temperatures.

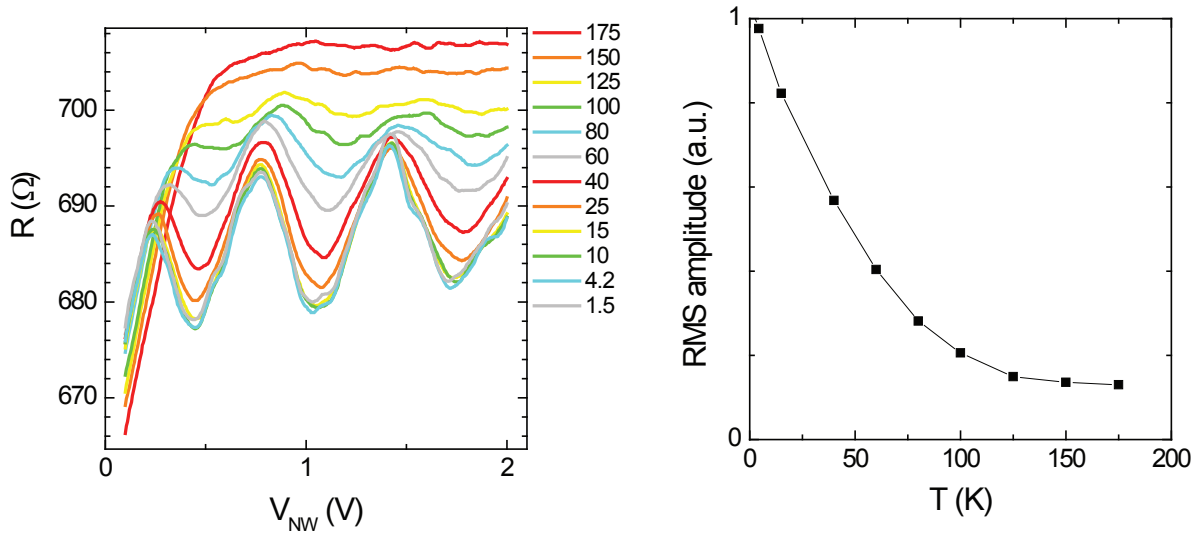

Figure 2.13: Temperature dependence of Fabry Perot oscillations in bilayer graphene II Left: resistance at various temperatures in the FP regime. Right: RMS amplitude of the oscillations, calculated from $\sqrt{\overline{(dR/dV_{nw})^2}}$ over the gate voltage ranges of Fig. 2.12.

Chapter 3

Substrate engineering for high mobility graphene devices

Graphene devices on standard SiO_2 substrates are highly disordered and exhibit characteristics that are far inferior to the expected intrinsic properties of graphene[7, 9, 29, 100–108]. While suspending graphene above the substrate leads to substantial improvement in device quality[109, 110], this geometry imposes severe limitations on device architecture and functionality. There is a growing need, therefore, to identify dielectrics that allow a substrate supported geometry while preserving suspended-like sample quality. Hexagonal boron nitride (hBN) is an appealing alternative to SiO_2 because it has an atomically smooth surface that is relatively free of dangling bonds and charge traps; has a lattice constant similar to that of graphite; and has high energy optical phonon modes and a large electrical band gap. This chapter describes the fabrication of graphene/hBN heterostructures by a mechanical transfer process and the characterization of the simplest of these devices, consisting of exfoliated mono- and bilayer graphene devices on single hBN substrates . Graphene devices on hBN substrates exhibit mobilities and carrier inhomogeneities that are almost

an order of magnitude better than devices on SiO_2. These devices also show reduced roughness, intrinsic doping and chemical reactivity. The ability to assemble crystalline layered materials in a controlled way permits fabrication of graphene devices on other promising dielectrics[111] and allows for the realization of more complex graphene heterostructures. This chapter details the initial discovery of hexa-Boron Nitride as a substrate and complementary dielectric for graphene based electronics. Included are the initial fabrication of graphene on hexagonal Boron Nitride substrates, the first transport measurements, and a brief summary of ongoing projects that utilize the transfer enabled three dimensional architecture. Most of the content was published in reference [40].

3.1 Graphene on hexagonal Boron Nitride

3.1.1 Graphene on hBN device fabrication

The quality of substrate-supported graphene devices has not improved since the first observation of the anomalous quantum Hall effect in graphene and its bilayer [7, 29]. On SiO_2, the carrier mobility is limited by scattering from charged surface states and impurities [100–103, 105], substrate surface roughness[9, 106, 107] and SiO_2 surface optical phonons[104, 105]. Moreover, near the Dirac point substrate-induced disorder breaks up the 2D electron gas (2DES) into an inhomogeneous network of electron and hole puddles[102, 103, 108], while charged impurities trapped in the substrate or at the graphene-substrate interface cause extrinsic doping of the 2DES. So far, efforts to engineer alternatives to SiO_2 have typically involved other oxides, where similar surface effects continue to be problematic[112–114].

Hexagonal boron nitride (hBN) is an appealing substrate dielectric for improved graphene-based devices. hBN is an insulating isomorph of graphite with boron and nitrogen atoms occupying

the inequivalent A and B sublattices in the Bernal structure. The different onsite energies of the B and N atoms lead to a large (5.97 eV) band gap[16] and a small (1.7%) lattice mismatch with graphite[115]. Owing to the strong, in-plane, ionic bonding of the planar hexagonal lattice structure, hBN is relatively inert and expected to be free of dangling bonds or surface charge traps. Furthermore, the atomically planar surface should suppress rippling in graphene, which has been shown to mechanically conform to both corrugated and flat substrates [9, 116]. The dielectric properties of hBN ($\varepsilon \sim 3-4$ and $V_{\text{Breakdown}} \sim 0.7$ V/nm) compare favorably with SiO_2, allowing the use of hBN as a an alternative gate dielectric with no loss of functionality[19]. Moreover, the surface optical phonon modes of hBN have energies two times larger than similar modes in SiO_2, suggesting the possibility of improved high-temperature and high-electric field performance of hBN based graphene devices over those using typical oxide/graphene stacks[14, 73].

Graphene-on-BN devices are fabricated according to the procedure illustrated in Fig. 3.3d: (i) Fabrication begins with the mechanical exfoliation of hBN single crystals onto silicon wafers coated in 285 nm thermal oxide. Graphene is exfoliated separately onto a polymer stack consisting of a water soluble layer, either Mitsubishi Rayon aquaSAVE or poly-vinyl alcohol, and PMMA, and the substrate is floated on the surface of a DI water bath. Later incarnations of the transfer method have involved a variety of other methods as well, including mechanical peeling or direct transfer off a low-stiction substrate, such as PDMS. All thin-film liftoff based transfer methods rely on the same optical Fabry-Perot interference trick responsible for the original isolation of graphene on SiO_2[117]. In addition, we use a band pass filter (λ 562$\pm$ 20 nm) between eyepiece and microscope objective. This allows for use of the thicker substate stacks. For thicknesses larger than$\lambda/4$, different wavelengths of light pick up appreciable different phases, resulting in a loss of

contrast. By restricting the wavelengths, the FP trick can be extended up to large thicknesses (See Fig. 3.2. The polymer stack is tuned to a high intensity contrast for monolayer graphene, but also works for thin hBN or other exfoliatable materials. The graphene layer thickness is occasionally verified by Raman spectroscopy before transfer, although this is generally unnecessary for properly tuned substrate.

Once the water-soluble polymer dissolves (ii), the Si substrate sinks to the bottom of the bath leaving the extremely hydrophobic PMMA floating on top, (iii) The PMMA membrane is adhered to a glass transfer slide, which is clamped onto the arm of a micromanipulator mounted on an optical microscope. Using the microscope to optically locate the position of the graphene flake on the suspended polymer film, the graphene is precisely aligned to the target BN and the two are brought into contact. With this technique the graphene can be positioned to within a few microns of the target position. During transfer, the target substrate is heated to 110 ^{o}C in an effort to drive off any water adsorbed on the surface of the graphene or hBN flakes as well as to promote good adhesion of the PMMA to the target substrate; (iv) Once transferred, the PMMA is dissolved in acetone. Electrical leads are deposited using standard electron beam lithography, after which all our samples are annealed in flowing H_2/Ar gas at 340 ^{o}C for 3.5 hours to remove resist residues. The devices presented in the main text did not undergo any further treatment (i.e. in-situ vacuum annealing etc.) after removal from the H_2/Ar flow.

Before transferring graphene, the surface of every target hBN flake is first characterized by atomic force microscopy to ensure it is free of contaminants or step edges, and also to measure its thickness. AFM images were acquired in air using silicon cantilevers operated in tapping mode. Fig. 3.1a-b shows optical and AFM images of a clean hBN surface after mechanical exfoliation

onto a SiO_2 substrate. While the texture of the SiO_2 surface is visibly apparent, the hBN surface looks completely devoid of any features on this scale. Fig. 3.1c shows a histogram of the measured surface roughness for hBN flakes of varying thicknesses. Measurements from a typical SiO_2 substrate, and from a calibration HOPG wafer are also shown, for comparison. All data was acquired on a 300 nm^2 scan window. The SiO_2 surface roughness , given by the standard deviation of a fitted Gaussian, is measured to be ~ 185 pm, consistent with values reported elsewhere[116]. The HOPG surface roughness is ~ 70 pm, which, since the HOPG wafer is atomically flat over large areas, is taken to be the resolution limit of our measurement. As seen in Fig. 3.1d, the hBN surface roughness approaches the measured HOPG roughness for flakes thicker than approximately 5 nm.

The hBN flakes used in this study are exfoliated from ultra-pure, hexagonal-BN single crystals, grown by the method described in Ref. [118]. The optical contrast on 285 nm SiO_2/Si substrates is sufficient to easily identify hBN flakes with thicknesses down to a single monolayer (see Fig. 3.3b as well as Ref. [17]). Fig. 3.4 shows AFM images of monolayer graphene transferred onto $\sim$14 nm thick hBN. The transferred graphene is free of wrinkles or distortions, consistent with previous reports of similar PMMA-based transfer techniques[119]. A histogram of the roughness of graphene on hBN (Fig. 3.4b) shows it to be indistinguishable from bare hBN and approximately three times less rough than SiO_2. We conclude that the graphene membrane conforms to the atomically flat hBN, consistent with previous reports on both rippled [9] and flat [116] surfaces.

3.1.2 Transport characterization of hBN supported graphene devices

Electronic transport measurements of monolayer graphene transferred onto hBN indicate that the resulting two-dimensional electronic systems are of high quality. Fig. 3.5a shows the resistance of a typical monolayer graphene sample on hBN as a function of applied back gate voltage, V_g.

The resistivity peak, corresponding to the overall charge neutrality point, is extremely narrow and occurs at nearly zero gate voltage. The conductivity (dotted line inset in Fig. 3.5a) is strongly sublinear in carrier density, indicating a crossover from scattering dominated by charge impurities at low density to short-range impurity scattering at large carrier density[101–103, 107, 120]. The data is well fit (solid line in figure) by a self-consistent Boltzmann equation for diffusive transport that includes both long and short range scattering [102, 103], $\sigma^{-1} = (ne\mu_C + \sigma_o)^{-1} + \rho_s$, where μ_C is the density-independent mobility due to charged-impurity Coulomb (long-range) scattering, ρ_S is the contribution to resistivity from short-range scattering, and σ_o is the residual conductivity at the charge neutrality point. We obtain $\mu_C \sim 60,000$ cm^2/Vs, three times larger than on SiO_2 using a similar analysis[120], and $\rho_S \sim 71\ \Omega$, which is similar to values obtained on SiO_2. This indicates a threefold decrease in the scattering rate due to charge-impurities in this sample, but a similar degree of short range scattering, in comparison to the best SiO_2 samples. This suggests that the sublinear shape does not result from increased short range scattering on BN substrates, but rather a substantially reduced charge impurity contribution, which reveals the effects of short range scattering at comparatively lower densities. Similar behavior was observed in more than 10 monolayer graphene samples and, importantly, we always measure a higher mobility for BN-supported graphene as compared to portions of the same flake on the nearby SiO_2 surface (see SI). For the monolayer graphene device shown here, the Hall mobility is $\sim$25,000 cm^2/Vs at high density, where short range scattering appears to dominate. While the origin of short-range scattering remains controversial, the similar values of ρ_S between SiO_2 and hBN supported-graphene samples suggests that scattering off ripples and out-of-plane vibrations[106, 107] may not be a significant contribution in our samples since these are likely to be suppressed on atomically flat hBN. For

comparison with literature, we note that the field effect mobility, defined by the derivative of the Drude formula; $\mu_{FE} = (1/C)d\sigma/dV_g$, varies from ∼25,000 cm^2/Vs at high density (in agreement with the Hall mobility) to as large as ∼140,000 cm^2/Vs near the charge neutrality point.

The width of the resistivity peak at the charge neutrality point gives an estimate of the charge-carrier inhomogeneity resulting from electron-hole puddle formation at low density [90]. In Fig. 3.5a the full width at half maximum (FWHM) of $\rho(V_g)$ is ∼1 V, giving an upper bound for disorder-induced carrier density fluctuation of $\delta n < 7 \times 10^{10}$ cm^{-2}, a factor of ∼3 improvement over SiO_2 -supported samples [108]. An alternate estimate of this inhomogeneity is obtained from the temperature dependence of the minimum conductivity. In Fig. 3.5c, σ_{min} increases by a factor of two between 4 K and 200 K. Such a strong temperature dependence has previously only been observed in suspended samples, with substrate-supported samples typically exhibiting $< 30\%$ variation in the same range [109]. σ_{min} is expected to vary with temperature only for $k_B T > E_{\text{puddle}}$ where for monolayer graphene[109] $E_{\text{puddle}} \approx \hbar v_f \sqrt{\pi \delta n}$. Here σ_{min} saturates to $\sim 6e^2/h$ for $T \lesssim 15$ K giving an upper bound of $\delta n \sim 10^9$ cm^{-2}. The δ_n estimated by these two measures is consistent with similar analysis performed on suspended devices[109, 121].

It has been proposed that a band gap would be induced in graphene aligned to an hBN substrate[115]. In our experiment the graphene has a random crystallographic orientation to the substrate, and thus we do not expect the necessary sublattice symmetry breaking to occur. Indeed, the temperature dependence of σ_{min} observed here does not follow the simply activated behavior that would be indicative of an energy gap. While we cannot rule out the possibility of locally gapped regions resulting from symmetry breaking over finite length scales, we see no evidence from transport measurements that an appreciable gap is present in this randomly stacked graphene on hBN.

Transport measurements from bilayer graphene transferred to hBN are shown in Fig. 3.5b. The corresponding conductivity is linear in gate voltage up to large densities, as expected for bilayer graphene in the presence of long and short range scalar potential disorder [122]. The (density-independent) electron and hole Hall mobilities are ∼60,000 cm^{-2}/Vs and ∼80,000 cm^{-2}/Vs, respectively, at T =2 K, with a value of 40,000 cm^{-2}/Vs measured at room temperature in air for this same device. The FWHM of the resistivity peak is ∼1.2 V, giving an estimate of the carrier inhomogeneity density $\delta n \sim 9 \times 10^{10}$ cm^{-2}. Both the mobility and inhomogeneity are comparable to the best reported suspended bilayer graphene devices[121] and almost an order of magnitude better than bilayer graphene on SiO_2[107]. The temperature dependence of σ_{min} (blue circles in Fig. 3.5c) is much stronger than in monolayer graphene, consistent with previous studies [107, 121] (We note that the bilayer graphene studied here, although undoped immediately after sample fabrication and annealing, was contaminated upon insertion into a helium flow cryostat; thereafter the charge neutrality point was found at $V_g \sim -27$ V. The temperature dependence at the charge neutrality point may therefore be due in part to an electric field induced energy gap[123, 124]).

The temperature dependence of the resistivity at high density for both monolayer graphene and bilayer graphene is shown in Fig. 3.5d. monolayer graphene resistance increases linearly with temperature (solid line in Fig. 3.5d) due to longitudinal acoustic phonon scattering, $\rho_{LA}(T) = \left(\frac{h}{e^2}\right) \frac{\pi^2 D_A^2 k_B T}{2h^2 \rho_s v_s^2 v_f^2}$, where $\rho_s = 7.6 \times 10^{-7}$ kg/m^{-2} is the graphene mass density, $v_f = 1 \times 10^6$ m/s is the Fermi velocity, $v_s = 2 \times 10^4$ m/s is the longitudinal acoustic phonon velocity and D_A is the acoustic deformation potential[105, 109]. Linear fits to the electron (hole) branches give $D_A \sim 18$ eV ($D_A \sim 21$ eV). In contrast, bilayer graphene exhibits a very weak temperature dependence, with a slightly negative overall trend (dashed line in Fig. 3.5d). Both of these findings agree with previous

measurements[105, 107, 109, 120]. We note that no indication of activated remote surface phonon scattering is seen in monolayer graphene (bilayer graphene) up to 200 K (240 K). However, further studies in a variable temperature UHV environment[105] are need to explore the high temperature behavior in graphene-on-BN more fully.

The chemical reactivity of our graphene–on–hBN heterostructures appears to be markedly different than graphene–on–SiO_2. Fig. 3.5e shows the room-temperature conductivity of a typical monolayer graphene layer before and after annealing in a H_2/Ar flow at 340^{o}C for 3.5 hrs (see methods). Annealing substantially enhances the carrier mobility while leaving the position of the charge neutrality point virtually unchanged. The low mobility immediately post-transfer may be due to neutral transfer residues and/or local strains that are relaxed upon heating. The lack of doping after heating in H_2/Ar is in stark contrast to SiO_2-supported devices, where heat treatment typically results in heavy doping of the graphene, often more than $5 \times 10^{12}\mathrm{cm}^{-2}$, after re-exposure to air. The mechanism responsible for this different behavior remains unclear since features of both the substrate (*e.g.* surface chemistry) and the graphene (*e.g.* roughness) may play a role.

Magnetotransport measurements provide further confirmation of the high material quality achieved in these samples. Fig. 3.6a shows the magnetoconductivity σ_{xx} and Hall conductivity σ_{xy} as a function of density at B=14 T for monolayer graphene, derived from simultaneous measurement of magnetoresistance R_{xx} and Hall resistance R_{xy} in the Hall bar geometry shown in Fig. 3.4. Complete lifting of the four-fold degeneracy[24] of the zero energy Landau level is observed, with the additional quantum hall states at $\nu = 0, +1, \pm 2$ exhibiting quantized Hall conductance $\sigma_{xy} = \nu e^2/h$ together with vanishing σ_{xx}. The dashed line in Fig. 3.6a indicates that signatures of the $\nu = \pm 1$ quantum hall effect (QHE) are visible at fields as low as $B = 8.5$ T, more than a factor

of two smaller than reported for monolayer graphene on SiO_2[24].

A complete sequence of broken symmetry Landau levels are visible in bilayer graphene at B =14 T (Fig. 3.6b). In our device, the substrate supported geometry allows us to probe much higher density than possible in suspended devices of similar quality[121]. Quantized Hall resistance is observed at $R_{xy} = \frac{1}{\nu}h/e^2$ concomitant with minima in R_{xx} for all integer filling factors from $\nu = 1$ to at least $\nu = 16$. Density sweeps at lower fields (see SI) show that the lifting of the expected four-fold degeneracy in bilayer graphene[121] is observable up to at least the fifth Landau level at less than 5 T. Complete quantization of the four-fold degenerate Landau levels and Shubnikov-de Haas oscillations is seen down to 2 and 0.4 T respectively. (Fig. 3.6b).

Fig. 3.7a shows an enlargement of the magneto-transport measured from BLG on hBN presented in Fig. 3.6. Landau levels are labeled between 5 and 14 Tesla, indicating that appearance of the four-fold symmetry breaking is visible down to approximately 5 Tesla. Complete quantization of the four-fold degenerate LL's, evidenced by both quantization in R_{xy} and a near-zero minimum in R_{xx}, is observed down to approximately 2 Tesla. The inset of Fig. 3.7a shows the low field Shubnikov de Haas oscillations, which are visible down to as low as 0.4 Tesla.

Magnetoresistance measured at fixed field and varying backgate voltage are shown for several different fields in Fig. 3.7b. Minima in between the otherwise four-fold degenerate LL's, for LL index greater than $\nu = 4$, begin to emerge at $\sim$5 Tesla, becoming fully quantized for all integer fillings up to at least $\nu = 20$ at 14 Tesla. In the lowest energy LL, where the n=0 and n=1 levels are doubly degenerate, the $\nu = 2$ quantum Hall state shows a deep broad minimum at fields well below 5 Tesla.

In the lowest Landau level the even-integer, $\nu = 2$, quantum Hall state has a larger gap compared to the odd-integer states, $\nu = 1$ and 3, as judged by the depth of the R_{xx} minimum[121, 125]. In the second Landau level, the situation is reversed, with the even integer state ($\nu = 6$) weaker than the odd integers ($\nu = 5, 7$). A full understanding of symmetry breaking with increasing Landau level index in bilayer graphene is postponed to the next chapter, where controllably applying a symmetry breaking field reveals the spin-and valley splitting of the LLs.

The technology of transferring atomically thin membranes from substrate to substrate while maintaining the integrity of the graphene and the quality of the electronic system opens up a number of experimental directions which were not possible before. Fig. 3.8 show a few of the possible geometries for both technological [15] and fundamental applications. In addition, the aligned transfer process can be easily extended to other materials amenable to mechanical exfoliation onto the polymer stack, including not only the family of graphenes but MoS_2, Niobium selenide, and cuprate superconductors of the BaSrCaCuO family.

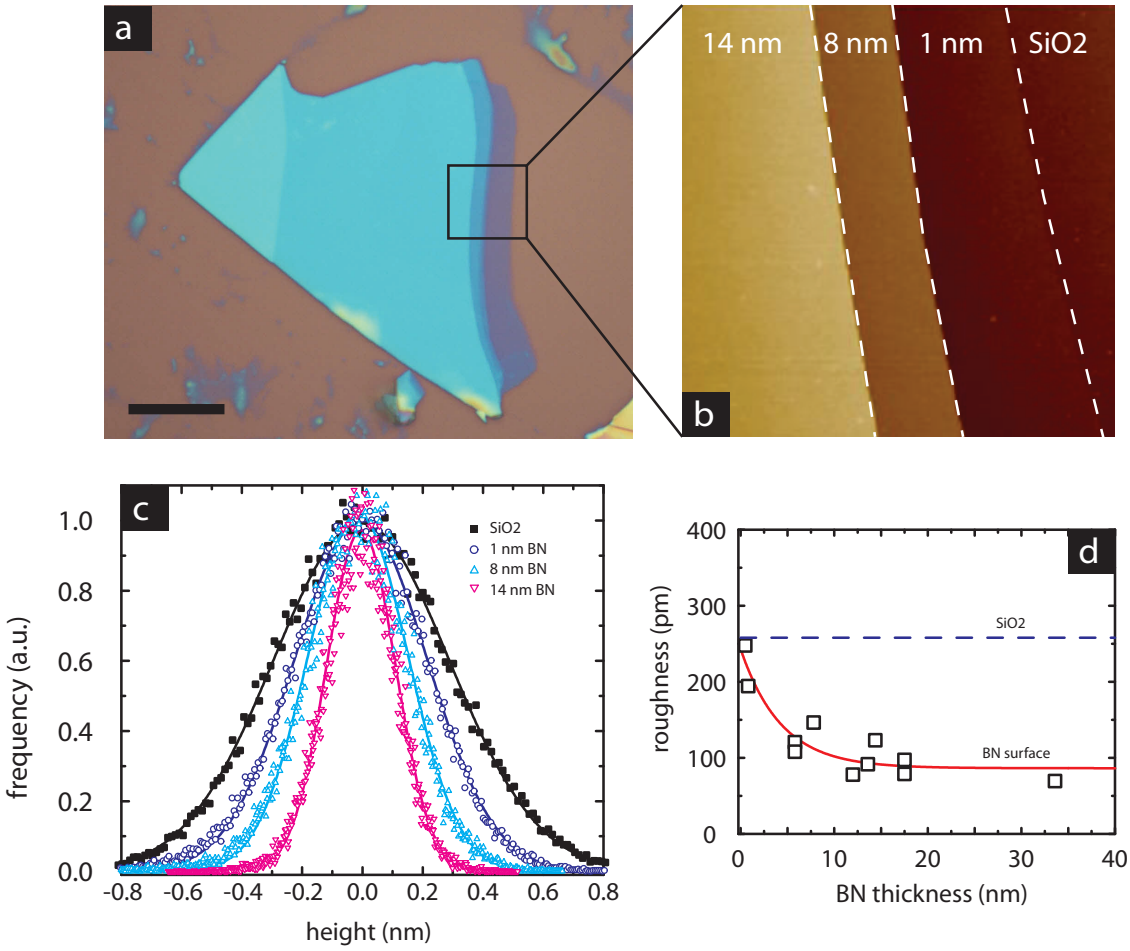

Figure 3.1: Mechanical characterization of hBN flakes
(a)Optical image of a representative hBN flake exfoliated onto a Si/SiO_2 substrate. (b) AFM image of the region indicated in (a) by a dashed box. scale-bar is 0.5 μm. The hBN surface seen here measures $\sim$ 8 nm in height relative to the SiO_2 backgraound. At this scale it is apparent the hBN surface is much smother than the underlying SiO_2 substrate. (c) Height histogram of the hBN surface measured for several different sample-thicknesses. A typical measurement from a SiO_2 surface (solid black squares) and a HOPG wafer (open black circles) are shown for comparison. (d) hBN surface roughness versus sample thickness measured from several different samples. Solid line is a guide-to-the-eye. Dashed line indicates resolution of our system, obtained by measuring the surface of HOPG under the same conditions.

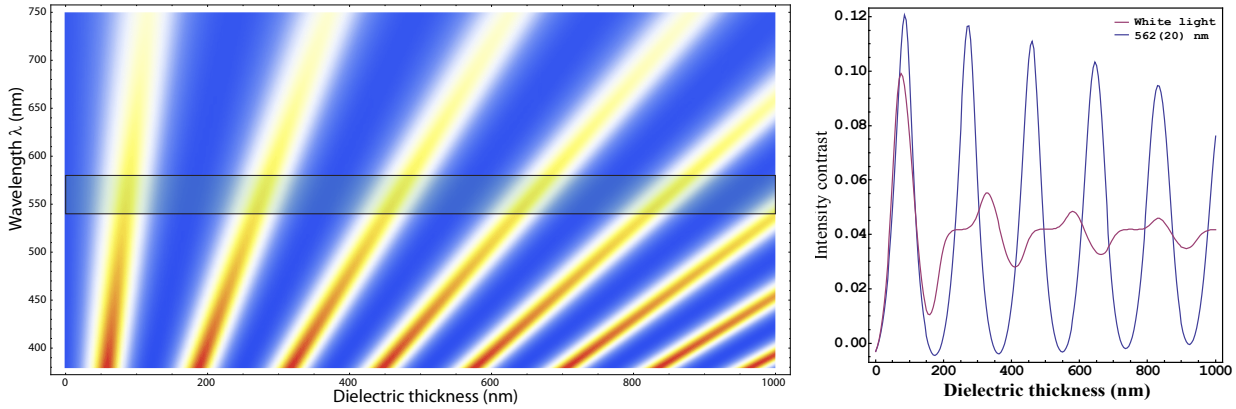

Figure 3.2: Intensity contrast calculations for polymer substrate thickness tuning
Left: Calculated optical contrast as a function of light wavelength and thickness for a dielectric substrate with index of refraction n=1.47. High contrast fringes disperse strongly for thicker substrates, resulting in diminished contrast for thicker substrates when averaging is carried out over all visible wavelengths. Restriction of the wavelengths with an optical band-pass filter restores the sharp contrast, allowing the method to be extended to high thicknesses (see right).

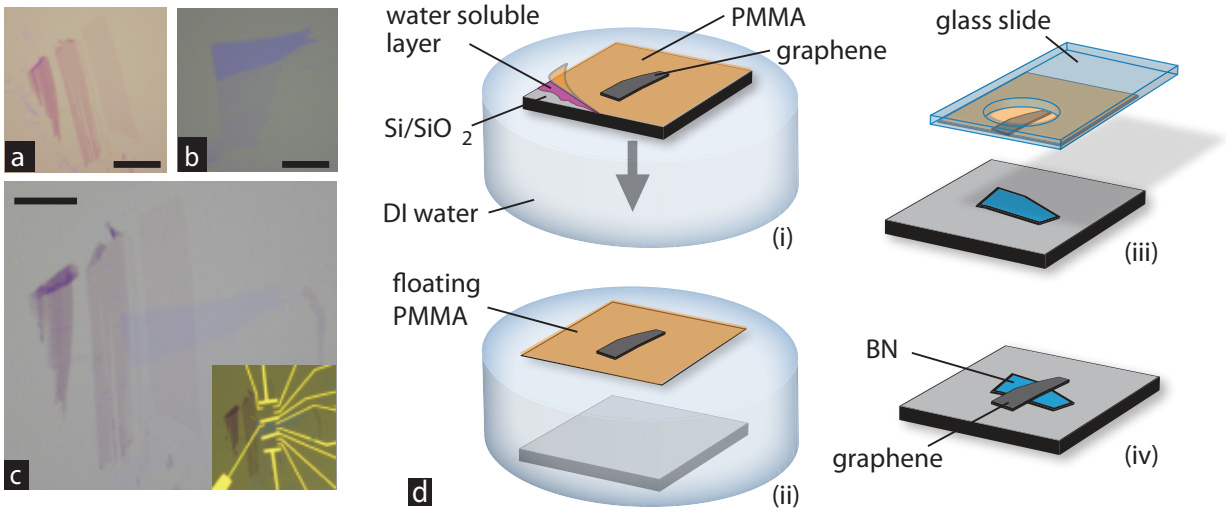

Figure 3.3: Mechanical Transfer Process.
Optical images of graphene and hBN before (a and b, respectively) and after (c) transfer. Scale bar in each is 10 μm. Inset shows electrical contacts. (d) Schematic illustration of the transfer process to fabricate graphene-on-BN devices (see text for details).

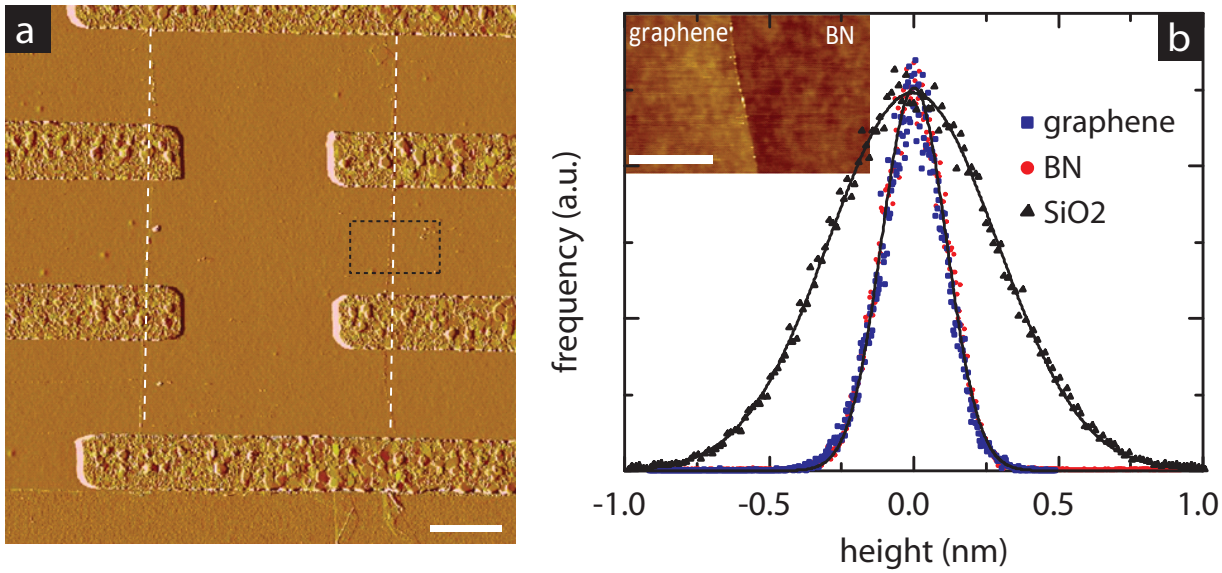

Figure 3.4: Atomic force microscopy of a graphene on hBN device
(a)AFM image of monolayer graphene on BN with electrical leads. White dashed lines indicate the edge of the graphene flake. Scale bar is 2 μm. (b) Histogram of the height distribution (surface roughness) measured by AFM for SiO_2 (black triangles), hBN (red circles) and graphene-on-BN (blue squares). Solid lines are Gaussian fits to the distribution. Inset: high resolution AFM image showing comparison of graphene and BN surfaces, corresponding to the dashed square in (a). Scale bar is 0.5 μm

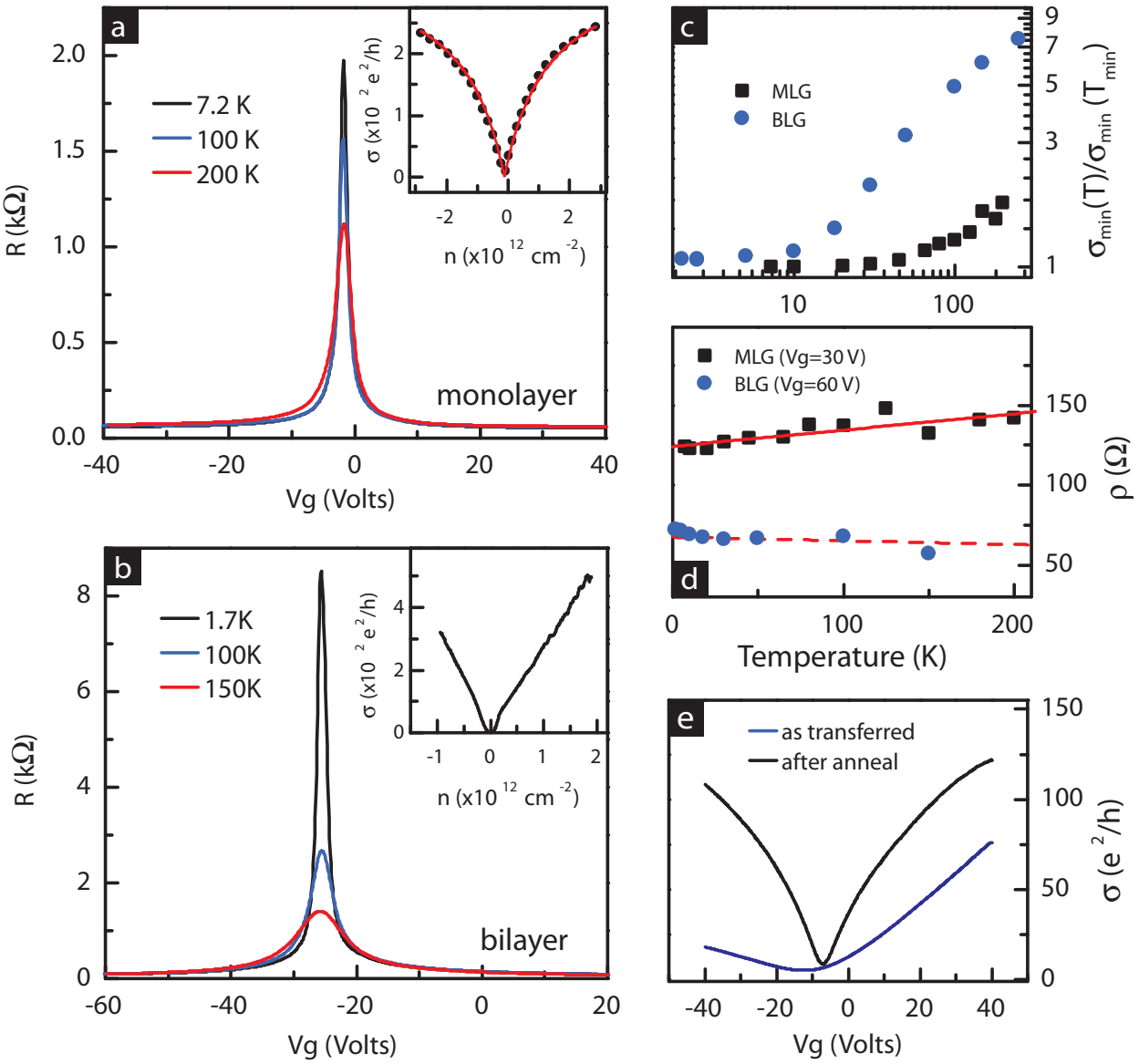

Figure 3.5: B=0 transport properties of hBN supported graphene devices
Resistance versus applied gate voltage for (a) monolayer graphene and (b) bilayer graphene on hBN. Inset in each panel shows the corresponding conductivity. For both devices, the temperature dependence of the conductivity minimum and high density resistivity are shown in (c) and (d), respectively. Solid and dashed lines in (d) are linear fits to the data. (e) Conductivity of a different monolayer graphene sample comparing the room-temperature transport characteristics measured as–transferred–to–hBN (blue curve) and after annealing in H_2Ar (black curve).

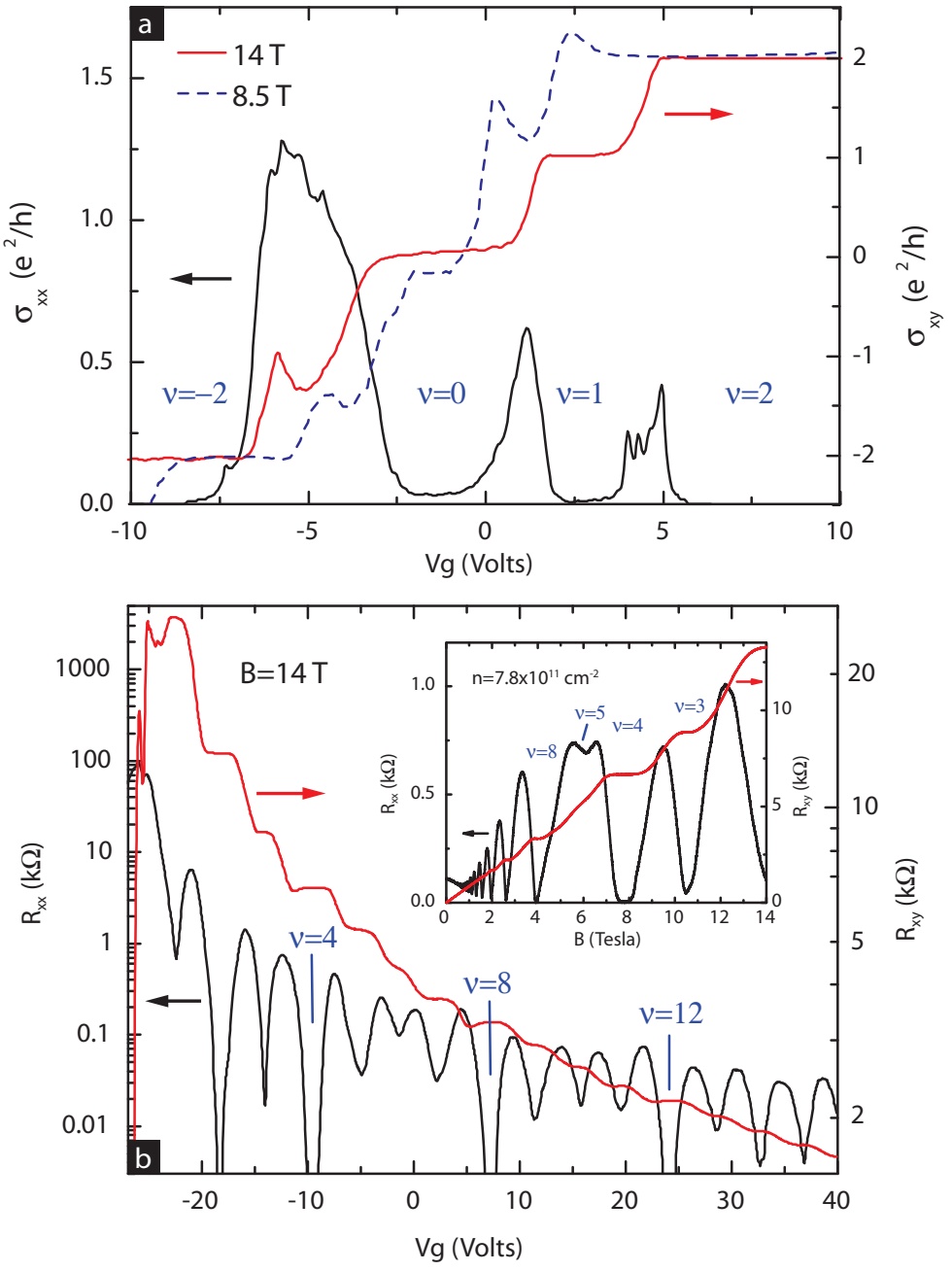

Figure 3.6: Magnetotransport of graphene on hBN devices
(a)Longitudinal and Hall conductivity versus gate voltage at $B = 14$ T (solid line) and 8.5 T (dashed line) for monolayer graphene. (b) Longitudinal and Hall resistance versus gate voltage at $B = 14$ T for bilayer graphene. Inset shows a magnetic field sweep at fixed density. SdH oscillations begin at ∼0.4 T with Landau level symmetry breaking appearing at fields less than 6 T. $T \sim 2$ K in both panels.

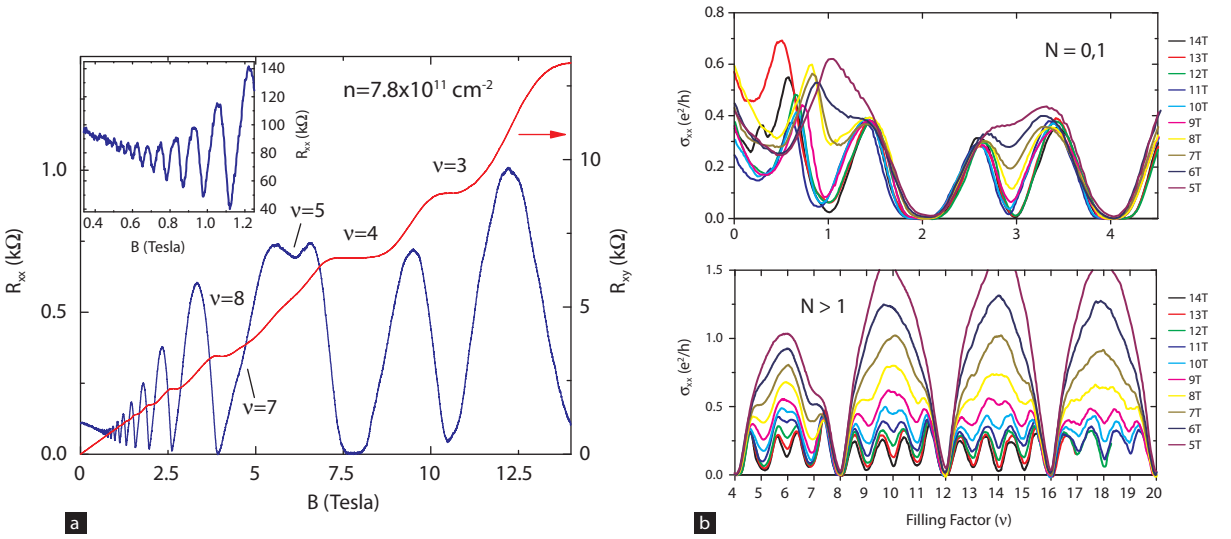

Figure 3.7: Additional magnetotransport data from a bilayer graphene on hBN sample (a)Magnetoresistance (blue curve) and Hall resistance (red curve) versus B field of the BLG sample on hBN. $T \sim 4$ K and $n = 7.8 \times 10^{11}$ cm^{-2}. Landau Levels between 5 and 14 Tesla are labeled. Inset shows low field SdH oscillations, measured under the same conditions.(b) Magnetoresistance versus gate voltage of the same sample. Upper panel shows symmetry breaking in the lowest energy Landau Level (i.e. $|\nu| < 4$). Lower panel shows symmetry breaking of the higher order Landau levels. The data is plotted versus filling factor for easier comparisons between different magnetic fields.

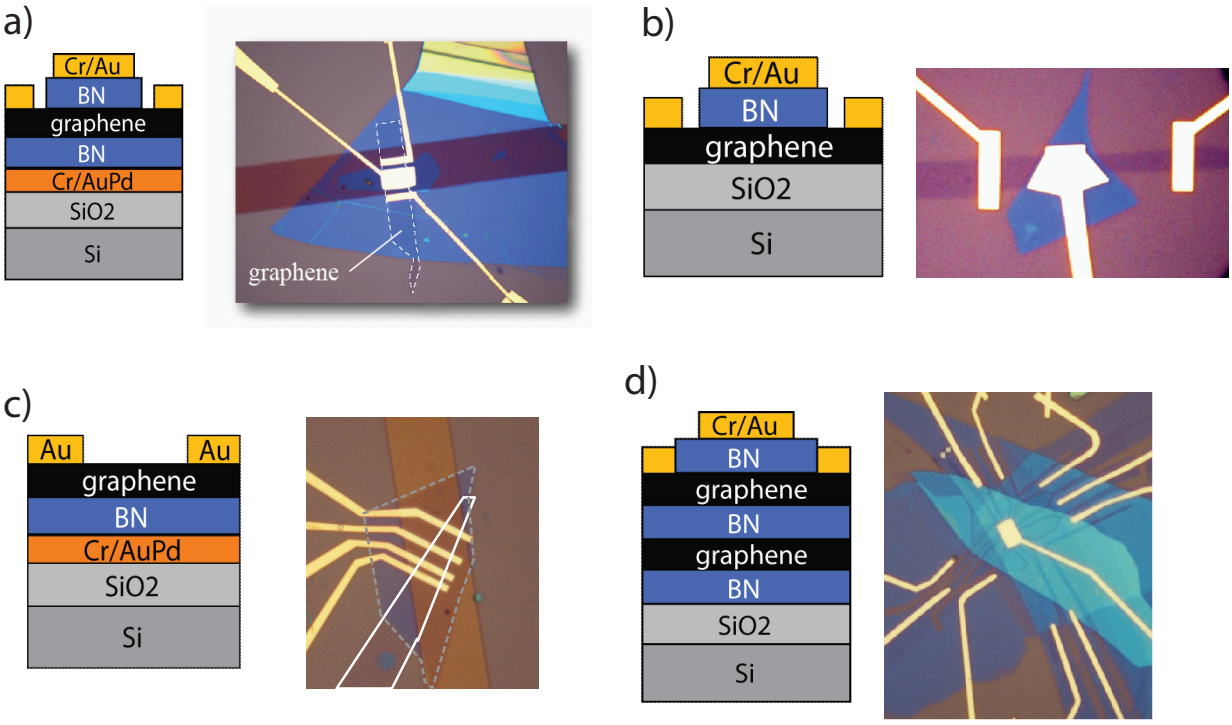

Figure 3.8: Heterostructure heaven

Sample device geometries enabled by the combination of hBN gate dielectrics and the aligned transfer process (a-b) Dual gated graphene devices for capacitance measurements. (c) Thin hBN FET structure, designed for high transconductance. (d) Dual gated, double layer graphene structure with independence contacts to the two graphene layers. Interlayer Coulomb drag and tunneling measurements are now possible between clean graphene monolayers, with the ratio d/ℓ_B tunable over a wider range than in conventional GaAs double quantum wells [126]. This will allow experimental access to the exciton phase diagram in the oppositely doped regime, an issue of ongoing theoretical debate[127, 128].

Chapter 4

Interaction driven quantum Hall effects in graphene

Electronic systems with several degenerate degrees of freedom can support a rich variety of broken symmetry states. In graphene subjected to a quantizing magnetic field, the strong Coulomb interactions and fourfold spin/valley degeneracy lead to an approximate SU(4) isospin symmetry within individual Landau levels. At partial filling, exchange interactions can drive the ground state to polarize ferromagnetically[129] within this expanded isospin space, manifesting experimentally as additional integer quantum Hall (QH) plateaus outside the normal sequence. At still higher fields, quantized Hall plateaus appear at fractional LL fillings[130], associated with the formation of a quantum liquid with topological order[131]. This chapter details a series of experiments devoted to the exploration of these interaction driven quantum Hall states in mono- and bilayer graphenes, performed on the substrate-engineered devices developed in the work presented in the previous chapter.

The first section will describe the observation of a wide number of interaction-induced integer quantum Hall states in monolayer graphene, and their classification according to their real spin structure *via* tilted field magnetotransport. Through activation gap measurements, we find evidence

for real spin polarized states supporting Skyrmionic excitations, charge- or spin- density order, and valley textured excitations at different filling factors, revealing the absence of a universally dominant anisotropy in the graphene QHIMF. In the second section, I will discuss the observation of a number of fractional QH states in monolayer graphene, and relate the hierarchy of FQH states observed to the isospin anisotropies probed in section two. The hierarchy of FQH states observed in graphene, particularly in the zero energy LL (ZLL), again reflects the unique symmetries and anisoptropies of the graphene QHFM. In the final section, I will discuss preliminary measurements on bilayer graphene.

4.1 Spin and valley quantum Hall ferromagnetism

Graphene is exceptional among multicomponent quantum Hall systems [132–134] due to a near-perfect energetic hierarchy (See Fig. 4.1). The energy scales characterizing cyclotron motion (E_N) and long range interparticle Coulomb interactions (E_C)—both of which reflect physics that is independent of spin or valley flavor—dwarf explicit spin and valley symmetry breaking effects. The combined four flavor degeneracy can therefore be thought of as a single SU(4) isospin[31, 33]. As in other multicomponent quantum Hall systems, exchange interactions can drive the system through a ferromagnetic instability[21], in which the order parameter corresponds to a finite polarization within the appropriate isospin space. At integer fillings within a partially filled quartet LL, this order parameter is leads to a finite gap for charged excitations and a robust quantum Hall effect for integers outside the usual single particle sequence. The precise SU(4) polarization for given experimental conditions depends on the interplay between anisotropies arising from the Zeeman

effect, lattice scale interactions, and disorder. All of these anisotropies are small and experimentally tunable, allowing for the possibility of a variety of distinct ground states across accessible ranges of filling factors, magnetic fields, and realizations of disorder.

Previous studies performed on SiO_2-supported or suspended graphene have indeed reported the observation of QHE at several integer filling factors outside the normal sequence[24, 27, 40, 135–137]; however, the nature of the (presumably broken symmetry) states leading to these plateaus remains a matter of intense theoretical debate[20, 21, 138–158]. In the ZLL, most experimental [136, 137, 159–162] and theoretical [20, 145–158] work has focused on the strongly insulating behavior observed at $\nu = 0$, corresponding to half filling of the zero energy Landau Level, which has no analog in conventional two dimensional electron systems. The insulating state has been described variously as a spin-polarized valley singlet, a valley polarized, spin singlet, or a lattice scale spin density wave, but experimental resolution of this discrepancy has been hampered by the absence of any probe of the spin or valley order. Even less is known about the symmetry breaking at $\nu = \pm 1$[24, 135], [20, 139, 142, 163] or throughout the $N \neq 0$ LLs[24, 27, 135, 137]. Due to the anomalous structure of the ZLL, in which the valley quantum number and real-space sublattice coincide, the symmetry broken states for $N = 0$ may not resemble those for $N \neq 0$; however, limitations on sample quality and geometry in SiO_2 supported and suspended devices, respectively, have precluded a comparative study.

We address these issues by studying the activation gaps, ${}^{\nu}\Delta$, associated with the broken symmetry IQHE states in graphene devices fabricated on hBN substrates[40]. This gap is associated with thermally exciting the lowest lying charged excitations of the ground state. Owing to the atomic-scale confinement of the electronic wavefunctions to the plane of the graphene, all orbital

effects related to electronic interactions depend only on the out of plane component of magnetic field $B_\perp$, while spins respond directly to the total magnetic field, B_T, independent of its direction. Tilted field measurements of the ${}^\nu\Delta$ thus allow us to extract quantitative information about the spin textures of the ground state and its elementary excitations.

Figure 5.8a shows the evolution of the quantum Hall effect with magnetic field in a representative device. Symmetry breaking at $\nu = \pm 1$ is visible at fields of $B_\perp \gtrsim 5\ T$, followed by the higher LLs at $B_\perp \gtrsim 7\ T$; by 14 T (overlaid), ρ_{xx} minima are visible at all integer filling within the experimental range. In addition, an insulating state develops at $\nu = 0$ (Fig. 1c) starting from 2-3 T, consistent with previous work on clean, suspended graphene [137, 161]. We find that all broken symmetry ρ_{xx} minima, as well as the $\nu = 0$ insulator, show simply activated temperature dependence over a wide range of fields (Fig 1d and inset to Fig 1c), allowing us to extract the energy gap ${}^\nu\Delta$ as a function of perpendicular and total field. Using this technique, we explicitly demonstrate the dependence of the isospin ferromagnetic order and accompanying charged excitations—for fixed relative filling factor—on LL index. Specifically, in the $N \neq 0$ LLs, a dominant Zeeman anisotropy leads to spin polarized ground states at half filling and valley textured excitations at quarter filling; in the ZLL, the situation is reversed, with a spin unpolarized insulating state observed at $\nu = 0$ and real spin textured excitations from the fully polarized $\nu = 1$.

The exceptional quality of the devices studied here allows the observation of all integer filling broken symmetry states at magnetic fields of a few tesla, allowing the Zeeman energy to be tuned across a wide range in experimentally realizable magnetic fields. The quantum scattering lifetime is a quantitative measure of sample disorder, and can be determined from the magnetic field

dependence of the Shubnikov de Haas (SdH) oscillation amplitude according to [120, 164, 165]

$$\Delta\rho = 4\rho_o\gamma_{th}e^{-\pi/\omega_C\tau_q}, \tag{4.1}$$

where $\Delta\rho$ is the resistivity amplitude of the SdH oscillation, ρ_o is the non-oscillatory background resistance, γ_{th} is a thermal factor that describes the thermal contribution to the Landau level broadening, and $\omega_c = eB/m^*$ is the cyclotron frequency where e is the electron charge, B is the magnetic field and m^* is the effective carrier mass. In graphene the analogous relation can be guessed by defining the effective mass as $m^* = E_F/v_F = \hbar\sqrt{\pi n}/v_F$. From the SdH resistivity oscillations (Fig. 4.3 b), values for $\Delta\rho$ were obtained using a similar analysis as in Ref. [120]. Fig. 4.3c shows a log plot of $\Delta\rho$ versus $1/B$ (a so-called Dingle plot) acquired from the resistivity curves shown in Fig. 4.3b. The slope of a linear fit gives the quantum lifetime, τ_q, which is then used to calculate the corresponding Dingle temperature $\Gamma = \hbar/2\tau_q$, plotted for several traces in 4.3d and yielding an average LL broadening of $\Gamma \sim 33 \pm 8$ K.

Devices were measured in a sample-in-^{4}He vapor variable temperature cryostat fitted with a mechanical sample rotation stage, mounted in the bore of a 35 T resistive magnet at the National High Magnetic Field Lab in Tallahassee, FL. Electrical measurements for $\nu \neq 0$ were performed in the four point geometry using a 10-100 nA current bias. For the $\nu = 0$ measurements were taken in the two terminal geometry using a 200 μV excitation voltage. The numerous features present in a gate voltage trace at intermediate magnetic fields ($B_\perp < 25$ T) allowed precise angle calibration, with $B_\perp$ determined to better than .5% accuracy. This was particularly important in the case of the $\nu = 0$ state, where the dependence on $B_\perp$ is at least one order of magnitude stronger than that on B_T.

R_{xx} minima were determined by sweeping the gate voltage at fixed temperature. All ρ_{xx} minima, as well as the resistance maximum at $\nu = 0$, obey an Arrhenius law, $R_{xx} \sim R_0 \exp\left(\frac{-\Delta}{2T}\right)$. Gaps were determined by fitting to this formula over at least one decade of resistance when possible. Error bars are dominated by ambiguity in picking out the appropriate 'linear regime'. Plots for all gaps presented in the main text, including best fits, are available in the appendix.

Figures 4.4a-b show activation gaps for the half-filled LLs, $\nu = 0, -4, -8, -12$, as a function of $B_\perp$. The perpendicular field dependence for all N is qualitatively similar, following an approximately linear scaling with $B_\perp$ in which the effective gyromagnetic ratio in *perpendicular* field, $g_\perp \equiv \mu_B^{-1}\partial_{B_\perp}({}^{\nu}\Delta)$, is enhanced with respect to the bare value $g_0 = 2$. The measured energy gaps are much larger than might be expected from known single-particle effects; in addition, $g_\perp$ decreases with increasing LL index N, consistent with exchange-driven gaps[21].

Tilted field measurements reveal the uniqueness of the ZLL. For $N \neq 0$, the half filled gaps, ${}^{-4}\Delta$,${}^{-8}\Delta$, and ${}^{-12}\Delta$, increase with B_T for fixed $B_\perp$(Fig. 4.4d). This is consistent with the existence of real spin polarized states, in which excitations involve quasiparticles containing a net spin reversal relative to the ground state (and applied magnetic field). The activation gaps of such excitations consist of a direct Zeeman contribution from the reversal of spins against the external field, as well as an exchange contribution arising from the spin reversal relative to adjacent (polarized) spins,

$$\Delta = \Delta_X(B_\perp) + g_0\mu_B B_T. \tag{4.2}$$

In contrast, the $\nu = 0$ resistance decreases (Fig 4.4b) with increased E_Z, an observation incompatible with the real spin polarized scenario for $\nu = 0$[147, 149, 152, 155]. Instead, the data

suggest that a spin *unpolarized* state, in which excitations contain a net spin aligned parallel (rather than antiparallel) to the applied field, underlies the insulating behavior at $\nu = 0$.

Half filling of a fourfold degenerate graphene Landau level provides an ideal testing ground for the relative strength of the spin and valley anisotropies. Because each cyclotron guiding center is doubly occupied, Pauli exclusion prevents the Landau level from fully polarizing in both spin and valley simultaneously. Ignoring symmetry breaking terms, the ground state of a graphene quantum Hall ferromagnet at half filling, $\nu = 0, \pm 4, \pm 8, \pm 12...$, is degenerate, consisting of the family of fully SU(4) polarized two particle states; the system chooses one such state, spontaneously breaking the SU(4) symmetry. In physical graphene, a variety of symmetry breaking terms compete, explicitly destroying the SU(4) symmetry and lifting the degeneracy. The resulting ground state thus reflects the result of that competition. Early theoretical studies of the $\nu = 0$ ground state focused on the the scenario of a dominant Zeeman effect[147, 149], which leads to counterpropagating spin-polarized states at the sample boundaries and a two terminal conductance of $2\frac{e^2}{h}$. The subsequent observation of a strongly insulating high magnetic field ground state[136] cast doubt on the physicality of this scenario. While attempts have been made to reconcile spin polarization with the observed behavior ([155, 166], a more compelling explanation has since emerged stemming from the effect of the graphene lattice structure on electronic interactions[20]. The interactions of graphene electrons over long distances are well described by the continuum massless Dirac equation; however, at short distances this theory breaks down and interactions become sensitive to lattice-scale effects. In N=0 LL, where the valley quantum number coincides with sublattice, these effects can favor ground states different from the spin-polarized ferromagnet (see Fig 2 f) [20, 153, 154, 157]. Naively, the outcome of the competition between these multiple

interaction anisotropies and the Zeeman effect is not easy to assess, but both numerical[153] and renormalization group[158, 167] studies suggest that these effects are in fact likely to be dominant at realistic magnetic fields. Previous experimental studies of the $\nu = 0$ state on substrate supported [136, 159, 160, 162] and suspnended[137, 161] devices have given inconsistent results, and so far have been unable to address this puzzle.

The fact implied by Fig. 5.8a, b, d, and e is that different order prevails at half filling for $N = 0$ and $N \neq 0$ even under identical experimental conditions ($B_\perp$ and B_T, which together fix the real spin anisotropy), and suggests that the difference is in the valley sector and is intrinsic to graphene, in line with the predictions of Alicea and Fisher[20]. The experimental data indicate that while the Zeeman effect wins the competition for the $N \neq 0$ LLs, leading to spin polarized states at $\nu = -12, -8$, and -4, the short range anisotropies dominate the zero LL, leading to the formation of one of the possible lattice scale density waves portrayed in Fig. 4.4c (ii), (iii), and (iv). An additional notable feature of the experimental data is the dependence of ${}^0\Delta$ on $B_\perp$. The absence of a spin-polarized ground state at $\nu = 0$ precludes linear-in-B_T Zeeman contributions to the excitation energy. In contrast to 2D electronic systems with parabolic dispersion, in monolayer graphene both E_C and the cyclotron gaps scale as $\sqrt{B_\perp}$, a fact reflected in all available theories of the $\nu = 0$ insulator based on the linear Dirac model. The observed linear scaling thus points to the relevance of physics beyond the low energy theory.

Motivating future work, quantitative data on the decrease of the gap in applied parallel field suggest that the spin ferromagnet, which is predicted [147, 149] to be an exact analog of the spin quantum Hall state[168], may be experimentally accessible in the best samples at high tilt angles in realistic accessible magnetic fields. The response of the $\nu = 0$ insulator to magnetic field is very

weak. Thermal activation measurements of ${}^0\Delta$ in tilted field are rendered difficult by the fact that large tilt angles are required, where small miscalibrations and temperature dependent shifts of our mechanical rotator are exacerbated. Nevertheless, an *estimate* of the field required to induce the quantum spin Hall state based on less than a decade of resistance suggests it is within the reach of the largest magnetic fields with devices of typical quality, and perhaps within range of typical 15T laboratory magnetic fields with devices of only marginally higher quality (Fig. 4.5).

Despite the role of the single-particle Zeeman effect in setting the order in the higher LLs, tilted field activation gaps demonstrate that the symmetry breaking can be thought of as being essentially spontaneous, with Zeeman functioning as a small aligning field. The gaps at half filling for $N \neq 0$ increase with total magnetic field (Fig. 4.4d) faster than might be expected for single spin flips, as reflected by the enhanced measured values of $g_{\|} \equiv \mu_B^{-1}\partial_{B_T}\Delta$ (Fig. 4.4d, inset). In a Zeeman-dominated spin polarized state, charge transport occurs through the thermal activation of spin-reversed particle-hole pairs (Eq. 4.2). While exchange contributions to the energy gap lead to $g_{\perp} > g_0$ [169], this enhancement does not carry through to $g_{\|}$: changing B_T with $B_{\perp}$ fixed results in a measurement of the net spin of the excitation, and thus $g_{\|} = g_0$. In contrast, in exchange dominated spin polarized states it can be more energetically favorable to flip multiple spins smoothly in a Skyrmionic spin texture [170, 171], leading to a modified gap equation

$$\Delta = \Delta_X(B_{\perp}, E_Z/E_C) + (2K+1)g_0\mu_B B_T \tag{4.3}$$

where $K \geq 0$ represents the additional flipped spins per charged excitation and depends on the ratio E_Z/E_C. The $g_{\|}$ enhancements observed at ν=-4 and ν=-8 suggest that Skyrmions contribute to transport in both the $N = 1$ and $N = 2$ LLs. This is in contrast to quantum wells with a

parabolic dispersion where Skyrmions are thought to exist only in the N=0 LL[138, 172].

The dependence of $g_{\|}$ on LL index—as with $g_{\perp}$, $g_{\|}$ decreases with the decreasing exchange energy as Landau level index increases—agrees with theoretical expectations, but several quantitative aspects of data are not explained by a disorder free model of Skyrmion transport. In order to address the role of disorder in Skyrmion transport experimentally, we have studied the activation gaps at ν=-4 in several samples, and at several values of $B_{\perp}$. We have supplemented the natural variation in sample disorder with quasi-controlled 'contamination events', in which the disorder is increased *in situ*. Under normal conditions, graphene on h-BN samples are stable, and activation gaps can be measured repeatedly in the same sample over multiple cooldowns separated by weeks or months. However, rapidly warming the sample chamber causes outgassing from the cryostat walls, leading to the adsorption of debris on the graphene surface and higher disorder. This process, while difficult to control and not reliably reversible, allows us to exclude device-specific effects stemming, for example, from the interplay between the graphene electrons and the staggered lattice scale potential generated by the h-BN substrate (Samples before and after a contamination event are noted by numbers in parentheses). Figure 4.6a shows tilted field dependence of the activation gap ${}^{-4}\Delta$ at $B_{\perp} = 15$ T for several samples. Higher disorder is correlated with a shrinking of all LL gaps, consistent the level broadening, but also leads to a smaller measured $g_{\|}$. For the most disordered samples measured here, as well as previous measurements of graphene on SiO_2, $g_{\|} \approx 2$. As $g_{\|}$ is related to the physical Skyrmion size, this suggests that Skyrmion size may be limited principally by disorder rather than the Zeeman effect[173].

In the simplest picture of real spin Skyrmions in QHFMs, Skyrmion size is entirely determined by—and negatively correlated with—the ratio E_Z/E_C. For fixed ℓ_B, our data show some decrease

in $g_{\|}$ as E_Z is increased (4.6b), but this dependence is weaker than expected for a clean system. The ratio E_Z/E_C can also be varied by altering $B_\perp$, taking advantage of the differing scaling of the Zeeman ($E_Z \sim B_\perp$) and Coulomb ($E_C \sim \sqrt{B_\perp}$) energies. Surprisingly, we find *larger* $g_{\|}$ values for larger values of $B_\perp$ (Fig. 4.6b). A tentative explanation obtains from again considering the behavior of disorder limited Skyrmions. The shorter magnetic length at higher values of $B_\perp$ decreases the Skyrmion radius, $r_{sky} \sim (2K+1)\ell_B \propto 1/\sqrt{B_\perp}$ in absolute terms. In an inhomogenous potential Skyrmions may gain energy by shrinking so as to sit farther down in deep potential wells[173]; the 'disorder-optimized' Skyrmion radius, then, is expected to be positively correlated with $B_\perp$. We thus ascribe the observed $B_\perp$, B_T, and disorder dependences at least partially to the interplay between exchange interactions and disorder.

Like half filling, the phenomenology of a quarter filled graphene Landau level also shows markedly different behavior for $N = 0$ and $N \neq 0$. At quarter filling the naive ground state is a fully polarized state in which a single spin-valley flavor is occupied. While spin is always polarized in the direction of the field, valley anisotropies are thought to lead to Ising or x-y type valley polarizations for $N = 0$ and $N \neq 0$, respectively[139, 142]. Unlike at half-filling, spin and valley anisotropies do not compete with each other in the formation of the ground state at quarter filling: for a singly occupied cyclotron guiding center, there is no Pauli exclusion restriction on simultaneous spin- and valley polarization. The interplay between spin- and valley- anisotropies does, however, contribute to the energetic of the excitation spectrum relevant for charge transport. In the case of a dominant Zeeman effect, for example, the low lying charged excitations are thought to consist of valley flip textures [138] due to the high relative energetic cost of flipping real spins against the physical field. Most (although not all) activation measurements taken at quarter filling

for $N \neq 0$ (Figure 4.7b and c) are consistent with this scenario, with the gaps independent of B_T for fixed $B_\perp$ to within experimental error. In contrast, gaps at ν=-1 increase with increasing E_Z (Fig. 4.7a), suggesting again that the Zeeman effect is not the dominant anisotropy in the zero energy LL. Tilted field dependence of the gaps at ν=-1 also show enhancement of $g_\parallel$ over the bare value, consistent with the large strength of exchange in the zero LL[138].

While most data taken at half and quarter filling fit into the picture of QHFM with LL index dependent anisotropy, we have observed several unexpected tilted field anomalies at both odd and even filling in the high LLs. For example, among samples for which $^{-3}\Delta$ was measured as a function of E_Z, one (#129 (1)) shows reentrant behavior, with the gap collapsing with increasing Zeeman and then growing again as E_Z is further increased. Qualitatively similar behavior involving gap collapse in parallel field was observed in other samples throughout the quarter filled $N \neq 0$ LLs, (see Fig 4.8b). This behavior disappeared upon contamination of the sample with adsorbates, and the sample dependence makes it unlikely to be an intrinsic property of clean graphene. Reentrant behavior was also observed at half filling in the higher LLs at low values of $B_\perp$ in one particularly high mobility sample (see Fig. 4.8b). As has been pointed out theoretically, odd filling factors in the graphene QHFM are particularly sensitive to disorder[139, 163], which can stabilize spatially inhomogenous ground states; however, the nature of the reentrant transitions observed here remains a mystery.

The picture that emerges from the experimental data on the broken-symmetry integer quantum Hall effects is one of exchange driven quantum Hall ferromagnetism within the combined spin-valley isopsin space[21], where the leading anistropies are strongly dependent on LL index. Several questions remain, however: first, the precise nature of the ν=0 state remains elusive, and the linear

$B_\perp$ dependence is unaccounted for theoretically. Moreover, the absence of spin polarization at ν=0 and the presence of spin-reversed excitations at ν=1, need to be reconciled with the prevailing theoretical models of the FQHE in graphene ZLL [174, 175], all of which neglect the role of the valley anisotropies. This last point will be further addressed in the next section. Finally, little is understood about the structure and excitation spectrum of the odd filling states, and in particular the anomalous tilted field dependence observed in certain samples. We expect that the preliminary results presented here should motivate future work combining transport and surface science techniques, such as controlled absorbtion and scanned probe microscopy, to both elucidate the properties of the graphene quantum Hall ferromagnet and, more generally, to use the graphene QHFM as a model material platform for the systematic study of interacting disordered systems in which all relevant experimental parameters can be tuned and probed *in situ*.

4.2 Fractional quantum Hall effect

Since the first experimental report of fractionally quantized Hall conductance in a GaAs quantum well[23], the FQHE has been observed in a steadily increasing number of clean two dimensional electron systems[176–179]. The study of the FQHE in graphene is still in its infancy; however, several basic features of graphene suggest that it will differ in potentially interesting ways from the effect in other systems. First, the so-called Haldane pseudopotentials[180], which parameterize the nature of electronic interactions within a LL, differ from conventional systems due to the spinnor structure of the Hamiltonian in both monolayer and bilayer graphene. Altering the pseudopotentials alters the phase diagram of the interacting electron system, potentially leading to new phases; in bilayer graphene, these pseudopotentials are gate tunable over a wide range[181], potentially

enabling the observation of gate tunable phase transition between interaction driven phases. Second, the high degree of four-component symmetry of the graphene LL, and the exotic anisotropies discussed above, have been conjectured to produce new incompressible ground states in graphene [21, 138, 174, 182–188], some of which have no analog in conventional systems. Finally, graphene represents the first high quality two dimensional electron system in which the surface is accessible, enabling surface probes and in situ modification of the disorder potential. This last feature may allow truly new understandings of the microscopic physics of the fractional quantum Hall effect.

This section focuses on multiterminal measurements of the FQHE in high mobility monolayer graphene devices fabricated on hBN substrates [40]. The measured energy gaps are large, particularly in the second Landau level where they measure up to 10 times larger than those reported in the cleanest conventional systems. This can be understood as a consequence of the uniquely strong Coulomb interactions in graphene. These in turn are a consequence of the low atomic number of carbon and the inherently two dimensional nature of grpahene, which obviates the need to embed the two dimensional electron system in a high-κ dielectric bulk. The biggest question raised by the experiments, which is by no means resolved as of the writing of this thesis, is the role of the approximate SU(4) isospin symmetry and the unique valley anisotropies, in the fractional quantum Hall effect. While the experimental data presented show what we take to be clear signs that the spin-valley symmetry is relevant, the relationship between the quantum Hall isospin ferromagnetic states and the neighboring FQHE states remains unclear.

The measurements described are taken from a single-layer graphene sample fabricated on a hBN substrate. Fig. 1a shows the zero-field resistance and corresponding conductivity, acquired

at T$\sim$300 mK. The Hall mobility at high density is $\sim$30,000 cm^2/Vs; the charged-impurity mobility, which dominates at low density, is in excess of 100,000 cm^2/Vs as determined by fitting straight lines to the linear portion of the conductivity; the charge inhomogeneity, estimated from the resistivity peak width at the charge neutrality point (CNP), is of order 10^{10} cm^{-2}. All three metrics indicate this sample to be of exceptionally high quality and are consistent with previous measurements of similar graphene/h-BN devices [40].

Longitudinal (R_{xx}) and Hall (R_{xy}) magnetoresistance measurements acquired by varying the gate voltage at a fixed B field of 35 T are shown in Fig. 5.8c. Quantized Hall plateaus and magnetoresistance zeroes appear at all accessible integer fillings in both the $n = 0$ and $n = 1$ LLs. Signatures of symmetry-breaking appear in the Shubnikov-de Haas (SdH) oscillations at fields as low as 1 T (inset of Fig. 5.8c), with full breaking of the four-fold degeneracy observed at fields less than 5 Tesla. The most remarkable feature of this sample is the appearance of the FQHE at 35 T throughout the accessible density range (labeled with arrows in Fig. 5.8c).

In Fig. 5.10a,b detailed plots of the $n = 0$ and $n = 1$ LLs are given. For clarity, the Hall conductivity, calculated from the tensor relation $\sigma_{xy} = R_{xy}/(R_{xy}^2 + (w/l)R_{xx}^2)$, is shown where w/l is the aspect ratio of the Hall bar. We observe the hallmark features of the FQHE, namely quantization of R_{xy} to values of $\frac{1}{\nu}h/e^2$ concomitant with minima in R_{xx}, at fractional filling factors ν=$\frac{1}{3}$, $\frac{2}{3}$ and $\frac{4}{3}$ in the $n = 0$ LL and at $\nu = \frac{7}{3}$, $\frac{8}{3}$, $\frac{10}{3}$, $\frac{11}{3}$ and $\frac{13}{3}$ in the $n = 1$ LL. Additionally, a weak minimum in R_{xx} at $\nu = \frac{8}{5}$ is suggestive of an emerging FQHE state at this filling. With the exception of the $\frac{1}{3}$, $\frac{2}{3}$ and $\frac{7}{3}$, all observed Hall conductivity plateaus are within 1% of their expected value. At $\frac{1}{3}$ and $\frac{2}{3}$, the Hall plateaus are "N" shaped and do not exhibit exact quantization, typical of FQH states not yet fully formed in magnetic field.

The weak formation of the $\frac{1}{3}$ and $\frac{2}{3}$ states may be related to the presence of a competing, insulating phase at low density [136]. Fig. 4.11a shows the magnetoresistance over a wide range of densities, all plotted on the same vertical scale. Near the charge neutrality point, the proximity to the insulating phase [136] enhances the measured longitudinal bulk resistance, R_{xx}, obscuring the FQHE at low densities. The Hall conductivity, σ_{xy}, at $\frac{1}{3}$ and $\frac{2}{3}$ fillings shows $\sim \%10$ and $\sim \%3$ disagreement with the expected values, respectively. In both cases the σ_{xy} value is larger than expected (indicated as a horizontal bar in the figure), which we ascribe to mixing between the Hall and longitudinal resistivities. The 1/3 and 2/3 magnetoresistance minima are both non-zero, and they do not show activated behavior over the temperature range studied ($\sim$0.3 K to $\sim$10 K), likely due, at least in part, to a competition or coexistence with the insulating phase. The correct labeling of each plateau, in spite of inexact Hall quantization, is supported by good agreement of the density position of the magnetoresistance minima with the expected value for the corresponding FQH state (top axis of Fig. 4.11b), as well as previous observation of the two states in suspended samples [137, 161].

The gap energies of the FQHE states were measured from the temperature dependence of the R_{xx} minima in the thermally activated regime; $R_{xx} \propto e^{\Delta/2k_BT}$, where Δ is the energy gap, k_B is Boltzmann's constant and T is the electron temperature (Fig. 3). For all observed FQH states, the gaps are large in spite of considerable LL broadening due to disorder. For example, the measured gap at $\nu = \frac{4}{3}$ is 16 K at 35 T. The large gaps likely result from the lower dielectric screening and near-zero width of the 2DES in comparison to conventional semiconductor heterostructures, both of which increase the effective strength of the electron interactions that give rise to the FQHE.

Interestingly, the even numerator and odd numerator states exhibit opposite trends, with the even-numerator decreasing with increasing LL index while the odd-numerator states actually grow in strength. Although the proximity of the $\frac{1}{3}$ state to the insulating state does not allow us to measure $\Delta_{1/3}$, recent measurements performed on multi-terminal suspended graphene indicate that $\Delta_{1/3}$ is indeed larger than any gap values measured in this device [189]. The trend in the gap scaling with filling fraction may be a consequence of the relativistic dispersion relation, which modifies the electron interactions in graphene [140, 183]. In the context of the composite Fermion theory, the fact that the even numerator gaps are greater than that of the odd numerator is analogous to the broken symmetry IQHE of real electrons, where the even integer states emerge from the otherwise four-fold degenerate LLs with stronger gaps than the odd-integer states [24].

Measurement of the even-numerator gaps over a range of perpendicular fields is shown in Fig. 3d. In the simplest picture of spinless, non-interacting composite Fermions, the FQHE energy gaps are set by the Coulomb interaction between real electrons and therefore exhibit a $\sqrt{B}$ dependence with magnetic field. However, the near degeneracy of the real spin can give rise to spin-textured charged excitations, resulting in a nearly linear dependence of the FQHE gaps on magnetic field [190]. A question of fundamental interest is whether incompressible states at fractional filling in graphene support spin textured excitations, and how these relate to the underlying symmetry of the ground state. The solid and dashed lines in Fig. 3d are attempts to fit the data using square root and linear B-dependence, respectively. Both fit the data equally well, making it impossible to distinguish them at present. We use the y-axis intercepts of the two fits to estimate the disorder induced LL broadening to be in the range $\Gamma \sim$ 10–30 K, giving an estimate for the intrinsic $\frac{4}{3}$ gap at 35 T of 30–50 K, or 0.05–0.07 $e^2/\varepsilon l_B$ in Coulomb energy units. Here we have

taken the effective dielectric constant for graphene to be $\varepsilon \sim 5$, calculated from the internal electron screening due to interband transitions[100], where the external dielectric environment is taken as an average of vacuum ($\varepsilon_{vac} = 1$) and the underlying BN substrate ($\varepsilon_{BN} \sim 3.5$).

In the $n = 1$ LL, the disorder limited $\frac{8}{3}$ gap measures approximately 6 K. This is more than an order of magnitude larger gap than measured at the same total filling in GaAs devices [191] where mobilities are in excess of 10^7 cm^2/V sec, and remains 2–3 times larger even after accounting for the higher magnetic field at which our device was measured. This is consistent with the theoretical expectation that electron-electron interactions in the $n = 1$ LL of graphene are expected to be similar in strength to the $n = 0$ LL in GaAs[182].

No FQHE state appears in our samples at $\nu = \frac{5}{3}$. Due to the Berry phase shift in graphene, the lowest LL for electrons (holes) begins at filling factor ν=-2 (+2), in contrast to conventional zero-Berry phase materials, such as GaAs, in which the lowest LL begins at filling fraction $\nu = 0$. Filling factor $\pm\frac{5}{3} = \pm 2 \mp \frac{1}{3}$ is thus expected to be the closest analog to the $\frac{1}{3}$ state in conventional systems, making the non-observation of the $\frac{5}{3}$ state conspicuous given that the $\frac{1}{3}$ Laughlin state in conventional systems is generally robust. Comparing our data to theoretical understandings of the graphene FQHE, a fully spin and valley polarized ground state with low-lying valley Skyrmion excitations is theoretically expected at $\nu = \frac{5}{3}$ [138, 182, 183, 186, 187]. Calculations for a corresponding valley Skyrmion gap (0.03-0.043 $e^2/\varepsilon l_B$[182, 188]) are comparable to the $\sim$0.02–0.04 $e^2/\varepsilon l_B$ LL broadening estimated from our measurement of the $\frac{4}{3}$ gap, possibly explaining our non-observation of the $\frac{5}{3}$. At even numerator filling in the lowest LL, such as at $\frac{8}{5}$ and $\frac{4}{3}$, a valley-unpolarized ground state is theoretically predicted[182, 183, 186, 188], with larger-energy excitations than those occurring at $\frac{5}{3}$, qualitatively consistent with our experimental findings. The

mystery of the graphene FQHE data presented here is then not the absence of the $5/3$, but rather the strength of the FQHE gaps near charge neutrality.

A distinguishing feature of graphene is the fourfold internal degeneracy and in the presence of a large magnetic field we may consider three scenarios based on the single particle symmetry breaking effects: (i) all degeneracies are lifted by coupling to external fields and FQHE states cannot mix spin/valley branches; (ii) only one degeneracy, either spin or valley, is fully lifted, preserving an SU(2) symmetry in the remaining degenerate space and allowing, e.g., mixed pseudospin but not mixed spin FQH states; or (iii) both Zeeman and Valley splitting terms are sufficiently small that Coulomb interactions mix all branches, allowing mixed spin/valley FQHE states and excitations. In these scenarios, any remaining degeneracy should be reflected in the particle-hole symmetry of the FQHE states; in particular, we expect particle-hole conjugate FQH states within a single LL to have similar spin textures and gaps in the absence of any second order effects such as LL mixing[192]. The appearance of the $\frac{1}{3}$, $\frac{2}{3}$, and $\frac{4}{3}$ together with the absence of the $\frac{5}{3}$ is inconsistent with both scenarios (i) and (ii), which require simultaneous observation of either $\frac{4}{3}$ and $\frac{5}{3}$, or $\frac{1}{3}$ and $\frac{5}{3}$, respectively (Fig. 5.10d). The smallness of the Zeeman energy in comparison with Coulomb theoretically allows for the possibility [174] of real spin reversed excitations at $\nu = \frac{1}{3}$, and may account for the relative strength of the observed $\frac{1}{3}$ in comparison with the absent $\frac{5}{3}$.

An alternative scenario is based on a more subtle understanding of the nature of the valley anisotropies in the ZLL. The valley anisotropies arise from electronic *interactions*; as a result, they are fundamentally density dependent. At $\nu = 5/3$, the ZLL is barely occupied, electrons have a lot of space, and the short range interactions—which arise from from multiple occupancy of cyclotron guiding centers—should be negligible. At $\nu = 1/3$ on the other hand, each guiding

center is (almost) double occupied. The valley anisotropies should therefore be (almost) as strong as at $\nu = 0$, where, as shown in the previous section, they are at least one order of magnitude more important than the Zeeman effect, and lead to the formation of a spin unpolarized insulating state. A major outstanding experimental question is whether the isospin order of the fractional quantum Hall states near $\nu = 0$ resembles the density wave at charge neutrality, or if in fact the fractional and density wave order do indeed 'compete.' The absence of the $5/3$ state can actually be understood in either scenario: if in fact the 1/3 state is the particle hole conjugate of the $5/3$ state, it is still possible to observe different gaps, due to the increased cost (due to the short range interactions) of valley flip type excitations. If, of course, the $1/3$ state has a different isospin order, then of course no symmetry can be expected. One interpretation of the apparent 'competition' between FQHE and the insulating state ([137] and figure 4.11) is that the $1/3$ and $\nu = 0$ states do indeed have different orbital order, and the confused transport phenomenology is due to phase coexistence. As of this writing, no direct measurements of the isospin order exist. Several experimental methods may shed light on this puzzle by measuring the real spin order, starting from tilted field magnetotransport in the FQHE regime but extending to resistively detected ^{13}C nuclear magnetic resonance[193], or capacitive magnetization measurements[194].

The second LL (SLL) shows nearly all multiples of $\frac{1}{3}$ within the experimental range. For example, the $\frac{7}{3} = 2 + \frac{1}{3}$ state, the SLL analogue of the $\frac{5}{3}$, is present, and the $\frac{11}{3} = 2 + \frac{5}{3}$ and $\frac{10}{3} = 2 + \frac{4}{3}$, analogues of the $\frac{1}{3}$ and $\frac{2}{3}$ are also both well developed. Observation of the FQHE at $\nu = \frac{13}{3}$ represents, to our knowledge, the first clear measurement of the FQHE at a filling factor $\nu > 4$. This may be attributed at least in part to the fact that the FQHE states between $4 < \nu < 6$ continue to belong to the $n = 1$ LL due to the four-fold symmetry of single-particle

LLs in graphene.

4.3 Bilayer graphene

The study of electronic interactions in bilayer graphene is rapidly proving to be an even more fertile area than its analog in the monolayer. In the monolayer, as is apparent above, it is difficult to either control or probe the valley symmetry breaking. The single particle field that couples to a sublattice polarization, for example, would correspond to an electric potential commensurate with the lattice; it is difficult to imagine engineering this experimentally. In bilayer graphene, on the other hand, the relevant sublattices are on different layers. This permits the tuning—and probing, as discussed in the last chapter of the thesis—of the valley degree of freedom in bilayer graphene through the application of an out of plane electric field. The bilayer graphene QHIFM is thus an attractive alternative system in which to explore the physics discussed in this chapter, with the advantage that the valley structure can be accessed more easily experimentally.

Fig. 4.13 shows the tunable LL splitting induced by a an electrostatic gate. Producing gate-hBN-BLG-hBN-gate heterostructures while maintaining high sample quality has not been satisfactorily realized as of the writing the writing of this thesis (although no major technical obstacles remain). However, fabrication trouble can in this case be compensated by a sufficiently large magnet. In the single gated devices which are presented below, one does not have the ability to control the electric field induced splitting and density independently; however, the electric field of the single gate still induces a splitting in the LLs which can be measured.

Ignoring many-body effects, the $N \geq 2$ LLs consist of a quartet system in which the sublattice splitting is roughly proportional to the applied electronic displacement, $\Delta_{\vec{D}} \propto \vec{D}$. Each valley is

also split by its real spin projection along the direction of the magnetic field, $\Delta_\sigma = g\mu_B B_T$. In Fig. 4.13, we use intra-Landau level coincidence to measure the valley splitting, taking advantage of the isolated dependence of the spin splitting on the in-plane magnetic field. At fixed $B_\perp$—and consequently fixed gate voltages and so constant $\overline{D}$—the high energy spin branch of the low energy valley will coincide with the the low energy spin branch of the high energy valley when the spin and valley splitting coincide (Fig. 4.13c. Absent interactions, the intra-LL IQHE gaps should dissappear at this point; of course, exchange interactions can gap this now double degenerate system, leading to small residual gap. In either case, by tracing the resistance at half filling of a quartet, we can find the total magnetic field, B_T^*, at which this coincidence occurs, giving a measurement of this splitting,

$$\Delta_{\vec{D}} = g\mu_B B_T^*. \tag{4.4}$$

We performed this measurement over three high LLs in a single-gated high mobility bilayer graphene sample(Fig. 4.13a). Plotted in Fig. 4.13b is the constant temperature resistance of the half filled LLs where coincidence was within the experimental range. Because the traces are taken at fixed field, each filling appears at a fixed voltage, and consequently a fixed electric displacement. We want to find the constant of proportionality between the valley splitting and the displacement field: dividing the valley splitting measured through coincidence by the gate induced $\overline{D}$ and the perpendicular field, we find

$$\frac{\Delta_{\vec{D}}}{9.45\mathrm{T}} = 3.7\frac{\mathrm{K}}{\mathrm{T}\cdot\mathrm{V/nm}}. \tag{4.5}$$

This is several times larger than predicted by the two band model, but that is hardly surprising–at

the fields and densities under consideration, it is not likely to be accurate.

In addition to the tunability of its single particle symmetry breaking fields, bilayer graphene has two important intrinsic features which make it different from other clean two dimensional systems. First, the gapless parabolic spectrum at zero magnetic field is inherently unstable to interactions, and recently several groups [195–199] have observed signatures of new ground states (although the phenomenology of this ground state remains sample and location dependent as of this writing!). A second feature of bilayer graphene is the nature of its ZLL: unlike the higher LLs, and unlike all LLs in graphene, the ZLL in bilayer graphene is eightfold degenerate owing to the combination of the spin, valley, and 'accidental' orbital $|0\rangle, |1\rangle$ degeneracy. This last degeneracy renders the ZLL in bilayer graphene unique: unlike spin in valley, it is not 'spin-like' in any approximation and its orbital structure has been predicted to lead to a wealth of interesting ground states and excitations without analog in other 2DES[41, 200, 201].

Experimentally, exploration of the BLG octet LL has only just begun. As in the monolayer, the ability to fabricate high quality, multiterminal hBN supported graphene devices now makes a richer understanding possible. Figure 4.14 shows the evolution of the LLs as a function of magnetic field in a particularly high quality single-gated BLG on h-BN device ($\mu \gtrsim$ 100,000, with the measurement limited by the fact that the mean free path was likely considerably bigger than the 1μm$\times 1\mu$m device). Several striking features are apparent, in line with previous work[121, 125]: the even integer states, particularly $\nu = \pm 2$ and the insulator at $\nu = 0$, are strongly developed. Deep minima also appear at $\nu = \pm 1$ and ± 3, although these are not as strong as the even minima. This is because the odd minima appear as a result of the lifting of the orbital $|0\rangle, |1\rangle$ degeneracy, as pointed out in [41]. The orbital, rather than spin-like, nature of the $|0\rangle, |1\rangle$ degeneracy spoils the

electron-hole symmetry of the interacting ZLL in bilayer graphene. Indeed, in the experimental data a striking feature is the nonmonotonicity of the minimum at $\nu = -1$, which deepens, almost (but not completely) disappears, and the reemerges at higher fields. No such behavior is observed at $\nu = +1$. The nature of this transition between what may be different ground states is unknown, but provides further incentive to expand the studies of the bilayer octet, starting from the transport study of dual gated devices in variable/tilted magnetic field.

At the highest fields, FQHE emerges in high quality BLG on hBN samples. Figure 4.15 shows experimental evidence for FQHE taken from singly gated BLG devices. FQHE, from our limited experience, is more difficult to observe than in the monolayer, despite similar concentrations of disorder. When it does appear, it seems to be restricted almost exclusively to the non-octet, $N \geq 2$ LLs. OUr current heuristic understanding of this phenomenology is as follows. As in monolayer, in bilayer the gap size of the lowest order FQHE states is determined by the pseudospin structure of the FQH state; in particular, valley or (for the octet) orbital Skyrmion excitations may be cheaper energetically than excitations over the Λ-level gap, leading to smaller activation gaps. The octet orbital degeneracy may be particularly important in providing low lying modes, explaining the absence of observation of fractions. In the higher LLs, as in non-chiral parabolic 2DES, the electronic interactions are weaker due to the spreading o the LL wavefunctions, again potentially explaining the weakness of the FQHE. Where features are observed, the plateaus in R_{xy} are not sufficiently well formed to conclusively determine the filling factor; however, an estimate of the density suggests that most of the FQH signatures in the $N \geq 2$ LLs are associated with multiples of $\frac{1}{3}$. An exception is the only feature observed in the ZLL, Fig.4.15 right panel, which seems to lie closer to the midle of the LL, but this feature is too weakly formed to be labeled.

The weakness of FQHE in bilayer graphene is rather disappointing, as BLG is an extremely interesting system for the study of electronic interactions. The electronic correlations leading to the FQHE are governed by the so-called Haldane pseudopotentials[180], which describe the effective interaction. Due to the gate tunable weighting of components on the upper and lower layers of the bilayer, these pseudopotentials can be tuned electrostatically–effectively changing the interaction potential felt by the electrons within a single LL. The immediate question is: can the pseudopotentials be tuned to create the conditions for existence of any particularly interesting state, or the transition between states? Several theoretical calculations [181, 202–204] seem to answer this question in the affirmative, predicting both gate tunable transitions to FQH states and a range of parameters in which a stable Pfaffian exists. As the quality of dual gates samples improve, the study of FQHE in bilayer graphene promises to be an exciting field.

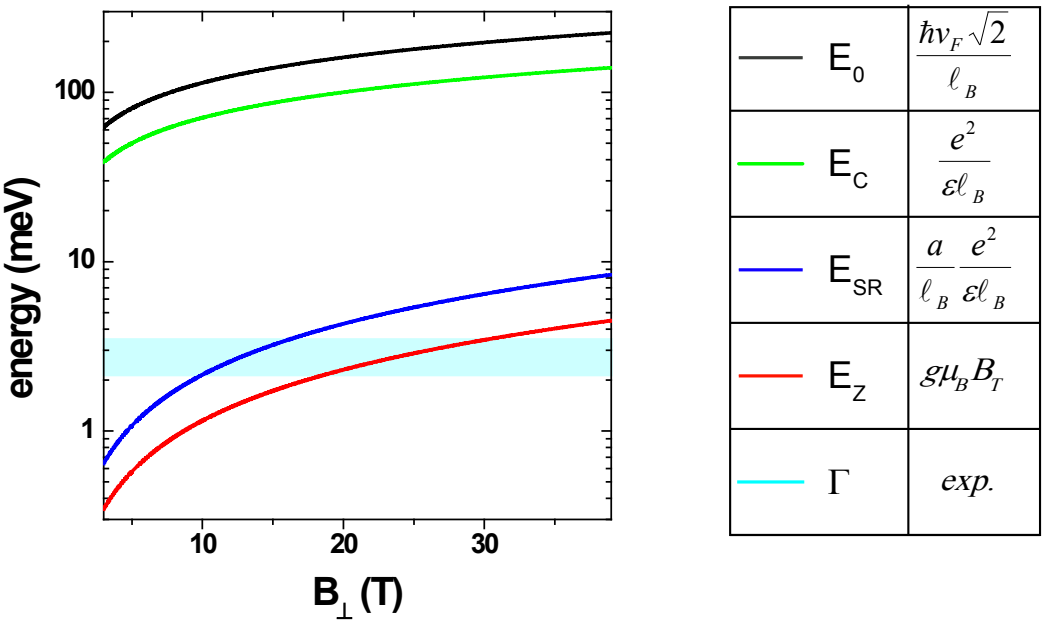

Figure 4.1: Energy scales in the graphene quantum Hall ferromagnet
The cyclotron energy (E_N) and Coulomb energy (E_C) both characterize physics that does not distinguish between isospin flavors. Both are at least one order of magnitude larger than the energies associated with the leading isospin anisotropies, which include the Zeeman effect (E_Z), lattice scale interactions (E_{SR}), and disorder (Γ). v_F is the Fermi velocity in graphene, a is the lattice constant, g_0 is the bare gyromagnetic ratio, and μ_B is the Bohr magneton. The disorder energy scale is extracted from the magnetic field dependence of Shubnikov-de Haas oscillations, see Figure 4.3.

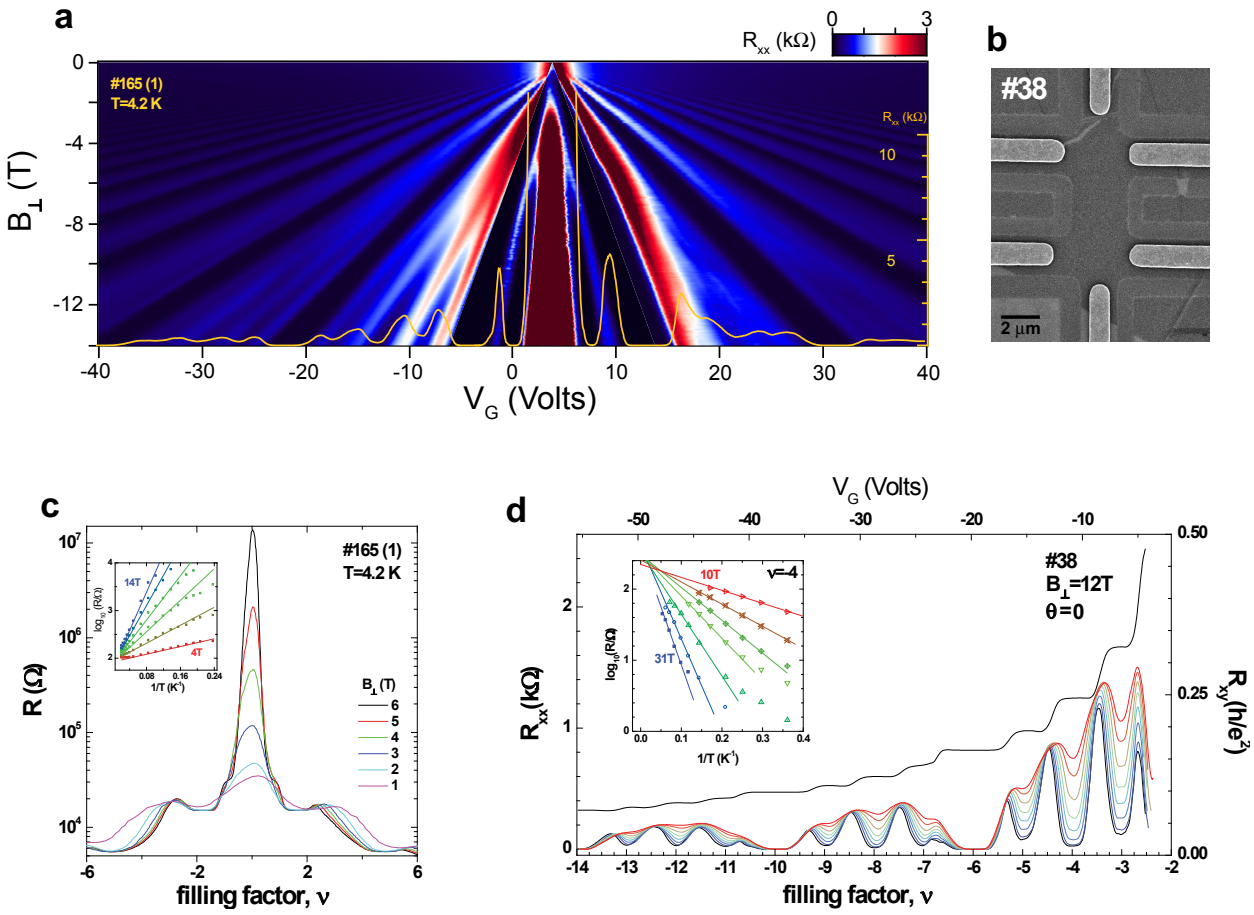

Figure 4.2: All integer quantum Hall effect in graphene on h-BN

(a) Landau fan from a monolayer graphene on h-BN device. Symmetry breaking of the Landau levels is visible from a few tesla, and at $B_\perp = 14T$ (superimposed) all integer filling factors feature minima in R_{xx}. The color scale for $-2 < \nu < 2$ has been expanded by a factor of 7. (b) SEM micrograph of a typical etched Hall bar device. (c) Development of the $\nu = 0$ insulating state. Inset: temperature dependence showing the Arrhenius behavior of the insulating resistance. (d) Temperature dependence of the R_{xx} minima in the symmetry broken IQHE regime. Inset: Arrhenius plots for $\nu = 4$ as a function of magnetic field.

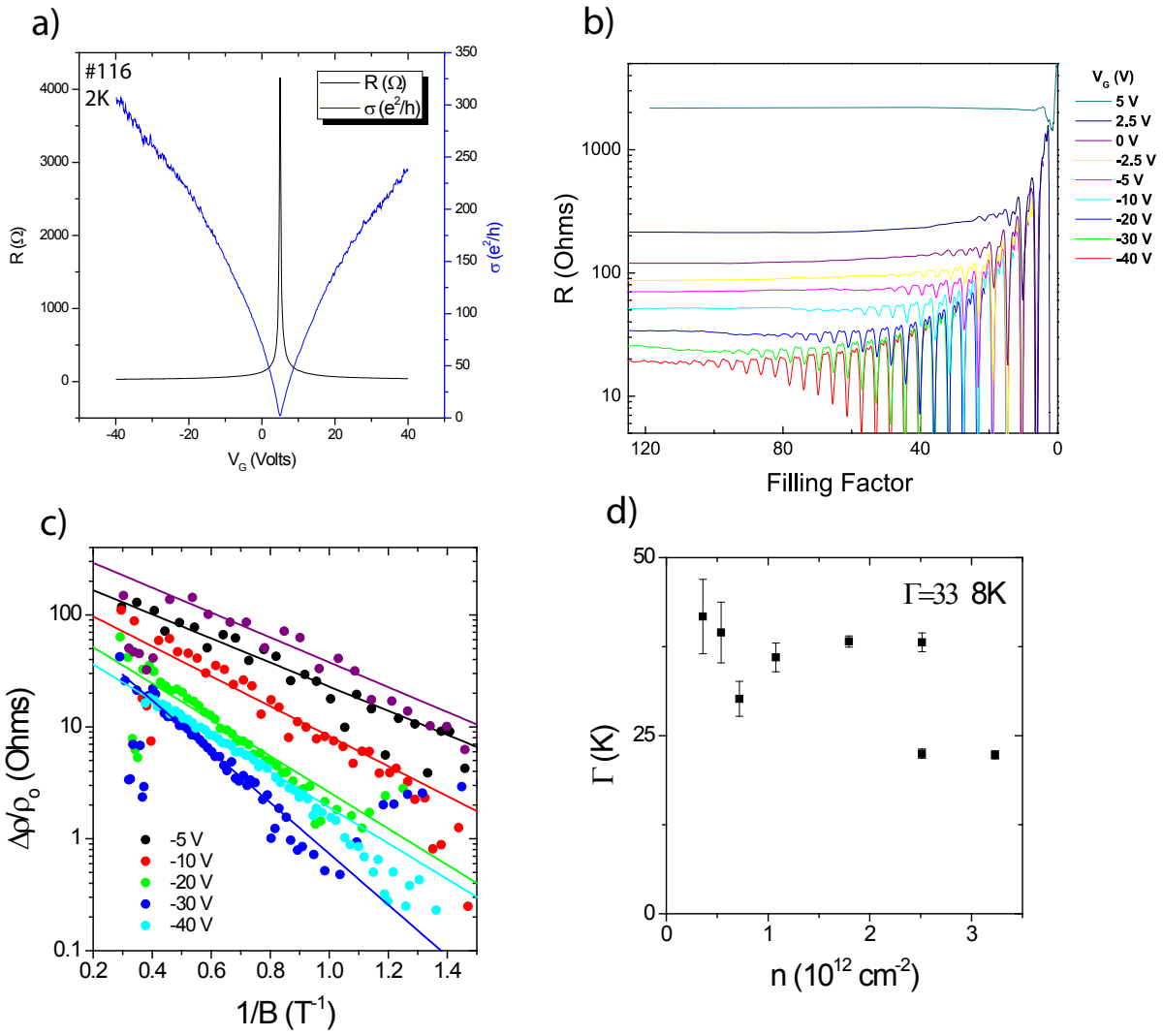

Figure 4.3: Dingle temperature in a hBN supported graphene device
a) Resistance (black) and conductivity (blue) for device #116. b) Resistance as a function of filling factor for different, constant gate voltages. c) Oscillation amplitude $\Delta\rho$ for different gate voltages. d) LL broadening Γ as extracted from linear fits to $\log \Delta\rho$ vs. $1/B$ plots in panel c.

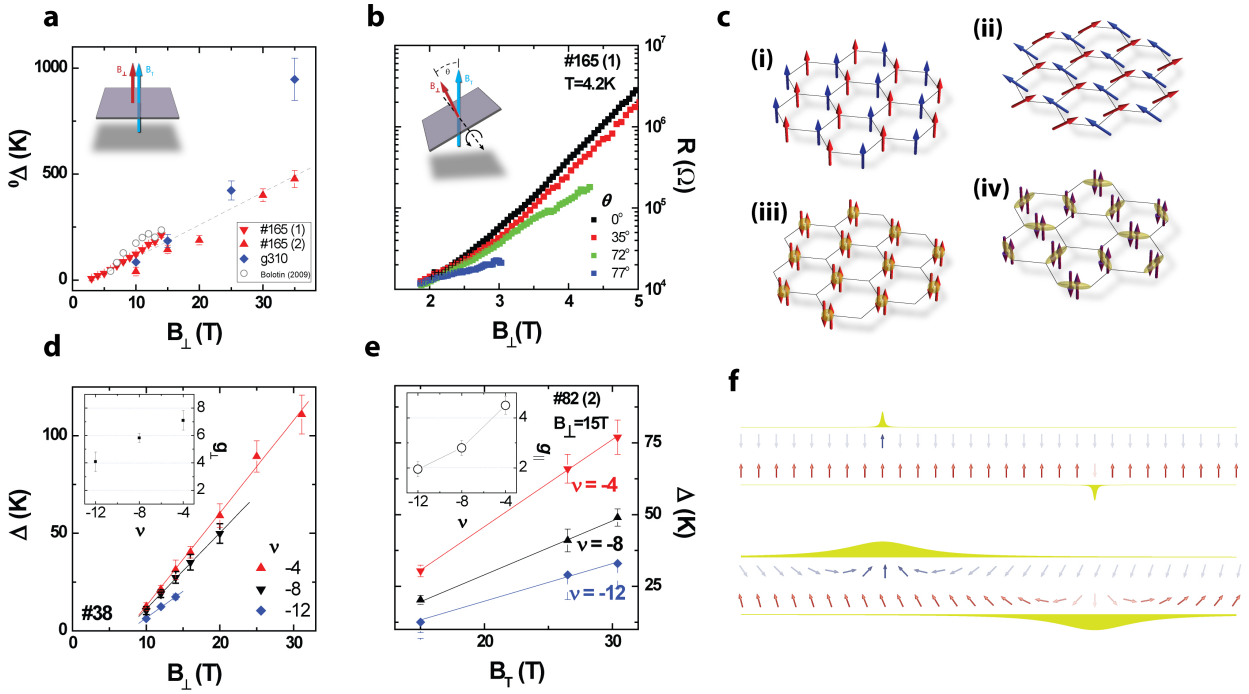

Figure 4.4: Activation gaps of half filled quartet Landau levels.
a) $B_\perp$ dependence of the $\nu = 0$ gap, ${}^0\Delta$, for several devices. ${}^0\Delta$ increases approximately linearly with applied $B_\perp$, a feature not associated with any currently proposed theory for the $\nu = 0$. The dashed line indicates $g_\perp = 23$. b) Tilted field dependence of the resistance of the $\nu = 0$ state. The resistance increases exponentially with field, consistent with a gapped state with ${}^0\Delta \propto B_\perp$. The resistance at fixed $B_\perp$ decreases for higher tilt angles, indicating a spin-unpolarized state. c) Candidate QHFM states for the $\nu = 0$. Our experiment rules out the spin ferromagnet, (**i**); all other states are marked by lattice scale spin (for the canted antiferromagnet, (**ii**)) or charge (for the charge density wave (**iii**) or Kekulé distortion (**iv**)) order. d) $B_\perp$ dependence of the half filled quartets for $N \neq 0$, ν=-4,-8,-12. Like the $\nu = 0$, all gaps scale approximately linearly with $B_\perp$, with enhanced $g_\perp$ factors that decrease with increasing LL index. e) Unlike the $\nu = 0$ state, all activation gaps measured for half-filled LLs with $N \neq 0$ increase with B_T, indicating spin polarized states. For ν=-4 and -8, the enhancement of $g_\parallel$ indicates that charged excitations contain multiple flipped spins. f) Schematic of charged excitations at half filling for $N \neq 0$. Excitations into the spin-reversed conduction band can take the form of single reversed spin particle hole pairs or smoothly varying Skyrmion-antiSkyrmion (S-aS) spin textures, depending on the strength of exchange interactions relative to disorder and the Zeeman energy. At $B_\perp = 15T$ in the samples studied in this work, the S-aS scenario prevails at ν=-4 and -8, while charge at ν=-12 is carried by single electron hole pairs.

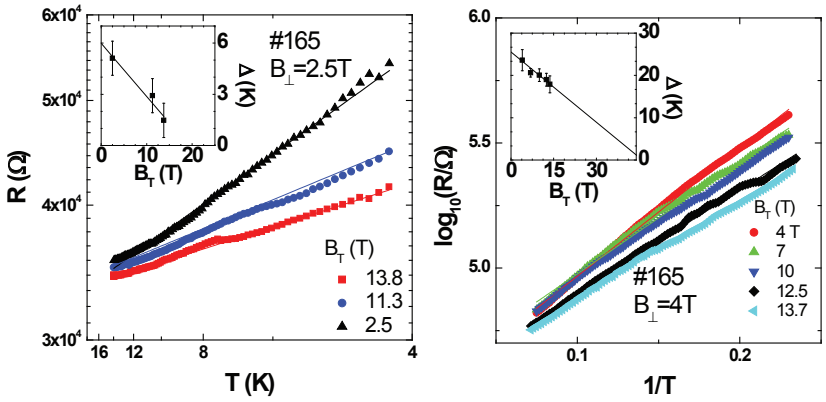

Figure 4.5: Tilted field temperature dependence of the $\nu = 0$ state
Temperature dependent resistance of the $\nu = 0$ insulator taken at $B_\perp$=2.5 T (left) and $B_\perp$=4 T. The estimates for the energy scales of the insulating gap suggest that the gap should close for cleaner samples, where the insulator is well developed by 1-2 Tesla, in magnetic fields of $\leq 45T$.

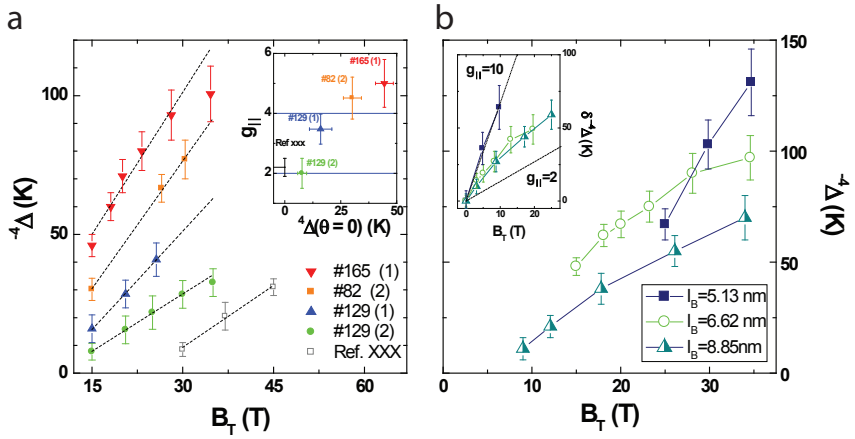

Figure 4.6: Skyrmions at ν=-4.
(a) Device dependence of $^{-4}\Delta$. Cleaner devices show both larger activation gaps (at all fillings) and larger slopes, $\partial_{B_\perp}$ ($^{-4}\Delta$), for fixed ℓ_B. This trend is observed both across devices and for the same device before and after a contamination event, e.g. device #129. (b) Perpendicular field dependence of $g_{\|}$ at ν=-4. The three curves show tilted field dependence of $^{-4}\Delta$ for three different values of the magnetic length, $\ell_B^2 = \frac{\hbar c}{eB_\perp}$. Contrary to the theory of Skyrmions transport in a clean QHFM, in which the Skyrmion size is negatively correlated with the ratio $E_Z/E_C \sim B_T/\sqrt{B_\perp}$, the number of flipped spins appears to be positively correlated with $B_\perp$, although slightly negatively correlated with E_Z for fixed ℓ_B. Taken together with (a), we conclude that disorder plays an important role in Skyrmion transport in graphene, and likely constitutes the major control on Skyrmion size[173] in our graphene samples.

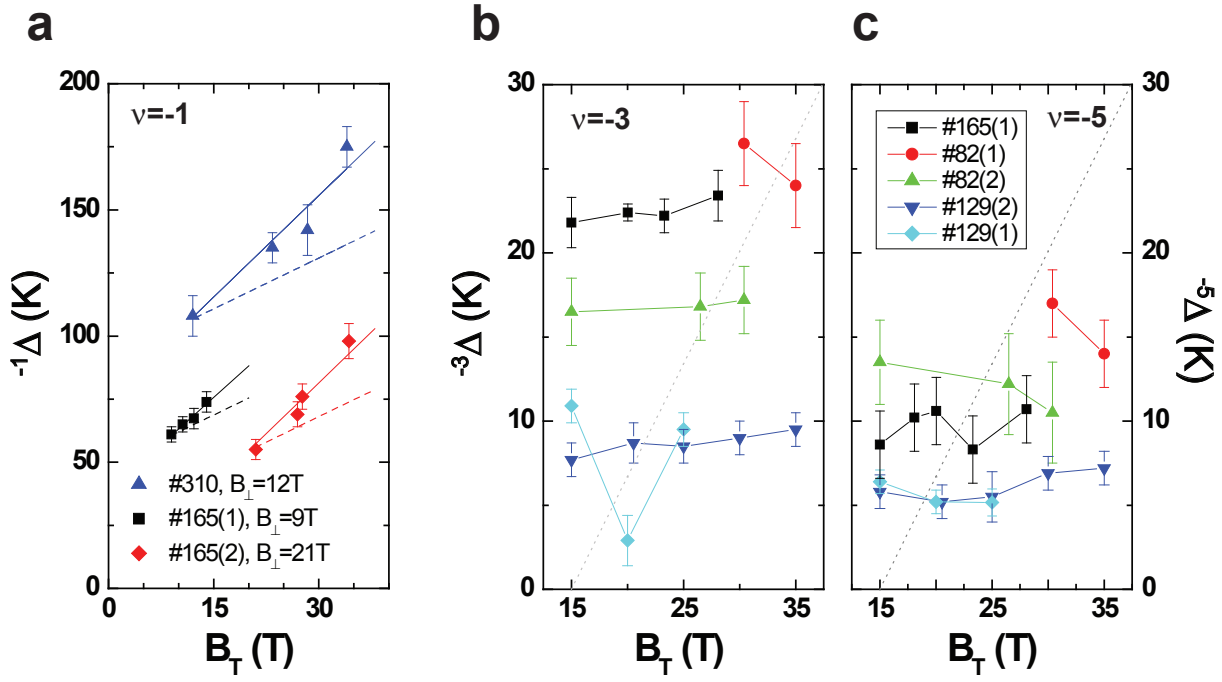

Figure 4.7: Tilted field transport at quarter filling

(a) ν=-1. Energy gaps increase with B_T, suggesting that excitations from the expected spin polarized, sublattice polarized state[20, 139, 142] involve real spin flips. Dependence on B_T appears to support enhancement of $g_{||}$ (solid lines are best linear fits to the data; dashed lines show $g_{||} = 2$ for reference). (b-c) Tilt dependence of ν=-3 and ν=-5. Most samples show minimal dependence on B_T, consistent with theoretical predictions of valley-textured excitations[138]. Note reentrant behavior in sample #129 (see Fig. 4.8). Dashed lines show $g_{||} = 2$ for comparison.

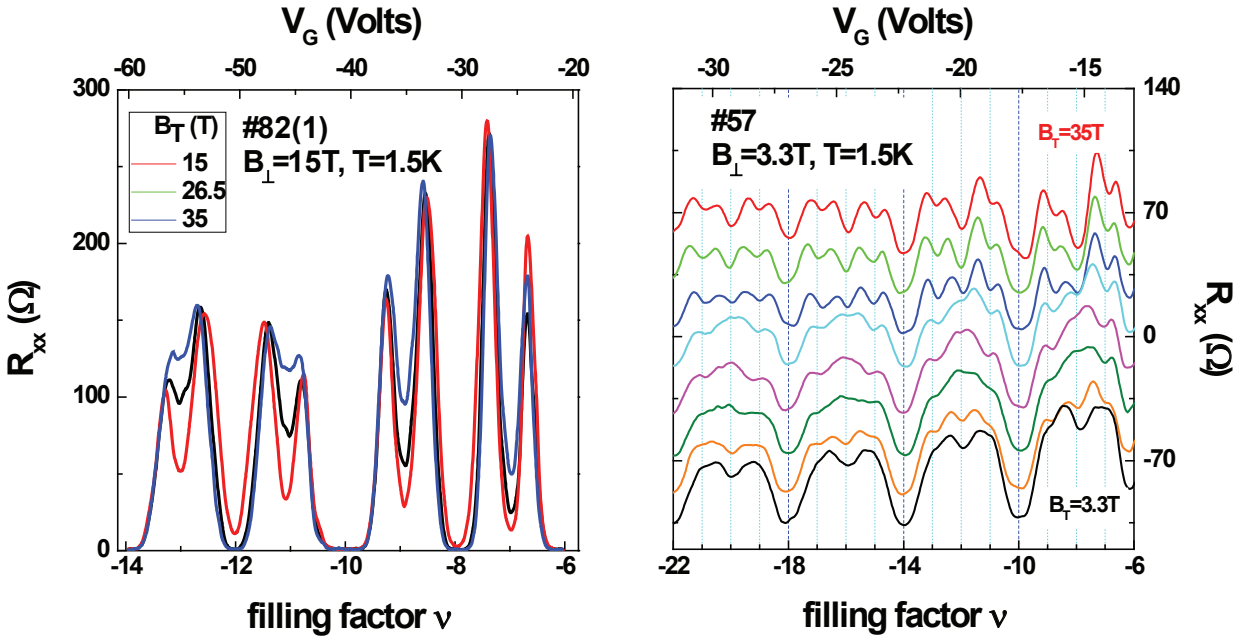

Figure 4.8: Reentrant QHE in tilted field in the higher LLs

(a) Gap collapse at odd filling. Gaps at quarter filling in the $N \neq 0$ LLs collapse in applied in-plane field in selected samples. Gap collapse, or collapse and reemergence (cf. $(-3)\Delta$ in device #129 (1), Fig. 4.7) is device dependent. In the two devices in which it was observed, the behavior did not survive a contamination event. (b) At very low perpendicular magnetic fields, an additional minimum is visible only at half filling. With the addition of an in-plane field, this minimum disappears, before reemerging again as B_T is increased further. Simultaneously, minima at quarter filling emerge with increasing B_T, indicating that they too can be spin active, increasing with B_T.

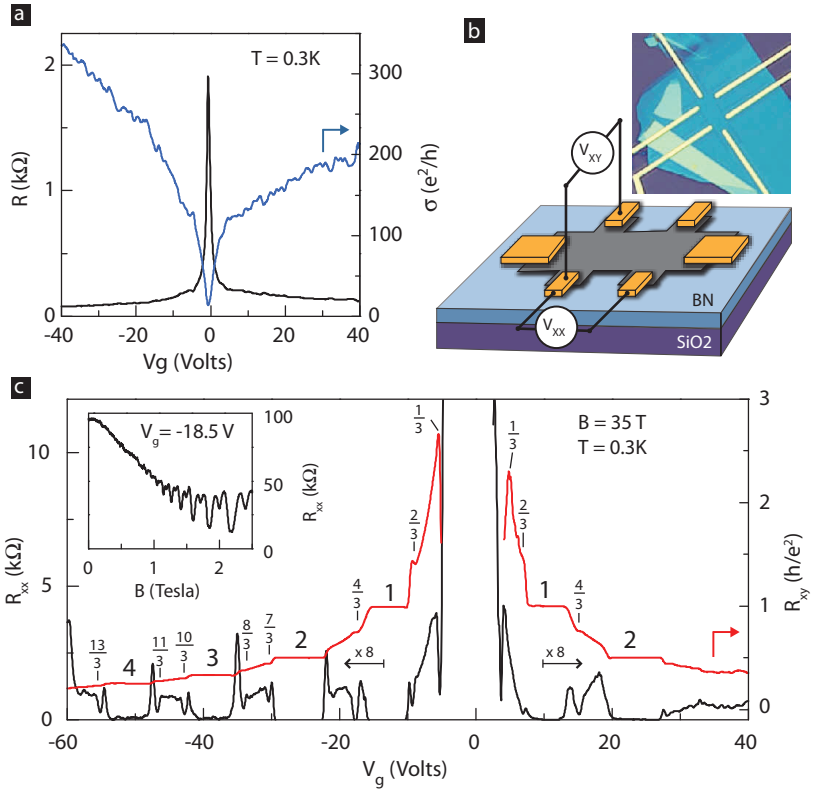

Figure 4.9: Schematic of a graphene device showing FQHE
(a) Resistance and conductivity measured at zero magnetic field. (b) Schematic of the etched hall bar device. Inset: Optical image; scale bar is 5 μm. (c)Magnetoresistance (left axis) and Hall resistance (right axis) versus gate voltage acquired at $B = 35$ T. Inset shows SdH oscillations at $V_g = -18.5$ V.

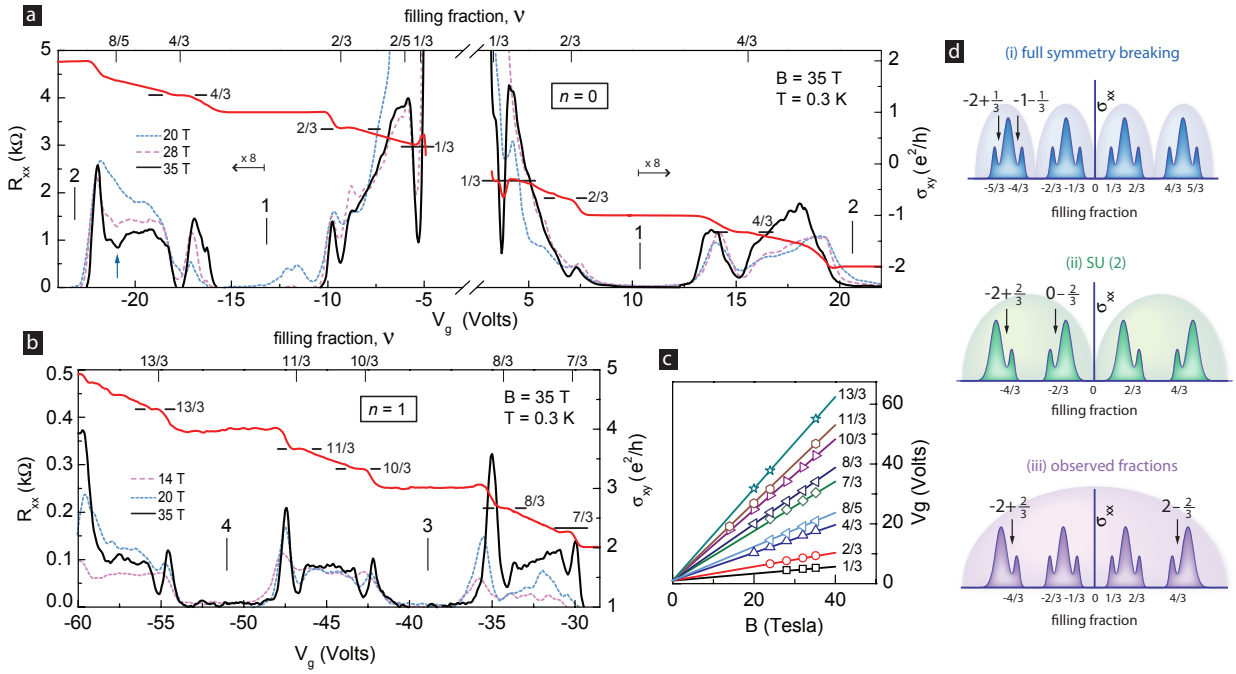

Figure 4.10: Fractional quantum Hall effect.
(a),(b) Magnetoresistance (left axis) and Hall conductivity (right axis) in the $n = 0$ and $n = 1$ Landau levels at $B = 35$ T. $T \sim$0.3 K. (c) Fan diagram showing the resistance minima at different magnetic fields for the FQHE states labeled in (a) and (b). Lines correspond to the positions calculated from the relation $B_\nu = \frac{1}{\nu} n_e h/e$, where $n_e = C_g(V–V_o)/e$ is the carrier density and $C_g = 1.09 \times 10^{-4}$ F/m^2 the capacitive coupling to the doped Si back gate, determined independently from low B Hall measurements. (d) Cartoon depiction of the FQHE hierarchy observed in our sample. Shown is the expected electron-hole symmetry assuming (i) full lifting of all internal degeneracies due to, for example, coupling to external fields, (ii) full breaking of only one degeneracy, leaving a twofold degenerate branch, (iii) schematic diagram of the experimental situation. Arrows label particle-hole conjugate pairs in each scenario.

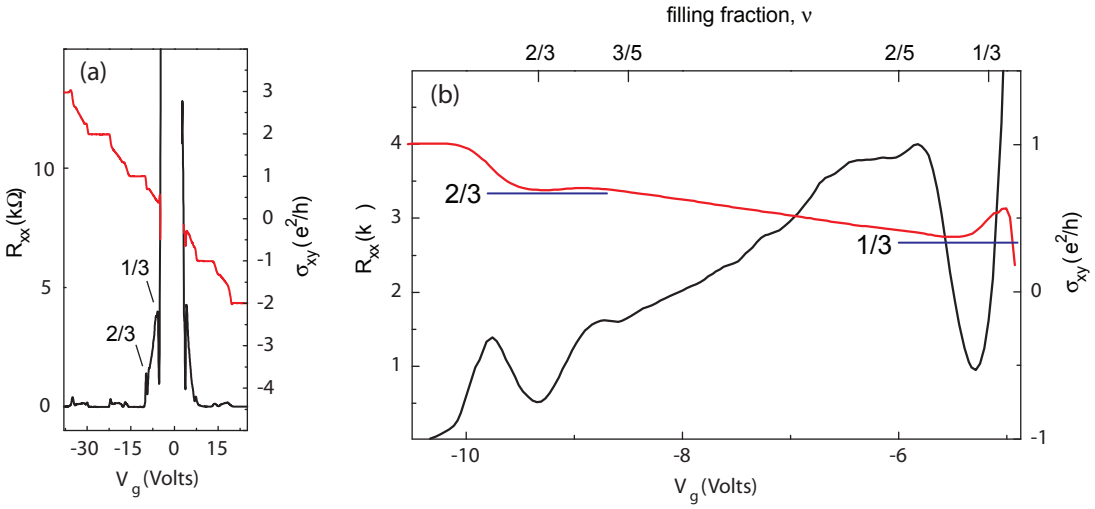

Figure 4.11: FQHE close the charge neutrality point
(a)Magnetoresistance (left axis) and Hall conductivity (right axis) over a large density range. The insulating phase appearing at the charge neutrality point strongly affects transport between ν=-1 and ν=1. (b) Detail of the magnetoresistance (left axis) and Hall conductivity (right axis) near the 1/3 and 2/3 FQH states. Horizontal lines indicate the expected value of the Hall quantization. Filling factor appears on the top axis, with expected minima positions marked at ν = 1/3 and 2/3. The position of the 2/5 and 3/5, corresponding to the nearest FQHE states in the standard CF series, are also labeled for comparison.

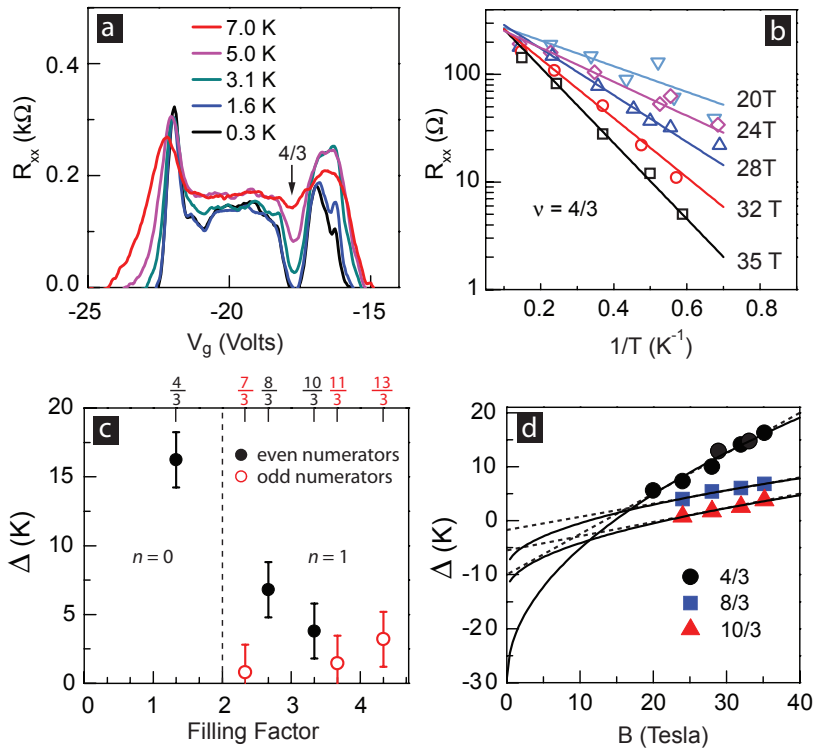

Figure 4.12: FQHE energy Gaps.
(a) Magnetoresistance versus temperature near $\nu = \frac{4}{3}$ at $B = 35$ T. (b) Arrhenius plot of the R_{xx} minimum at $\nu = \frac{4}{3}$ for several magnetic fields. Energy gaps versus filling factor at $B = 35$ T and versus perpendicular magnetic field are shown in (c) and (d). Dashed and solid lines in (d) are fits assuming linear and $\sqrt{B}$ dependence, respectively.

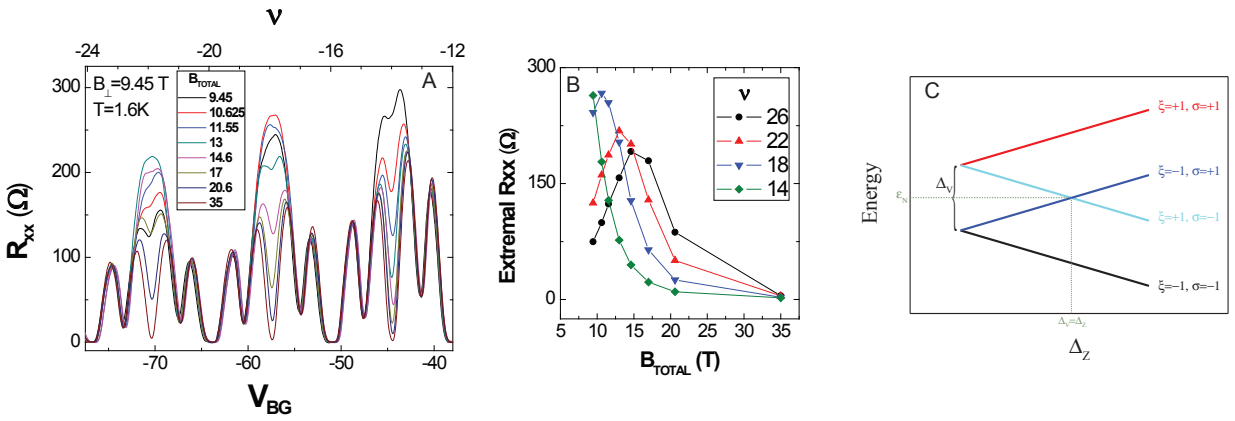

Figure 4.13: Intra-Landau level SdH coincidence in bilayer graphene $N \geq 2$ LLs
(a) Rxx as a function of gate voltage for fix $B_\perp = 9.45T$ and different values of B_T. At half filling of the quartet LLs, minima grow deeper or shallower with applied in-plane field depending on whether the gap at B_T=9.45T

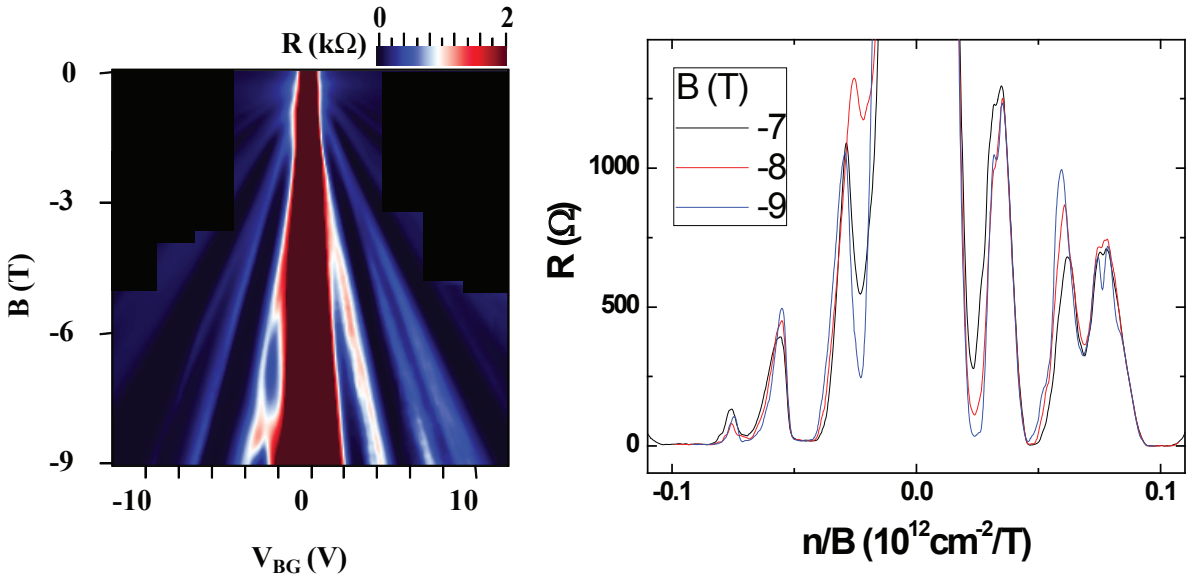

Figure 4.14: Symmetry breaking in the bilayer graphene octet

Data

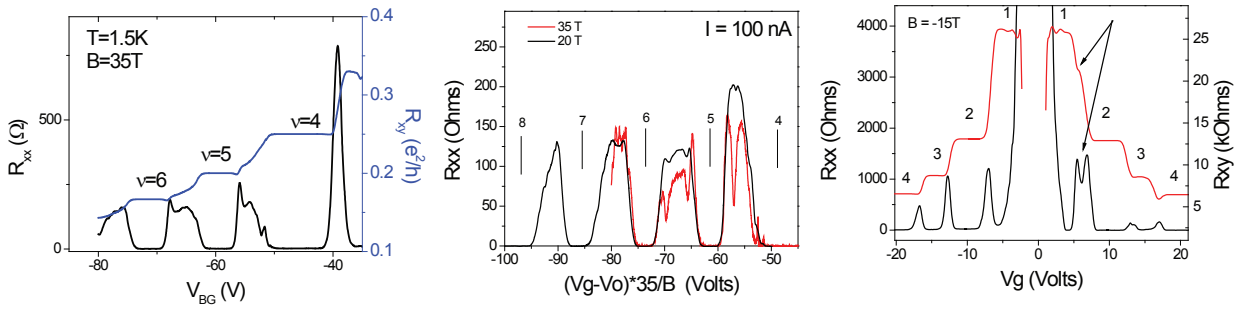

Figure 4.15: FQHE in bilayer graphene

Data taken from several devices showing signature of the the FQHE. In the leftmost and center panel several Rxx minima appear at fractional filling in the quartet LLs. In the right panel, a single feature appears between fillings 1 and 2.

Chapter 5

Capacitance measurements in bilayer graphene

Attempts to measure the quantum capacitance of bilayer graphene were originally motivated by technological challenge of gap engineering. Whereas in the monolayer a gap can be opened only by a potential modulation on the spatial scale of the lattice constant [115], in BLG the relevant sublattices are located on different layers, allowing a gap to be induced by a modulation of the interlayer imbalance *via* the application of an electric field perpendicular to the BLG planes [123, 123, 124]. Although the field-effect tunable gap in BLG has been observed optically [205–207], transport measurements show hopping conductivity at low temperatures. [82, 208, 209]

Capacitance measurements probe the energy cost of moving charge between different parts of a system. In a classical system, this energy cost is a purely geometric quantity and consists of the electrostatic energy. In contrast, capacitance measurements performed on quantum systems can access a range of subtle and interesting phenomena. In particular, Pauli exclusion in degenerate electronic systems gives rise to a characteristic quantum contribution to the internal energy. The associated contribution to capacitance, known as 'quantum capacitance' [210], is proportional to the electronic compressibility $\frac{\partial n}{\partial \mu}$. For a dual gated graphene device, for example, the differential

capacitance measured from the top gate is

$$C_T = \left(\frac{1}{C_T^0} + \frac{1}{e^2 A \nu} \right)^{-1} + C_{para} + \mathcal{O}\left(\frac{C_B^0}{C_T^0} \right) \tag{5.1}$$

where $C_{T(B)}^0$ is the classical geometric capacitance between top (back) gate and graphene, C_{para} is any stray parallel capacitance, A is the area of the device, and $\nu \equiv \frac{\partial n}{\partial \mu}$. In addition, at low carrier densities, the internal energy is dominated by electronic correlations, resulting in a so-called negative compressibility contribution to capacitance [211]. In low dimensional systems these effects can amount to a sizeable contribution, making capacitance measurements a powerful probe of many-body effects [212]. Moreover, whereas electrical transport is often dominated by a small subset of electronic states, capacitance probes all states equally. Consequently, capacitance is a useful tool in the study of phenomena in which localization plays a role, such as quantum Hall effects and the metal-insulator transition [212–216]. Under certain conditions, the quantum capacitance can become an order-one effect [217, 218].

In this section I describe capacitance measurements performed in 2009-2010 on bilayer graphene[19], and, as of the time of this writing, under review at Physical Review B. As discussed in the introduction, bilayer graphene is in many ways the 'perfect' two dimensional electron system: with two parallel gates, both the density and the interlayer bias can be controlled independently. Features of the experimental data discussed below led to a proposal to directly probe both gate induced and spontaneous interlayer polarization through capacitance measurements, which can be found in [28].

5.1 Capacitance experiments on SiO_2 supported mono- and bilayer graphene

To produce dual gated graphene devices with high geometric capacitance, we utilize single crystal hexagonal boron nitride (h-BN) flakes [219] as the top gate dielectric. The detailed device fabrication process using h-BN are similar to those presented in [40]. The devices used for the capacitance measurements described here were produced using the warm KOH underetch method [220]. hBN crystals are exfoliated onto SiO_2 substates, coated in PMMA, and the film is them removed by floating the chip on warm KOH, which rapidly etches the PMMA/SiO_2 interface. Flakes are then transfered using the same apparatus described in Fig. 3.3, followed by electron beam lithography to form contact electrodes and a local top gate. The heavily doped silicon substrate, coated with 285 nm oxide, serves as bottom gate. We find that h-BN is an excellent gate dielectric, with $\varepsilon \sim$ 3-4 and breakdown fields comparable ($\sim$.8 V/nm) to SiO_2 thin films. In addition, we observe minimal degradation of graphene samples, with no additional doping contributed by the presence of the top gate and typical post h-BN transfer mobilities of $\mu \sim$5000-10,000 cm^2/V sec for graphene monolayers and $\mu \sim$2000-3,000 cm^2/V sec for bilayers.

Low temperature capacitance measurements were performed using a simple capacitance bridge circuit. All wires were shielded, and the sample package itself was encased in a Faraday cage to further reduce parasitic capacitances, which represent an additive constant to the measured value of C_T. A ceramic multilayer capacitor with minimal temperature dependence was chosen for the reference capacitor and connected near the sample at low temperature. The noise level of the bridge was $\sim$25 $e/\sqrt{Hz}$, allowing sub-femtofarad resolution with averaging times of less than 30 seconds for our typical top gate excitation voltage of 15-50 mV. For the variable temperature capacitance measurements, we applied a 50 mV AC excitation voltage on top of the DC gate bias

and measured the current through the graphene device. Although this method results in poorer STN than the bridge measurement, it eliminates calibration errors stemming from the small temperature dependence of the reference capacitor.

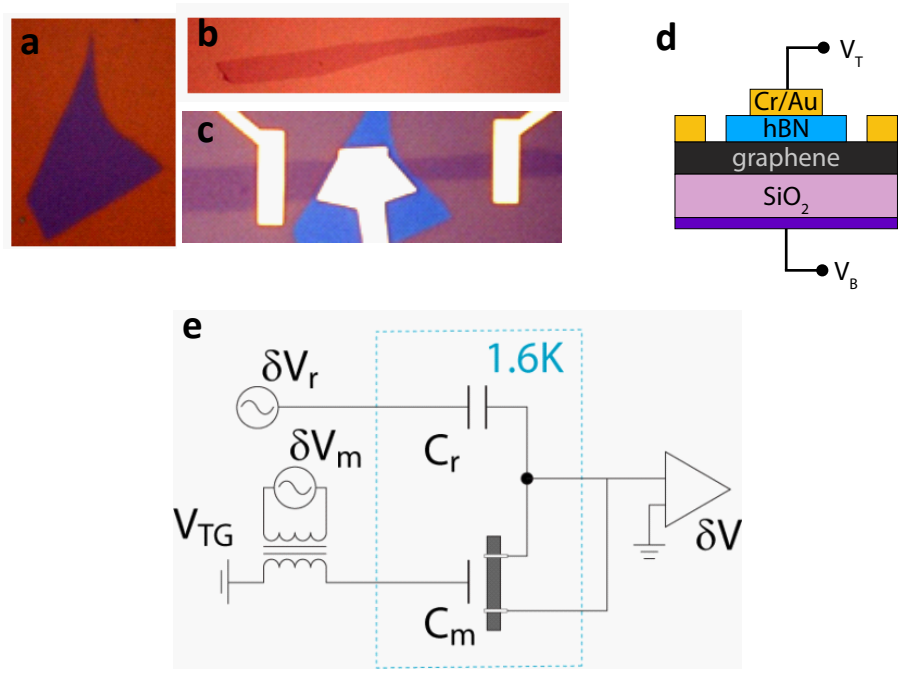

Figure 5.1: Graphene-hBN capacitor and capacitance bridge device schematic
A single crystal h-BN flake (a) is transferred onto mono- or bilayer graphene (b) and contacts deposited using electron beam lithography (c). Black bars are 10 μm. (d) Device schematic. (e) Schematic circuit diagram of the capacitance bridge. A reference capoacitor (Johanson Technology 0603/R14S) is mounted on the probe, and a reference voltage is chosen to balance the capacitance bridge. A small AC excitation signal is added to the DC gate bias through a transformer (Triad Magnetics SP67).

Fig. 5.2 shows the measured capacitance C and conductance G of MLG as a function of top gate voltage V_{TG} at both zero and high magnetic fields. The lowered compressibility stemming from the linear spectrum of of MLG can be inferred from a depression in the capacitance at zero

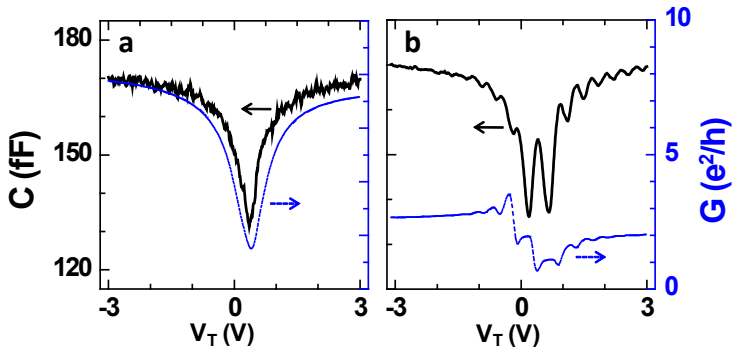

Figure 5.2: Monolayer graphene capacitance and conductance data
Measured conductance and capacitance of monolayer graphene at 2K and B=0 (a) and B=9T (b). In (a), capacitance and conductance resemble each other closely due to the fact that both contain a spurious contribution adding "in parallel"; $G = (1/R + 1/R_{contact})^{-1}$ and $C_T = (1/C_Q + 1/C_T^0)^{-1}$ where R is the device resistance, C_Q is the compressibility, or "quantum capacitance," C_T^0 is the geometric capcacitance, and $R_{contact}$ is the contact resistance of our two-terminal devices.

density, while at high B the formation of the n =0 Landau level (LL) leads to a peak at charge neutrality [108]. The high magnetic field capacitance traces show compressibility oscillations due to the formation of higher LLs, while conductance shows the electron-hole asymmetry that is the signature of edge state transport in graphene heterojunctions [59, 60, 221].

In the remainder of this section, we present capacitance and transport data from the dual-gated BLG sample shown in Fig. 5.1 a-c. Using Eq. 5.1 we extract the compressibility from the capacitance as a function of density, n, temperature T, and electronic displacement $\overline{D} = \frac{\varepsilon_B}{d_B}\left((V_B - V_B^0) - \frac{C_T^0}{C_B^0}(V_T - V_T^0)\right)$ where ε_B and d_B are the dielectric constant and depth of the back gate dielectric layer, $V_{T(B)}$ is the applied voltage to the top (back) gate, and $V_{T(B)}^0$ is the voltage offset required to obtain minimal density and displacement in the top- gated region. At charge neutrality and a large applied displacement fields, we observe a finite minimum in capacitance,

confirming the presence of localized states in the bulk in our strongly disordered, SiO_2 supported samples. In contrast to transport measurements, however, the band gap can still be measured from the simply activated temperature dependence of the extracted minimal compressibility. By analyzing the asymmetric appearance of a feature associated with the 1D-like, $\sqrt{\varepsilon}$ van Hove singularity, we show from top gate capacitance data that perpendicular electric field breaks the interlayer symmetry, leading to the onset of a finite layer polarization.

Fig. 5.3 shows the capacitance of a BLG sample at 1.6 K measured with the cold bridge. Tuning external gates adjusts both n and $\overline{D}$. For small values of $\overline{D} \approx 0$, capacitance exhibits a minimum at $n = 0$ as expected for ungapped bilayer graphene, which has a hyperbolic band structure. As $|\overline{D}|$ increases, the $n = 0$ minimum gets deeper, corresponding to the formation of a gap in the energy spectrum. This minimum, however, does not go to zero, and in fact the capacitance modulation is only 10%. In addition, a distinct local maximum develops next to the minimum. The presence of both the dip and local peak in ν at high $|\overline{D}|$ can be understood, at least qualitatively, from the band structure of gapped BLG, once the effects of disorder [222] and the interlayer separation [28] are taken into account.

Within the nearest-neighbor tight binding approximation, the energy spectrum of pristine, Bernal stacked bilayer graphene with finite interlayer asymmetry Δ is gapped and has a "Mexican hat" structure, with the band extrema occurring at finite k_0 such that $\varepsilon_{k_0} \sim \pm\Delta/\sqrt{2}$. The energy scale of the "Mexican hat" is small, $\varepsilon_m \sim \Delta^3/4\gamma_0^2 \lesssim 5$ meV for the gap sizes probed in this experiment, and less than the energy scale of potential fluctuations arising from disorder [108]. However, even in the presence of strong disorder, the absence of a positive quadratic term in the energy spectrum turns the problem of gapped, disordered bilayer graphene into one of a heavily

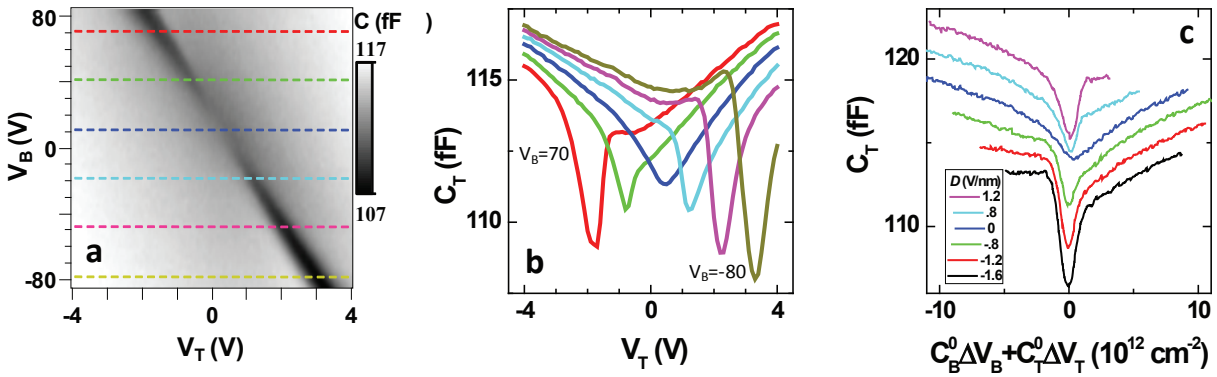

Figure 5.3: Capacitance of dual gated bilayer graphene
Capacitance at B=0 and 1.6 K as a function of V_T and V_B. Colored traces in (b) are taken at 30 volt intervals in V_B, corresponding to the colored lines in (a). (c) Traces at constant $\overline{D}$, extracted from the data set shown in (a). Data is plotted as a function of $C_T^0\Delta V_T + C_B^0\Delta V_B$, which would correspond to the density were the bilayer perfectly 2 dimensional and perfectly compressible. Curves in (c) are offset for clarity.

doped semiconductor with *quartic* energy bands [223]. We thus expect vestiges of a $\nu \propto 1/\sqrt{\varepsilon}$ vHs-like feature to be present even in our disordered (μ ~2,000 cm^2/V sec) samples, manifesting as a nonmonotonic-in- density feature at the band edge.

In addition to smearing the band edge vHs, disorder has a large effect on compressibility at charge neutrality in the presence of a large gap. In contrast to clean semiconductors, in which the depleted system is incompressible, our measured capacitance remains finite and large even for large $\overline{D}$, a fact we attribute to disorder-induced tails in the density of states [224]. This explains the discrepancy between energy scales that govern transport [82] and the gap energies observed optically [205–207]. It also suggests that recently predicted topological edge conduction [225] is

not the dominant reason for incomplete "turn-off" in BLG devices of typical quality.

Quantitative analysis of the capacitance data requires extracting the compressibility ν from the measured signal, C_T. For a perfectly two dimensional electron system ($C_{BL} \to \infty$), the measured capacitance (per unit area) is

$$C_T^{-1} = \left(\frac{1}{C_T^0} + \frac{1}{e^2 \nu} \right)^{-1} + C_{para} + \mathcal{O}\left(\frac{C_B^0}{C_T^0} \right), \tag{5.2}$$

where C_{para} are all parasitic capacitances between gate and contact electrodes. Extracting ν thus requires subtracting both a parallel (C_{para}) and series C_T^0 capacitances. We determined C_T from the device area (A =31 μm^2 from optical microscope images) and the ratio of the back and top gate capacitances, measured by tracking the charge neutrality point in the V_T-V_B plane (see inset to Fig. 5.3a). For the BLG device presented in this paper, we measured and C_T/C_B =29.5$\pm$.4, where $C_B = 115$ aF/μm^2 is the geometric capacitance of the bottom gate. As disordered BLG devices cannot be turned off completely, C_P cannot be measured *in situ* as has been done in GaAs heterostructures [226] and semiconducting carbon nanotubes [214]. Instead, we determine C_P=16$\pm$1 fF by removing the graphene through a short oxygen plasma etch and measuring the remaining capacitance between the metal contacts and the top gate. C_P constitutes about 10% of the total capacitance signal. Due to the subsequent subtraction of the (series) geometric capacitance C_T, the error in determination of C_P is least important when the capacitance differs considerably from the geometric value. This is the regime in which we perform a quantitative analysis of the compressibility of gapped BLG.

Near overall charge neutrality at $|\overline{D}| \gg 0$, our samples show a hopping conductivity similar to that observed in [82] from 1 K to $\sim$ 150 K. Capacitance instead shows no significant temperature

dependence up to 50 K, thereafter following a simply activated dependence (Fig. 5.4b). This is consistent with the presence of disorder-induced tails in the density of states throughout the band gap. Whereas temperature dependent transport is dominated by the hopping between these localized states, temperature dependent capacitance is dominated by thermal population of the much larger density of states near the band edge. This allows us to obtain an independent estimate of the band gap (inset to Fig. 5.4b), which we find to be ~ 75 meV for $\overline{D} \sim 1$, in agreement with infrared spectroscopy [206, 207].

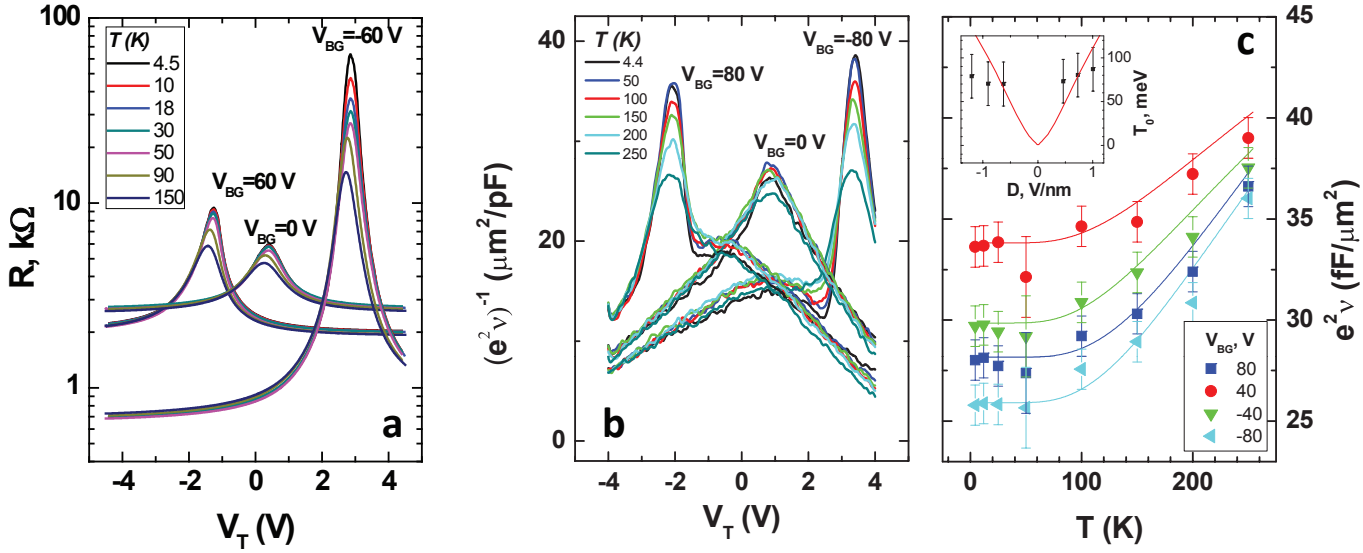

Figure 5.4: Temperature dependence of capacitance and resistance in biased bilayer graphene (a) Temperature dependence of resistance for $V_B = 60$, 0 and -60 V. The resistance is strongly temperature dependent at low temperatures, indicating hopping conductivity. (b) Temperature dependence of $(e^2\nu)^{-1}$ for $V_B = 80$, 0 and -80 V. (c) Temperature dependence of the minimal compressibility $e^2\nu$(n=0). Curves were fit with a simply activated temperature dependence, $\nu(T) = \nu(T = 4.4K) + \nu_1 e^{-T_0/T}$, where ν_1 and T_0 are free fitting parameters. A single value of C_P is chosen for all gate voltages, but is allowed to vary with T so that the curves match at high density. Inset: values of T_0 as a function of $\overline{D}$. Solid line is as in Fig. 5.3b (inset).

The most interesting feature of the data are the local maxima observed at the band edges:

these are associated with the 1D vHs inherent in the BLG band structure [222, 223]. As shown in Fig. 5.5, this cusp coincides with the onset of the strongly temperature dependent resistance characteristic of charge neutrality when displacement field is large. The cusps mark the 'mobility edge' associated with the boundary between the localized states in disordered, neutral graphene and the plane-wave like extended state which render the high-density temperature dependence metallic [227]. In simple language, by measuring both the conductivity σ and the density of states ν, we can isolate the contributions of ν and τ to the Drude conductivity, $\sigma = \nu e^2 \tau$. The absence of nonmonotonic features in the conductivity, and the disproportionate change in resistance, as compared with the measured capacitance, at high $\overline{D}$, suggest that changes in τ do indeed dominate the transport phenomenology of SiO_2 supported bilayer graphene.

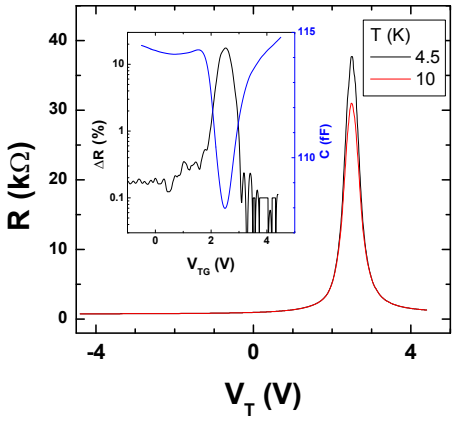

Figure 5.5: Mobility edge in biased bilayer graphene
Resistance traces taken at 4.5 and 10K. Comparing their difference, $\Delta R = R(10K) - R(4.5K)$, with the measured capacitance, shows the correlation between the band-edge singularity and the onset of localization.

The vHs feature is only present on one edge of the band gap, appearing on the electron side for $\overline{D} > 0$ and the hole side for $\overline{D} < 0$. This inversion symmetry in the variables ($\overline{D}$,n) was observed

in all devices measured, including those fabricated using a resist free shadow mask deposition as well as seeded atomic layer deposition of HfO_2 [80]. Understanding this asymmetry requires taking into account the three dimensional structure of BLG [28], which consists of two strongly coupled but spatially distinct layers of carbon atoms. The charge distribution on a BLG flake is sharply concentrated on the two layers, $n(z) \simeq n_1\delta(z) + n_2\delta(z+d)$, so that the system can be modeled as a four plate capacitor shown. A detailed solution of this electrostatic problem, and some of its implications, are presented in the next section. For the purposes of understanding the extant experimental data, the salient result is that the 3D model leads to a modified relation for the measured capacitance,

$$C_T = C_T^0 \left(1 - \frac{\det(\hat{C}) - C_B^0\nu_{21} + C_T^0\nu_{22}}{\det(\hat{\nu} + \hat{C})}\right), \tag{5.3}$$

where $\nu_{ij} = \partial n_i/\partial v_j$, $i,j = 1,2$ is the matrix of intra- and inter-layer compressibilities, and $\hat{C}$ is a constant matrix whose elements are combinations of the geometric capacitances C_B^0,C_T^0, and $C_{BL} \sim 26fF/\mu m^2$. Eq. 5.2 amounts to the large C_{BL} limit of Eq. , corresponding to a perfectly two dimensional system.

The relevant feature of Eq. 5.1 is that while ν_{21} is symmetric with respect to layer interchange, $\frac{\partial n_2}{\partial v_2}$ is obviously asymmetric in the presence of interlayer asymmetry. Notably, penetration field [79] measurements of bilayer graphene depend only on layer-symmetric quantities, and thus probe fundamentally different physical quantities. As elaborated in the next section, the $1/\sqrt{\varepsilon}$ divergence associated with the 1D vHs at the band edge 'lives' on the low energy layer within the BLG flake. The vHs manifests more strongly in the measured capacitance when vHs-hosting layer is closest to the top gate; conversely, the gate sees a far-layer vHs only through the screened field

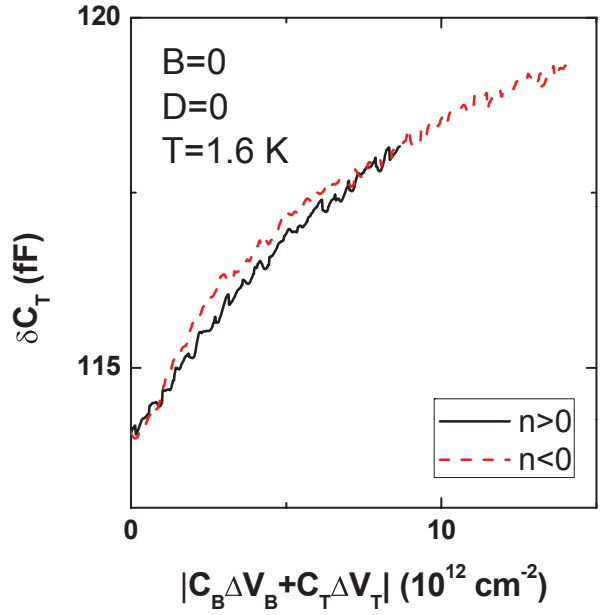

Figure 5.6: Electron-hole symmetry of capacitance for $\overline{D} = 0$
Capacitance traces for $\overline{D} = 0$, used in the background subtraction in Fig 5.7. No noticeable electron-hole is observed, in contrast to the results of Herniksen and Eisenstein.[79]

penetrating the near layer. Counterintuitively, disorder enhances this effect not only by smearing the total density of states [222, 223] but by populating the normally depleted non-vHs layer, thereby enhancing its ability to screen. While an ideal experimental geometry would permit the simultaneous measurement of capacitance from two sides of the BLG flake this is effectively accomplished in our single local gate geometry by reversing the sign of $\overline{D}$, thus reversing the order of the vHs bearing and non-bearing layers.

In order to better compare our experimental data with theory based on a parabolic two band model, it is convenient to subtract a background taken at $\overline{D} = 0$ (see Fig.). Because the high energy behavior depends only weakly on the displacement, this has the effect of isolating the low

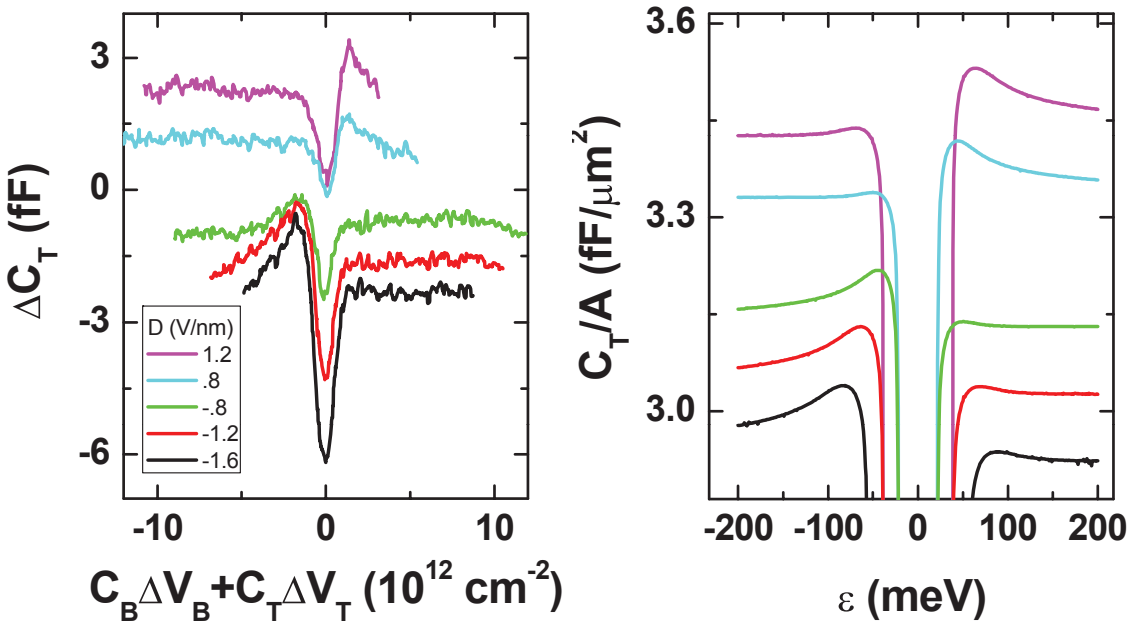

Figure 5.7: Comparison of background-subtracted data with the NLCE model
(a) Subtracted capacitance, $\Delta C_T = C_T(\overline{D}) - C_T(\overline{D} = 0)$, as a function of approximate density for different applied displacements. (b) Calculated top gate capacitance for disordered bilayer graphene, following the discussion given in [28]. The colors correspond to the displacements in (a); the disorder parameter is $\gamma = 4$ for all curves.

energy part of the measured capacitance. The results of this subtraction resemble theoretical calculations which take into account both the interlayer separation as well as weak, short-range disorder (Fig. 5.7). In particular, the asymmetric appearance of the van Hove singularity can be understood as the effect of disorder enhanced interlayer screening. However, quantitative understanding of the role of disorder in bilayer graphene will require experiments that independently control the disorder, as well as a more sophisticated theory taking into account a wider variety of effects including long range scattering and electron-electron interactions.

5.2 Capacitance of bilayer graphene as a which-layer probe

In this section I will discuss the unique capabilities of capacitance measurements in BLG. Due to the finite interlayer separation, capacitance measurements can probe layer-specific properties that are out of reach in conventional transport measurements in which the layers are not contacted separately. These calculations were motivated by the preliminary experiments detailed in the previous section, and explain one aspect of that data; however, the results obtained suggest several follow up experiments which may be considerably more interesting. In summary, a full calculation allows us to interpret the peculiar electron-hole asymmetry observed in top-gate capacitance measurements in terms of a "near-layer capacitance enhancement", which is a combined effect of van Hove singularities (vHs) in the BLG band structure and the interlayer screening. The implication is that capacitance experiments can be used as a which-layer probe in bilayer graphene, offering a unique capability in probing its electronic properties which may be particularly fruitful in the study of broken symmetry states emerging in the cleanest samples at both zero and finite magnetic fields.

5.2.1 The near-layer capacitance enhancement

The geometry of BLG devices in which capacitance measurements are performed allows the electrostatic potentials on the two layers to be varied independently, enabling independent control of both carrier density and the gap in the electronic spectrum [38, 123, 124]. In the absence of external fields and electronic interactions, BLG is a metal characterized (at sufficiently low energies) by approximately parabolic valence and conduction bands which touch at the corners of the hexagonal Brillouin zone (at the K and K' points). The degeneracy at this band crossing is protected by

the symmetry of the BLG crystal structure, in which atomic sites on different layers are equivalent under transformations of the point symmetry group. Application of an external electric field perpendicular to the layers breaks the which-layer symmetry, turning BLG into a semiconductor with a gate-tunable band gap. At not too strong fields the gapped state can be described[38] by projecting the tight binding Hamiltonian on the low-energy subspace of wavefunctions (ψ_1, ψ_2) where the subscript indicates the layer index, giving the two-band Hamiltonian

$$H_0(\vec{p}) = \begin{pmatrix} v_1 & \frac{p_+^2}{2m} \\ \frac{p_-^2}{2m} & v_2 \end{pmatrix}, \quad p_\pm = p_x \pm i p_y, \tag{5.4}$$

where momentum $\vec{p}$ is measured relative to the K (or K') point and v_1, v_2 are the potentials on each layer, controlled by external gates or dopants. The Hamiltonian (5.4) features a band gap of size $\Delta = |v_1 - v_2|$, and a pair of vHs in the density of states of inverse square root form positioned on either side of the gap at $\varepsilon = v_1$ and $\varepsilon = v_2$.

The field-induced gapped state is characterized by interlayer density imbalance, in which the occupancies of the two layers are very different for $v_1 = v_2$ and for $v_1 \neq v_2$. For the balanced bilayer ($v_1 = v_2$) the wavefunction amplitudes on each layer are equal (up to a phase); however, in the presence of an imbalance ($v_1 \neq v_2$) the amplitudes become unequal. This leads to population imbalance between the two layers,

$$|\psi_{1(2)}(\vec{p})|^2 = \frac{1}{2} \mp \frac{1}{2} \frac{v_1 - v_2}{\sqrt{(p^2/m)^2 + (v_1 - v_2)^2}}, \tag{5.5}$$

with a higher occupancy on the layer which has lower energy. This layer population asymmetry results in a strong asymmetry in the partial (layer specific) densities of states: since each vHs

shows up only in the partial density of states for one of the two layers, the corresponding divergent contribution to compressibility comes only from the vHs-bearing layer, remaining finite for the other layer.

As we discuss in detail below, the layer population asymmetry, Eq.(5.5), manifests itself in capacitance measurements. This is illustrated in Fig.5.8(b), in which top-gate capacitance found using a self-consistent model (see Sec.5.2.3) is plotted as a function of gate voltages $V_{\rm t}$ and $V_{\rm b}$. The enhancement in capacitance associated with the band edge is stronger when the divergent vHs-bearing layer is facing the gate used to measure capacitance (top layer for $C_{\rm t}$ and bottom layer for $C_{\rm b}$ in Fig. 5.8 a). We refer to this behavior as 'near-layer capacitance enhancement' (NLCE). This NLCE effect is seen in the capacitance map shown in Fig.5.8(b): the dark region, corresponds to the insulating state realized when the chemical potential is positioned inside field-induced gap, is bordered on *one* side by a bright fringe corresponding to the NLCE. The markedly different contrast between the van Hove singularity- associated features positioned on either side of the dark region, is associated with the density piling up on the near layer rather than the far one.

This behavior explains the asymmetry observed in top-gate capacitance measurements [[19]], in which a feature identified with the vHs was observed only for electrons (holes) when the high (low) energy layer was nearest the gate from which capacitance was measured. In contrast, no such asymmetry is expected for the capacitance measured using 'penetration field' geometry[79], because the penetration field capacitance is more symmetric than the one-sided (top or bottom) gate capacitance. Indeed, no NLCE-type asymmetry was observed in the measurements reported in Ref.[[79]]. As we shall see, the gate capacitance and the penetration field capacitance measure fundamentally different characteristics of the system. Simultaneous measurements of gate and

penetration field capacitances can thus provide detailed and direct information on layer polarization of the bilayer.

The NLCE effect is sensitive to the form of the vHs, which depends on the specifics of the dispersion relation. The simplest model for BLG, which we focus on below, is that of quartic dispersion, described by the Hamiltonian (5.4). A more detailed analysis [38, 123, 124], based on the four band model, leads to a 'Mexican hat' structure in band dispersion near points K and K'. However, the Mexican hat dispersion and the quartic dispersion both lead to an inverse square-root vHs at the band edge, resulting in essentially identical NLCE effects.

In this section we develop theory of the NLCE effect. In section III we calculate, using a two band model of BLG, layer-indexed densities of states, $\nu_{ij} = -\partial n_i/\partial v_j$, where $i, j, = 1, 2$ refer to the two layers. In section IV we develop a many-body approach that describes interactions of particles in BLG with other particles and also with gate potentials. Using a self-consistent Hartree-type approximation, we derive expressions for several quantities of interest relevant to capacitance measurements in terms of the matrix elements ν_{ij}. We find that different experimental observables exhibit very different behavior. In particular, the gate capacitance exhibits strong particle-hole asymmetry and the NLCE effect (see Fig.1), while the penetration-field capacitance is nearly particle-hole symmetric. In section V, we consider the effect of disorder, and show that the asymmetry persists for relatively high disorder concentrations corresponding to the experimental regime. Finally, we conclude with a discussion of the usefulness of different capacitance measurements in bilayer graphene for probing the layer-pseudospin texture of possible broken symmetry phases.

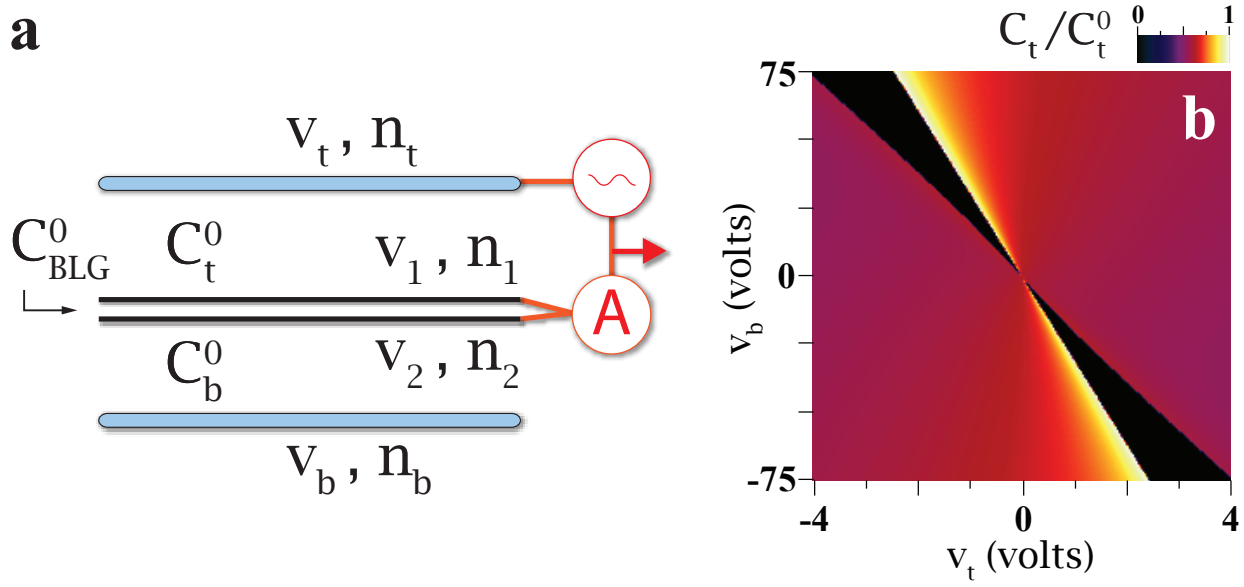

Figure 5.8: Near layer capacitance enhancement (NLCE)
a) Bilayer graphene capacitor schematic. Layer densities (n_1 and n_2) and electrostatic potentials (v_1 and v_2) are controlled by voltages on external gates (v_t and v_b), which couple to the bilayer through the fixed geometric capacitances C_t^0 and C_b^0. Capacitance measurements [19] are performed by measuring the current flowing through *both* layers in the presence of an AC driving potential on one of the gates. b) Top gate capacitance as a function of external gate potentials for a clean bilayer, calculated using the self-consistent approach of Sec.5.2.3 [see Eq.(5.29) as well as Eqs.(5.20)-(5.23) and (5.16)-(5.18)]. The capacitance, which is small in the insulating regime and high in the metallic regime, is enhanced at the edges of the metallic region due to the presence of van Hove singularities in the density of states at the band edge. The enhancement is *asymmetric*, reflecting the asymmetric population of the layers, Eq.(5.5).

5.2.2 van Hove singularities and compressibility in clean bilayer graphene

The main features of the compressibility of BLG in an external field can be understood in terms of the many-body Hamiltonian

$$H = \sum_{\vec{p},\alpha} \psi^\dagger_{\vec{p},\alpha} H_0 \psi_{\vec{p},\alpha} + H_\mathrm{int} \tag{5.6}$$

where H_0 is the single-particle Hamiltonian (5.4) and summation over four flavors $\alpha = 1,2,3,4$ accounts for the spin and valley (K, K') degrees of freedom. The interaction is written in terms of

density harmonics on the layers, $n_{i,\vec{k}} = \sum_{\vec{p},\alpha} \psi^{\dagger}_{i,\vec{p},\alpha}\psi_{i,\vec{p}+\vec{k}}$ $(i = 1, 2)$,

$$H_{\rm int} = \frac{1}{2}\sum_{\vec{k}} \begin{pmatrix} n_{1,-\vec{k}} \\ \\ n_{2,-\vec{k}} \end{pmatrix}^{\rm T} \begin{pmatrix} V_{\vec{k}} & \tilde{V}_{\vec{k}} \\ \\ \tilde{V}_{\vec{k}} & V_{\vec{k}} \end{pmatrix} \begin{pmatrix} n_{1,\vec{k}} \\ \\ n_{2,\vec{k}} \end{pmatrix}, \tag{5.7}$$

with $V_{\vec{k}}$ and $\tilde{V}_{\vec{k}}$ the intralayer and interlayer Coulomb interaction,

$$V_{\vec{k}} = \frac{2\pi e^2}{\kappa|\vec{k}|}, \quad \tilde{V}_{\vec{k}} = e^{-|\vec{k}|d}V_{\vec{k}}, \tag{5.8}$$

where $d \approx 0.3\,{\rm nm}$ is the interlayer spacing in BLG.

We analyze quantum corrections to the capacitance of gated BLG described by the Hamiltonian (5.6) using a Hartree-type approximation. This is done in two steps. We first find the compressibility matrix of non-interacting fermions, formally setting $H_{\rm int} = 0$ in Eq.(5.6). In doing this, the BLG potentials v_1 and v_2 are treated as external parameters. Next, in Sec.5.2.3, we restore the interaction $H_{\rm int}$, adding to it the interaction between all charges, including those on the gates. We relate potentials $v_{1(2)}$ to charges on the gates and the graphene bilayer self-consistently, and use these relations to evaluate capacitance as a function of external gate voltages.

The Hartree-type analysis presented in this paper does not account for correlation effects; however, estimates of the correlation energy and the analysis of compressibility of BLG presented in Ref.[[228]] indicate that the corresponding correction to capacitance is small, except at very low values of disorder and temperature, where the BLG system develops an instability towards a correlated state.

In recent experiments [19, 79] electronic states with different doping relative to the neutrality

point are probed by varying the potentials v_1 and v_2 through their response to the potentials v_t and v_b applied to external gates. Metallic and insulating conductance regimes occur when the Fermi level lies inside or outside the gate-induced gap [82, 208, 209]. The insulating regime was observed to accompany a drop in compressibility.

It is convenient to introduce layer-symmetrized potentials $v_\pm = \frac{1}{2}(v_1 \pm v_2)$. Within the two band model (5.4), the gap size is $\Delta = 2|v_-|$ and the position of the gap center relative to the Fermi level is $v_+ - \mu$; the metallic and insulating regimes in a clean bilayer are then described by $|v_+ - \mu| > |v_-|$ and $|v_+ - \mu| < |v_-|$, respectively. In experiments [19, 79] capacitance was measured with the graphene bilayer grounded. This situation can be described by a Fermi level pinned to zero energy, $\mu = 0$.

Particle densities on the two layers can be expressed as sums over all occupied states,

$$n_{1(2)} = \int \frac{d^2p}{(2\pi\hbar)^2} f(\vec{p}) |\psi_{1(2)}(\vec{p})|^2, \tag{5.9}$$

where $f(\vec{p}) = 1/(e^{\beta\varepsilon(\vec{p})} + 1)$. In what follows, we focus on the case of zero temperature, $f(\vec{p}) = \theta(-\varepsilon(\vec{p}))$. Using the eigenstates of the Hamiltonian (5.4) and defining layer-symmetrized densities $n_\pm = n_1 \pm n_2$, we find

$$n_+ = \begin{cases} -\nu_0 \sqrt{v_+^2 - v_-^2}\, \operatorname{sgn} v_+ & \text{(metal)}, \\ 0 & \text{(insulator)}, \end{cases} \tag{5.10}$$

$$n_- = \begin{cases} -\nu_0 v_- \ln\left(\frac{2\Lambda}{|v_+| + \sqrt{v_+^2 - v_-^2}} \right) & \text{(metal)}, \\ -\nu_0 v_- \ln\left(\frac{2\Lambda}{|v_-|} \right) & \text{(insulator)}, \end{cases} \tag{5.11}$$

where Λ is an ultraviolet cutoff of order the bandwidth. Here $\nu_0 = 2me^2/(\pi\hbar^2)$ accounts for the four-fold spin/valley degeneracy, and can be written as $2/\pi a_B$, where a_B is the Bohr's radius of BLG. The two cases in Eqs.(5.10),(5.11), metallic and insulating, correspond to the regimes $|v_+| > |v_-|$ and $|v_+| < |v_-|$.

Using these expressions we can compute the entries of the compressibility matrix $\nu_{ij} = -\partial n_i/\partial v_j$. The expressions have different form for $|v_+| > |v_-|$ and for $|v_+| < |v_-|$:

$$\nu_{++} = \begin{cases} \nu_0 \frac{|v_+|}{\sqrt{v_+^2 - v_-^2}} & \text{(metal)}, \\ 0 & \text{(insulator)}, \end{cases} \tag{5.12}$$

$$\nu_{--} = \begin{cases} \tilde{\nu}_0 + \nu_0 \frac{|v_+|}{\sqrt{v_+^2 - v_-^2}} & \text{(metal)}, \\ \nu_0 \ln\left(\frac{2\Lambda}{e|v_-|}\right) & \text{(insulator)}, \end{cases} \tag{5.13}$$

$$\nu_{+-} = \nu_{-+} = \begin{cases} -\nu_0 \frac{v_- \operatorname{sgn} v_+}{\sqrt{v_+^2 - v_-^2}} & \text{(metal)}, \\ 0 & \text{(insulator)}, \end{cases} \tag{5.14}$$

where we defined

$$\tilde{\nu}_0 = \nu_0 \ln\left(\frac{2\Lambda}{e\left(|v_+| + \sqrt{v_+^2 - v_-^2}\right)}\right), \tag{5.15}$$

with $e = 2.71828....$ Expressions (5.12)-(5.14) are plotted in the left panel of Fig. 5.9. Note that the compressibility matrix is symmetric, $\nu_{+-} = \nu_{-+}$.

Different elements of matrix $\hat{\nu}$ have different physical meanings. The diagonal element $\nu_{++} = -\partial n_+/\partial v_+$ is the total charge compressibility. The diagonal element $\nu_{--} = -\partial n_-/\partial v_-$ is layer polarizability. The off-diagonal elements $\nu_{-+} = \nu_{+-} = -\partial n_-/\partial v_+$ describe the charge-flavor

response. The latter quantities are particularly useful, as they measure the layer distribution of incremental additions of charge, giving information about the layer polarization of the ground state: the quantities ν_{-+} and ν_{+-} are zero for an unpolarized bilayer, but nonzero in the presence of a charge imbalance.

Rewriting Eqs.(5.10),(5.11) in terms of variables characterizing individual layers, n_1, n_2, we obtain

$$\nu_{11} = \frac{1}{2}\nu_0 \frac{|v_+| - v_- \mathrm{sgn}\, v_+}{\sqrt{v_+^2 - v_-^2}} + \frac{1}{4}\tilde{\nu}_0 \tag{5.16}$$

$$\nu_{22} = \frac{1}{2}\nu_0 \frac{|v_+| + v_- \mathrm{sgn}\, v_+}{\sqrt{v_+^2 - v_-^2}} + \frac{1}{4}\tilde{\nu}_0 \tag{5.17}$$

$$\nu_{12} = \nu_{21} = -\frac{1}{4}\tilde{\nu}_0. \tag{5.18}$$

Expressions (5.16)-(5.18) are invariant under simultaneous $1 \leftrightarrow 2$ exchange and gap inversion, $v_- \to -v_-$.

Both of the diagonal compressibility matrix elements (ν_{11} and ν_{22}) exhibit an inverse square root divergence at the charge gap edge, where the density of single particle states has a van Hove singularity. The two diagonal compressibilities behave *asymmetrically*, diverging on opposite sides of the gap: $\partial n_1/\partial v_1$ diverges at $v_1 \to 0$, while $\partial n_2/\partial v_2$ diverges at $v_2 \to 0$. In contrast, the off-diagonal compressibilities ($i \neq j$) remain finite on either side of the charge gap and are symmetric (see Fig. 5.9, left panel). Inside the charge gap, $|v_+| < |v_-|$, the diagonal and off-diagonal compressibilities are constant:

$$\nu_{11} = \nu_{22} = -\nu_{12} = -\nu_{21} = \frac{\nu_0}{4} \ln\left(\frac{2\Lambda}{e|v_-|}\right), \tag{5.19}$$

exhibiting no divergence at the gap edge.

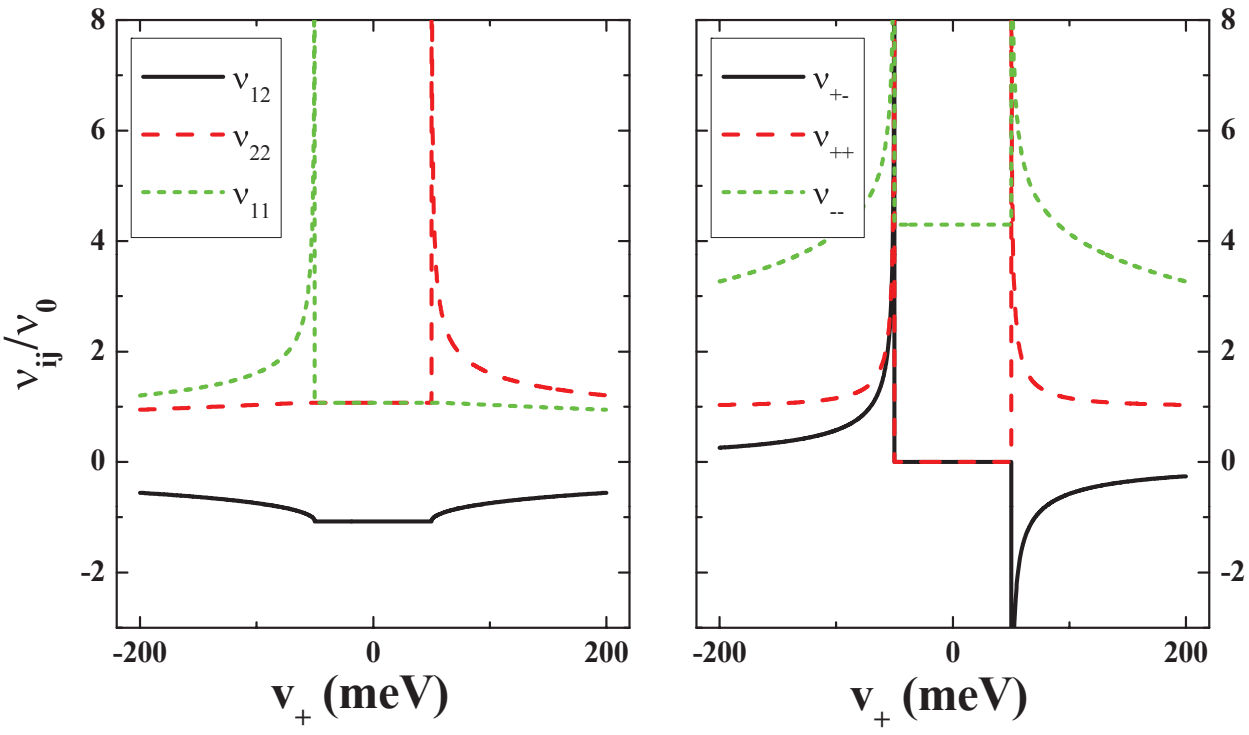

Figure 5.9: Calculated interlayer compressibility matrix elements
Energy dependence of the interlayer compressibility matrix elements ν_{ij} in the 1/2 (left panel, Eqs. (5.16)-(5.18)) and $\nu_{\pm}$ (right panel, Eqs. (5.12)-(5.14)) bases for fixed interlayer asymmetry $v_- = 50\text{meV}$ and $\Lambda = 5\text{eV}$. In the left panel, single layer charge compressibilities ν_{11} and ν_{22} are divergent only on one side of the charge gap, allowing the interlayer asymmetry to be probed by single side capacitance measurements. In the $+/-$ basis, this asymmetry is reflected by the charge-flavor response, ν_{+-}.

5.2.3 Self-consistent capacitance calculation

We shall focus on the geometry pictured in Fig.5.8a, which describes a dual-gated graphene device of the type studied in Refs.[[19]] and [[79]]. The experimental system consists of a bilayer graphene sheet placed between two gates, characterized by potentials $v_{\rm t}$ and $v_{\rm b}$, charge densities

$n_{\rm t}$ and $n_{\rm b}$, and geometric capacitances to the bilayer $C_{\rm t}^0$ and $C_{\rm b}^0$. The bilayer is described by the potentials v_1 and v_2 and charge densities n_1 and n_2 induced by the external gates on the individual layers. Electrostatic energy of the bilayer itself is taken into account by including an interlayer capacitance $C_{\rm BLG}$, which can be estimated from the "geometric" value obtained for a parallel plate capacitor, $C_{\rm BLG} = (4\pi d)^{-1}$, with $d \approx 0.3\,{\rm nm}$. This electrostatic model amounts to the approximation that the charge density on the bilayer is of the for m $n(z) = n_1\delta(z-d/2)+n_2\delta(z+d/2)$. While corrections are expected due to the finite extent of the wavefunctions, these corrections amount, for the most part, to a renormalization of $C_{\rm BLG}$, upon which our results do not sensitively depend.

The quantities of interest obey the general electrostatic charge field relations

$$C_{\rm t}^0(v_{\rm t} - v_1) = \frac{1}{2}\left(n_{\rm t} - n_1 - n_2 - n_{\rm b}\right), \tag{5.20}$$

$$C_{\rm BLG}^0(v_1 - v_2) = \frac{1}{2}\left(n_{\rm t} + n_1 - n_2 - n_{\rm b}\right), \tag{5.21}$$

$$C_{\rm b}^0(v_2 - v_{\rm b}) = \frac{1}{2}\left(n_{\rm t} + n_1 + n_2 - n_{\rm b}\right), \tag{5.22}$$

$$n_{\rm t} + n_1 + n_2 + n_{\rm b} = 0. \tag{5.23}$$

To complete the system of equations for charge densities and potentials, a set of constitutive relations for BLG must be used. These relations, which are of general form $n_1 = f_1(v_1, v_2)$, $n_2 = f_2(v_1, v_2)$, will be calculated in subsequent sections.

Capacitance measurements are done in the finite frequency regime, by applying a small AC bias (on top of the DC bias used to control density and interlayer imbalance) to one terminal of the device and then recording the resulting change in charge density on a second terminal. Choice of

terminals distinguishes top (back) gate capacitance, $C_{\mathrm{t(b)}}$, from penetration field capacitance, C_{p},

$$C_{\mathrm{t(b)}} = -\left.\frac{\delta n_1 + \delta n_2}{\delta v_{\mathrm{t(b)}}}\right|_{\delta v_{\mathrm{b(t)}}=0}; \quad C_{\mathrm{p}} = -\left.\frac{\delta n_{\mathrm{t}}}{\delta v_{\mathrm{b}}}\right|_{\delta v_{\mathrm{t}}=0}. \tag{5.24}$$

After eliminating n_{t} and n_{b} from Eqs. (5.20)-(5.23) by expressing them in terms of other variables, $n_{\mathrm{t}} = C_{\mathrm{t}}^0(v_{\mathrm{t}} - v_1)$, $n_{\mathrm{b}} = C_{\mathrm{b}}^0(v_{\mathrm{b}} - v_2)$, the remaining two equations are linearized with the help of the matrix of inter- and intralayer compressibilities

$$\hat{\nu} = -\begin{pmatrix} \frac{\partial n_1}{\partial v_1} & \frac{\partial n_1}{\partial v_2} \\ \frac{\partial n_2}{\partial v_1} & \frac{\partial n_2}{\partial v_2} \end{pmatrix}, \quad \begin{pmatrix} \delta n_1 \\ \delta n_2 \end{pmatrix} = -\hat{\nu}\begin{pmatrix} \delta v_1 \\ \delta v_2 \end{pmatrix}. \tag{5.25}$$

This yields

$$\left[\hat{\nu} + \hat{C}\right]\begin{pmatrix} \delta v_1 \\ \delta v_2 \end{pmatrix} = \begin{pmatrix} C_{\mathrm{t}}^0 \delta v_{\mathrm{t}} \\ C_{\mathrm{b}}^0 \delta v_{\mathrm{b}} \end{pmatrix} \tag{5.26}$$

where $\hat{C}$ is a matrix of geometric capacitances,

$$\hat{C} = \begin{pmatrix} C_{\mathrm{BLG}}^0 + C_{\mathrm{t}}^0 & -C_{\mathrm{BLG}}^0 \\ -C_{\mathrm{BLG}}^0 & C_{\mathrm{BLG}}^0 + C_{\mathrm{b}}^0 \end{pmatrix}. \tag{5.27}$$

These expressions account for both the geometric and 'intrinsic' capacitance of BLG.

Solving for δv_1, δv_2, we find the charges induced on each layer by the gate potentials:

$$\begin{pmatrix} \delta n_1 \\ \delta n_2 \end{pmatrix} = \left[\hat{1} - \hat{C}\left(\hat{\nu} + \hat{C}\right)^{-1}\right]\begin{pmatrix} C_{\mathrm{t}}^0 \delta v_{\mathrm{t}} \\ C_{\mathrm{b}}^0 \delta v_{\mathrm{b}} \end{pmatrix} \tag{5.28}$$

Here the first term describes the geometric capacitance, which would be the only contribution if the electronic system in BLG was infinitely compressible, $\hat{\nu} \to \infty$. The term proportional to $-\hat{C}(\hat{\nu}+\hat{C})^{-1}$ describes the quantum capacitance contribution. Combining equation (5.28) with the relations for $n_{\rm t}$ and $n_{\rm b}$, all three capacitance observables can be calculated:

$$C_{\rm t} = C_{\rm t}^0 \left(1 - \frac{\det(\hat{C}) - C_{\rm b}^0\nu_{21} + C_{\rm t}^0\nu_{22}}{\det(\hat{\nu}+\hat{C})}\right) \tag{5.29}$$

$$C_{\rm b} = C_{\rm b}^0 \left(1 - \frac{\det(\hat{C}) - C_{\rm t}^0\nu_{12} + C_{\rm b}^0\nu_{11}}{\det(\hat{\nu}+\hat{C})}\right) \tag{5.30}$$

$$C_{\rm p} = \frac{C_{\rm b}^0 C_{\rm t}^0}{\det(\hat{\nu}+\hat{C})}\left(C_{\rm BLG}^0 - \nu_{21}\right). \tag{5.31}$$

These quantities implicitly depend on the gate potentials through the compressibility matrix ν_{ij}.

Notably, different capacitance observables depend on different combinations of the compressibility matrix elements, and obey different symmetries. The penetration field capacitance $C_{\rm p}$ is dominated by the off diagonal component of the (necessarily symmetric) compressibility matrix. As a result, for a symmetric device ($C_{\rm b}^0 = C_{\rm t}^0$) it is invariant under interchanging layers 1 and 2 and therefore does not exhibit the NLCE effect. In contrast, the expressions for $C_{\rm b}$ and $C_{\rm t}$ are not $1 \leftrightarrow 2$ invariant. In particular, the last term in the expression for $C_{\rm t}$, proportional to ν_{22}, changes to ν_{11} upon layer permutation. As shown in the previous section, in the presence of a layer imbalance these two quantities are not the same, leading to the observed NLCE observed in Ref.[19].

In a device in which all capacitances can be measured, combinations of the measured quantities can be combined to probe the charge-flavor response. For the simplest case of a symmetric gate configuration ($C_{\rm b}^0 = C_{\rm t}^0$),

$$\frac{C_{\rm t} - C_{\rm b}}{C_{\rm p}} = \frac{4\nu_{-+}}{4C_{\rm BLG}^0 + \nu_{--} - \nu_{++}}. \tag{5.32}$$

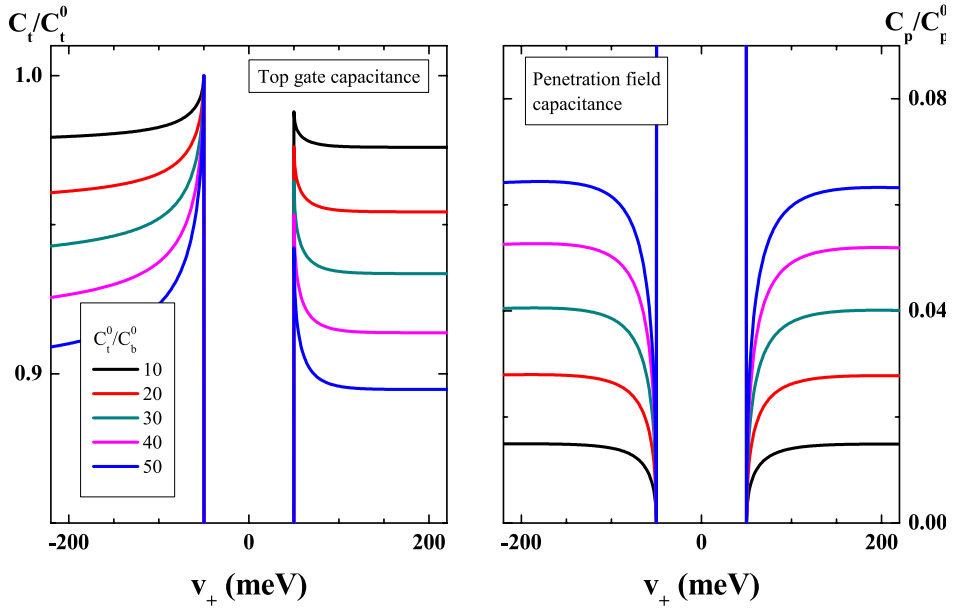

Figure 5.10: Top gate and penetration field capacitance calculated for the clean bilayer Different color traces correspond to different values of the top gate geometric capacitance, measured relative to a fixed $C_{\rm b}^0$ (taken to be 120 aF/μm^2 corresponding to the standard 285 nm SiO_2). Penetration field traces are normalized by the geometric value corresponding to full penetration, $C_{\rm p}^0 = (1/C_{\rm b}^0 + 1/C_{\rm BLG}^0 + 1/C_{\rm t}^0)^{-1}$.

Because this quantity is proportional to ν_{-+}, it can be used to probe both gate-induced and spontaneous layer polarization, allowing direct experimental measurement—somewhat analogous to Knight Shift measurements for spin—of the ground state layer polarization.

5.2.4 The effect of disorder

In the devices used for capacitance measurements in Refs.[[19]],[[79]], graphene flakes were supported by a silica substrate. The carrier mobility in such devices was of order 1,000 cm^2/V sec. For such low-mobility devices, taking into account the effect of disorder is crucial for developing a sensible model of the experimental data. Full quantitative description of experiments requires

including realistic disorder, which is likely long range [222, 229, 230], along with the effects of electronic correlations [231] which can give quantitative corrections to the electronic compressibility. However, the the key features of the data are captured by a simpler short range disorder model [223], which involves delta-function impurities localized on carbon sites:

$$H = \sum_{\vec{p}} \psi^{\dagger}_{\mathbf{p}} H_0 \psi_{\mathbf{p}} + \sum_{\mathbf{x}} u(\mathbf{x}) \psi^{\dagger}_{\mathbf{x}} \psi_{\mathbf{x}}, \tag{5.33}$$

with potential $u(\vec{x}) = \sum_i U\delta(\vec{x} - \vec{x}_i)$ taking values U on the carbon sites occupied by impurities, and zero elsewhere. The impurities are assumed to be distributed randomly with concentration n.

The problem (5.33) can be analyzed using a self-consistent T-matrix approximation (SCTA). The SCTA approach provides a somewhat more general approach than the self-consistent Born approximation, and is reduced to the latter for weak disorder.

We evaluate the DOS and the total energy by employing disorder-averaged Greens functions expressed through the layer-indexed disorder-averaged self-energies Σ_i

$$G(\varepsilon, \vec{p}) = \begin{bmatrix} \varepsilon - v_1 - \Sigma_1 & -t_{\vec{p}} \\ -t^*_{\vec{p}} & \varepsilon - v_2 - \Sigma_2 \end{bmatrix}^{-1}, \tag{5.34}$$

where $\mathrm{t}_{\mathbf{p}}$ is the kinetic energy operator [38, 123, 124], $t_{\vec{k}} \propto (1 + e^{-i\vec{k}\vec{e}_1} + e^{-i\vec{k}\vec{e}_2})^2$. An infinitesimal imaginary part $\pm i0$ should be added to ε to obtain the retarded and advanced Greens functions.

The self-energy is approximated by the average values of the T-matrix, evaluated separately for the sites on layers 1 and 2,

$$\Sigma_1(\varepsilon) = \tilde{n}\langle T_1(\varepsilon)\rangle, \quad \Sigma_2(\varepsilon) = \tilde{n}\langle T_2(\varepsilon)\rangle. \tag{5.35}$$

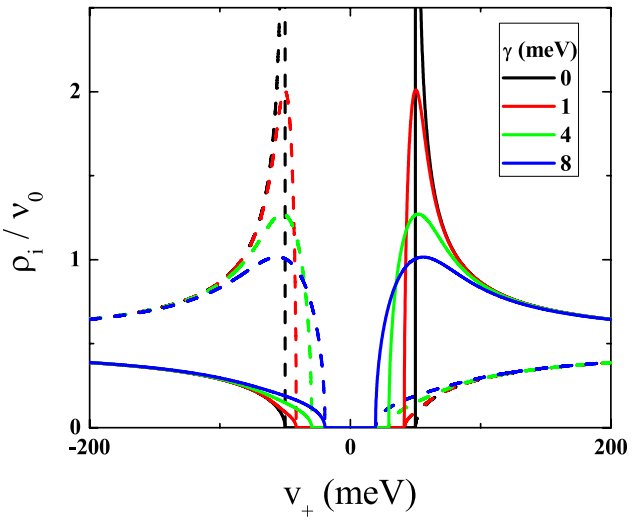

Figure 5.11: The effect of disorder on the density of states
Partial density of states ρ_i, Eq. (5.41) for layers $i = 1$ (solid lines) and $i = 2$ (dashed lines) of a graphene bilayer, obtained from the self-consistent Born approximation, Eqs.(5.39),(5.40). Increasing the disorder strength leads to smearing of van Hove singularities and, eventually a closing of the energy gap.

Here $\tilde{n} = n\rho_0$ is the adatom density with $\rho_0 = 2/3\sqrt{3}a^2$ the density of type 1 sites. The quantities $T_{1(2)}$, written as a 2×2 matrix, are given by

$$\begin{bmatrix} T_1 & 0 \\ 0 & T_2 \end{bmatrix} = \frac{\tilde{U}}{1 - \tilde{U}g}, \; g = \int \frac{d^2p}{(2\pi)^2} G(\varepsilon, \vec{p}), \tag{5.36}$$

where $\tilde{U} = U/\rho_0$. For realistic values of v_1 and v_2 the integral of the Greens function over the Brillouin zone is dominated by the regions near K and K'; approximating $t_{\vec{p}} \approx (p_x \pm ip_y)^2/2m$, we obtain

$$g = \frac{-im}{2\sqrt{\varepsilon_1 \varepsilon_2}} \begin{bmatrix} \varepsilon_2 & 0 \\ 0 & \varepsilon_1 \end{bmatrix}, \quad \varepsilon_{1(2)} = \varepsilon - v_{1(2)} - \Sigma_{1(2)}(\varepsilon). \tag{5.37}$$

This expression is valid for $\varepsilon_{1(2)}$ small compared to the bandwidth. Combining this result with Eq.(5.35), we obtain two coupled equations for ε_1, ε_2:

$$\varepsilon_1 = \varepsilon - v_1 - \frac{nU}{1+i\beta/\lambda(\varepsilon)},\ \varepsilon_2 = \varepsilon - v_2 - \frac{nU}{1+i\beta\lambda(\varepsilon)}, \tag{5.38}$$

where we defined $\lambda(\varepsilon) = \sqrt{\varepsilon_1/\varepsilon_2}$ and $\beta = m\tilde{U}/2$.

Solving these equations for ε_1, ε_2 as a function of ε, we find the Greens function (5.34) and use it to calculate the density of states,

$$\rho(\varepsilon) = \frac{1}{\pi}\mathrm{Im}\int G(\varepsilon+i0,\vec{p})\frac{d^2p}{(2\pi)^2} = \frac{m}{\pi}\begin{bmatrix} \lambda^{-1}(\varepsilon) & 0 \\ 0 & \lambda(\varepsilon) \end{bmatrix}, \tag{5.39}$$

where the integral is identical to the one in Eq.(5.37). A factor of two was inserted after integration to account for spin degeneracy.

The density of states is expressed through the quantity $\lambda(\varepsilon)$. Taking the ratio of the self-consistent equations for ε_1 and ε_2, Eq.(5.38), we obtain a single equation for the quantity λ. Focusing on the case of weak disorder potential and expanding in U, we arrive at

$$\lambda^2 = \frac{\varepsilon - v_1 + i\gamma/\lambda}{\varepsilon - v_2 + i\gamma\lambda}, \quad \gamma = \frac{mU^2}{2\rho_0}n, \tag{5.40}$$

where the terms linear in U have been incorporated in the quantities $v_{1(2)}$. Once $\lambda(\varepsilon)$ is found from Eq.(5.40), it can be plugged into Eq.(5.39) to obtain partial densities of states on each of the layers (see Fig.5.10),

$$\rho_1(\varepsilon) = \frac{\nu_0}{2}\mathrm{Re}\,\lambda^{-1}, \quad \rho_2(\varepsilon) = \frac{\nu_0}{2}\mathrm{Re}\,\lambda. \tag{5.41}$$

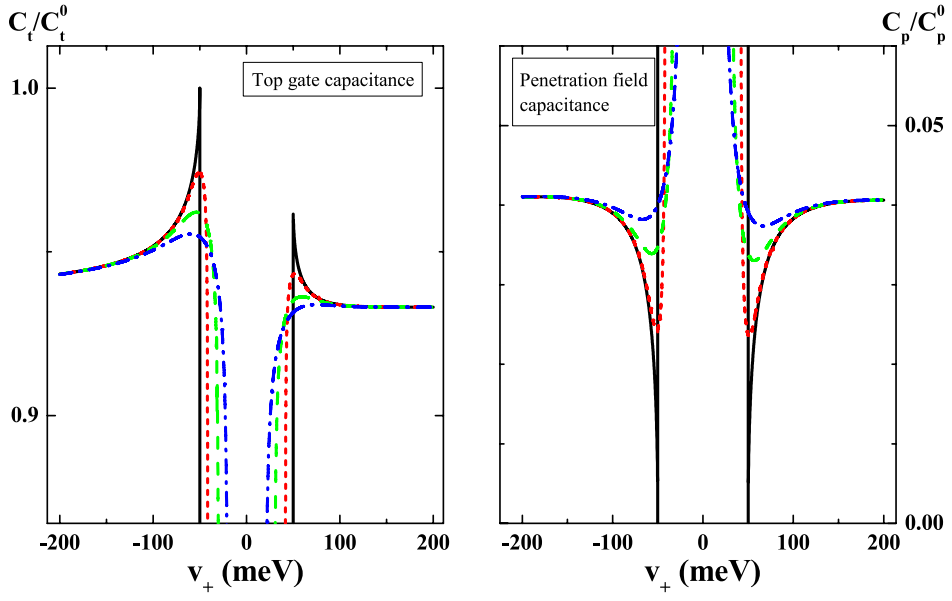

Figure 5.12: The effect of disorder on $C_{\rm t}$ and $C_{\rm p}$
Top gate (left panel) and penetration field (right panel) capacitance for different values of the short-range disorder parameter γ, here measured in meV. Interlayer asymmetry parameter $v_- = 50\text{meV}$ and the cutoff $\Lambda = 5\text{eV}$. Geometric parameters are chosen to match experiment reported in Ref.[[19]], $C_{\rm t}^0/C_{\rm b}^0 = 30$, $C_{\rm b}^0 = 120\text{aF}/\mu\text{m}^2$. Color scheme corresponds to varying values of γ as in Fig. 5.11.

In the absence of disorder, $\gamma = 0$, we have $\lambda = \sqrt{(\varepsilon - v_1)/(\varepsilon - v_2)}$, which gives van Hove singularities of an inverse square root form at the band edges $\varepsilon = v_1, v_2$ as found in section I. In the presence of disorder, these singularities are washed out to varying degrees. As shown in Fig.5.11, this washing out proceeds by both reducing the height of the vHs peak and closing the gap. Crucially, the 'off'-layer density of states at the energy of the 'on' layer vHs peak increases with disorder. This has the effect of increasing the screening effect of the 'off' layer when it lies closer to the gate used to measure capacitance, *enhancing* the NLCE effect for disordered samples.

To calculate experimental capacitances, Eqs. (5.30)-(5.31), the partial densities of states are

integrated numerically with respect to energy and then redifferentiated with respect to the appropriate energy variable, v_1 or v_2. In Figure 5.12, the results for both top gate and penetration field capacitance for a device with electrostatic parameters resembling those in Ref.[19] are plotted. The asymmetry of top gate capacitance survives disorder averaging, and indeed is enhanced. For intermediate values of disorder, electrons and holes display qualitatively different behavior: the non-monotonic vHs feature survives for holes but is completely obliterated for electrons, as observed in Ref.[19].

5.2.5 Conclusions

As we argue above, electrostatic capacitance measurements offer a unique which-layer probe for BLG. The sensitivity to the interlayer imbalance arises despite the fact that the layers are not contacted separately: the relative proximity of the layers to the top- and bottom- gates, combined with the interlayer screening, allows capacitance measurements to access layer specific quantities. Gate capacitance measurements preferentially probe the nearer layer, leading to the NLCE effect as the near layer screens the far layer. Consequently, in the presence of a layer imbalance, top- and bottom- gate capacitance measurements will be different. This difference is the signature of layer polarization, allowing its unambiguous experimental determination.

Our analysis provides an explanation of recent top gate capacitance experiments on dual gate bilayer graphene structures [19, 79]. Since the degeneracy of the band crossing in the BLG spectrum at the K and K' points is linked to inversion symmetry, the gate-induced density imbalance and the opening of a band gap go hand in hand [38, 123, 124]. As we have shown, this imbalance can be probed directly through NLCE measurements; to our knowledge, the NLCE-type asymmetry observed in Ref.[19] is the first direct experimental evidence of layer imbalance in BLG.

The possibility of probing layer polarization directly through capacitance measurements has implications beyond the study of gate-induced gap opening. Recently, experimental sample quality has improved to the point of allowing the observation of a multitude of novel features likely associated with electronic correlations [40, 121, 125, 195, 196]. A large number of possible broken symmetry states, arising in the presence and in the absence of magnetic field, have been explored in the theoretical literature [41, 201, 228, 232–237], including several mutually exclusive scenarios for the ordering at low densities and small electric and magnetic fields. The main open questions pertaining to these states have to do with identifying broken symmetries and determining the exact structure of the order parameter and excitations. Future NLCE measurements, by offering a direct method for determination of the layer polarization, will help to narrow down the possibilities for these new states. A small step towards that goal is depicted in Fig. 5.13, which shows a proof-of-principle device in which top gate and penetration field capacitances can be measured. Given current limitations on the fabrication of high-mobility graphene-hBN heterostructures, it seems likely that real progress will require more sensitive measurements, either through the use of one or more stages of cold amplifiers[238] or quantum dot based charge sensing[239, 240].

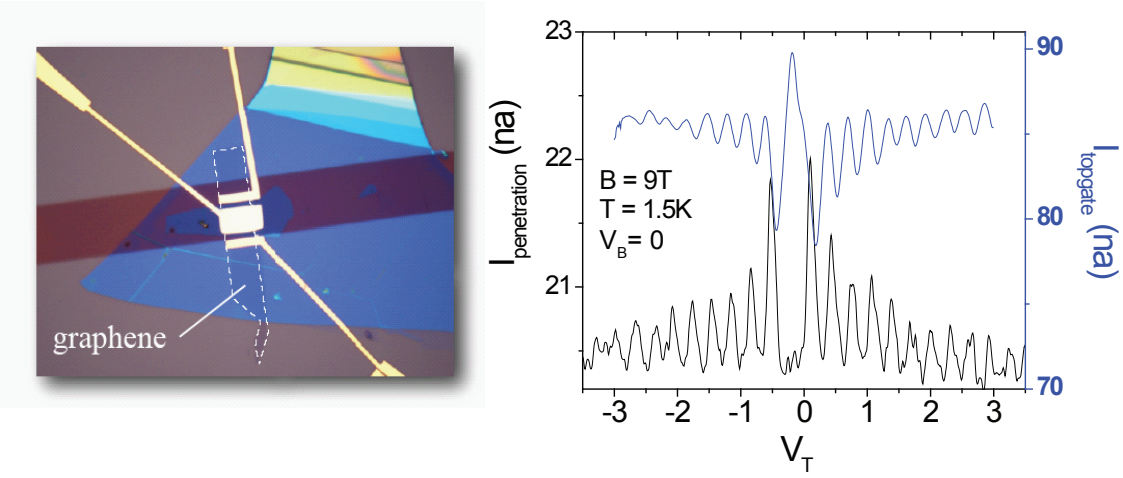

Figure 5.13: Towards NLCE as an experimental tool

Dual local gated hBN encapsulated BLG device (left panel). The hBN-BLG-hBN sandwich structure sits atoop a AuPd local gate, allowing both top-gate and penetration field measurements. This device is far from optimized, with significant undesired parasitics (including to the singly gated regions of the graphene). Although broken symmetry states did not appear at available magnetic fields of 9T, Landau levels are much clearer than in SiO_2 (right panel). The two curves show current from the top gate in in the top gate and penetration field geometries, demonstrating the feasibility of this device architecture. Due to poorly characterized parasitics, however, interlayer compressibilities were not extracted.

Appendix A

Appendix I

Activation data from broken symmetry integer quantum Hall states This section contains Arrhenius plots for the activation gaps discussed in chapter 3.

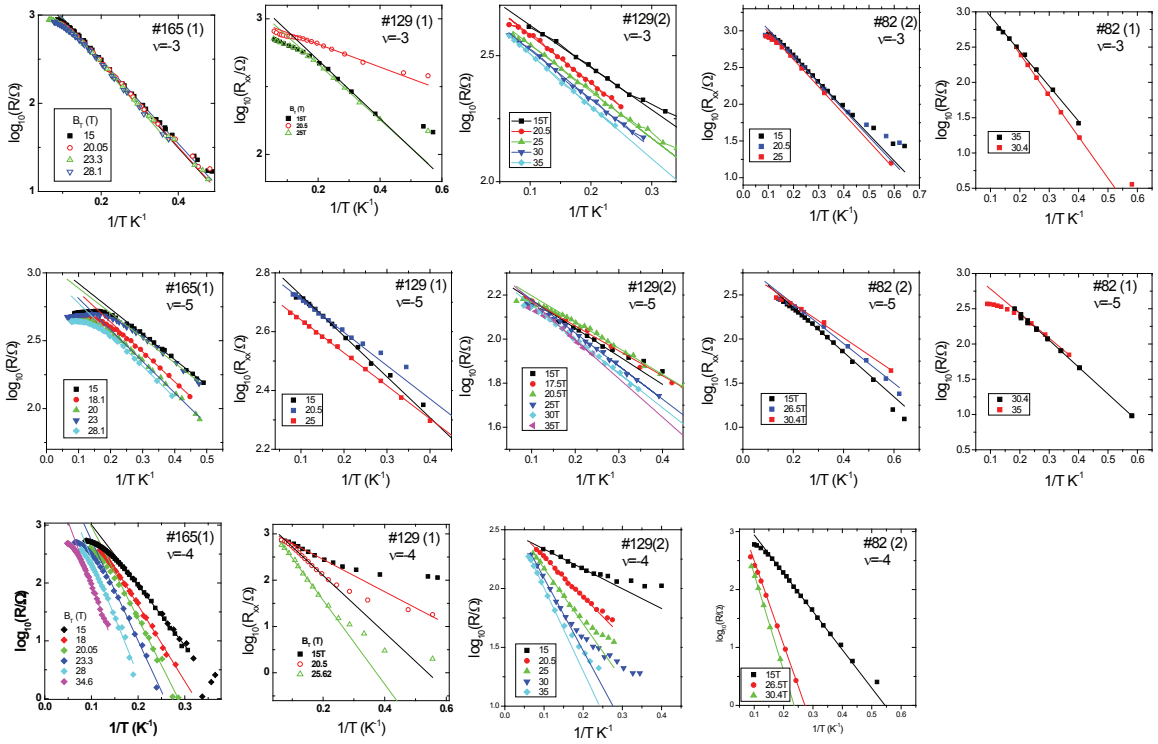

Figure A.1: Arrhenius plots I. Tilted field data for $B_\perp$=15 at ν=-3,=-4,-5.

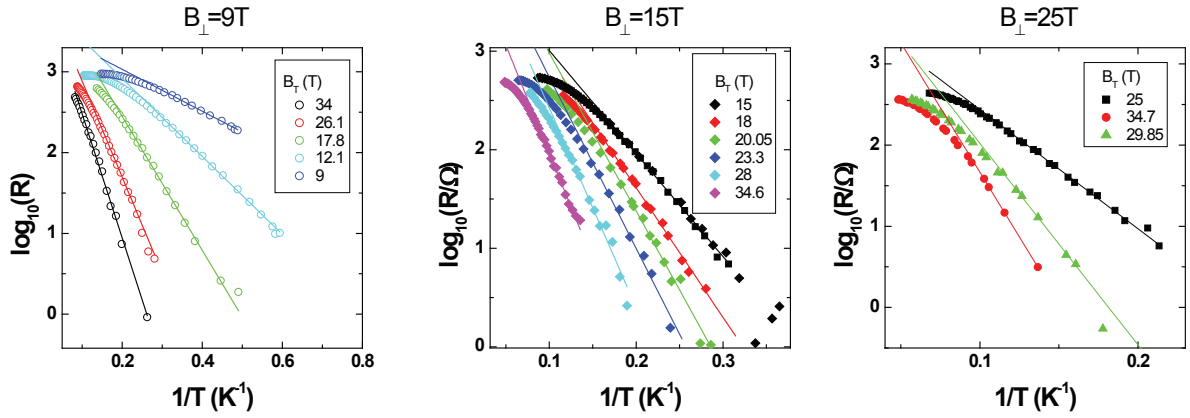

Figure A.2: Arrhenius plots II. Tilted field data for ν=-4 at $B_\perp$=9, 15, and 25 T.

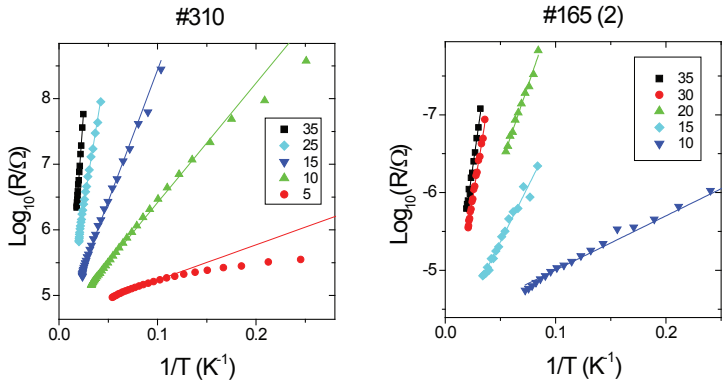

Figure A.3: Arrhenius plots III. Perpendicular field dependence of ν=0 for two devices.

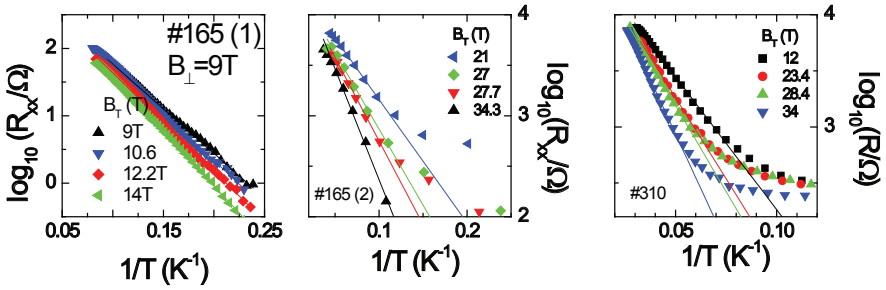

Figure A.4: Arrhenius plots III. Tilted field dependence of the ν=-1 for two devices, with two cooldowns for one of the devices.

Bibliography

[1] I. Meric, N. Baklitskaya, P. Kim, and K. Shepard, in Electron Devices Meeting, 2008. IEDM 2008. IEEE International DOI - 10.1109/IEDM.2008.4796738 (PUBLISHER, ADDRESS, 2008), pp. 1–4.

[2] J. C. Meyer, C. O. Girit, M. F. Crommie, and A. Zettl, Nature **454**, 319 (2008).

[3] D. Sui, Y. Huang, L. Huang, J. Liang, Y. Ma, and Y. Chen, Small **7**, 3186 (2011).

[4] Y. Zhang, Y.-W. Tan, H. L. Stormer, and P. Kim, Nature **438**, 201 (2005).

[5] K. S. Novoselov, A. K. Geim, S. V. Morozov, D. Jiang, M. I. Katsnelson, I. V. Grigorieva, S. V. Dubonos, and A. A. Firsov, Nature **438**, 197 (2005).

[6] S. Das Sarma, S. Adam, E. H. Hwang, and E. Rossi, Rev. Mod. Phys. **83**, (2011).

[7] A. H. Castro Neto, F. Guinea, N. M. R. Peres, K. S. Novoselov, and A. K. Geim, Reviews of Modern Physics **81**, 109 (2009).

[8] E. Stolyarova, K. T. Rim, S. M. Ryu, J. Maultzsch, P. Kim, L. E. Brus, T. F. Heinz, M. S. Hybertsen, and G. W. Flynn, Proceedings of the National Academy of Sciences of the United States of America **104**, 9209 (2007).

[9] M. Ishigami, J. H. Chen, W. G. Cullen, M. S. Fuhrer, and E. D. Williams, Nano Letters **7**, 1643 (2007).

[10] A. F. Young and P. Kim, Nat Phys **5**, 222 (2009).

[11] A. F. Young and P. Kim, Annu. Rev. Condens. Matter Phys. (2010).

[12] T. Ando and T. Nakanishi, Journal of the Physical Society of Japan **67**, 1704 (1998).

[13] N. Gu, M. Rudner, A. Young, P. Kim, and L. Levitov, Phys. Rev. Lett. **106**, 066601 (2011).

[14] I. Meric, M. Y. Han, A. F. Young, B. Özyilmaz, P. Kim, and K. L. Shepard, Nature Nanotechnology **3**, 654 (2008).

[15] I. Meric, C. Dean, A. Young, J. Hone, P. Kim, and K. Shepard, in Electron Devices Meeting (IEDM), 2010 IEEE International DOI - 10.1109/IEDM.2010.5703419 (PUBLISHER, ADDRESS, 2010), pp. 23.2.1–23.2.4.

[16] K. Watanabe, T. Taniguchi, and H. Kanda, Nat Mater **3**, 404 (2004).

[17] C. Lee, Q. Li, W. Kalb, X.-Z. Liu, H. Berger, R. W. Carpick, and J. Hone, Science **328**, 76 (2010).

[18] C. R. Dean, B. A. Piot, P. Hayden, S. Das Sarma, G. Gervais, L. N. Pfeiffer, and K. W. West, Phys. Rev. Lett. **101**, 186806 (2008).

[19] A. F. Young, C. R. Dean, I. Meric, S. Sorgenfrei, H. Ren, K. Watanabe, T. Taniguchi, J. Hone, K. L. Shepard, and P. Kim, arxiv:1004.5556 (2010).

[20] J. Alicea and M. P. A. Fisher, Phys. Rev. B **74**, 075422 (2006).

[21] K. Nomura and A. H. MacDonald, Phys. Rev. Lett. **96**, 256602 (2006).

[22] L. Landau and E. M. Lifshitz, Quantum Mechanics (Non-relativistic Theory), 3rd ed. (Butterworth-Heineman, ADDRESS, 1977), trans. J. B. Sykes and J. S. Bell.

[23] D. C. Tsui, H. L. Stormer, and A. C. Gossard, Phys. Rev. Lett. **48**, 1559 (1982).

[24] Y. Zhang, Z. Jiang, J. P. Small, M. S. Purewal, Y.-W. Tan, M. Fazlollahi, J. D. Chudow, J. A. Jaszczak, H. L. Stormer, and P. Kim, Phys. Rev. Lett. **96**, 136806 (2006).

[25] M. Bird, S. Bole, I. Dixon, Y. Eyssa, B. Gao, and H. Schneider-Muntau, Physica B: Condensed Matter **294-295**, 639 (2001).

[26] A. Young, C. Dean, L. Wang, H. Ren, J. Hone, K. Shepard, and P. Kim, In prepartion .

[27] C. R. Dean, A. F. Young, P. Cadden-Zimansky, L. Wang, H. Ren, K. Watanabe, T. Taniguchi, P. Kim, J. Hone, and K. L. Shepard, Nature Physics **7**, 693 (2011).

[28] A. F. Young and L. S. Levitov, Phys. Rev. B **84**, 085441 (2011).

[29] A. K. Geim and K. S. Novoselov, Nature Materials **6**, 183 (2007).

[30] C. W. J. Beenakker, Rev. Mod. Phys. **80,**, 1337 (2007).

[31] M. O. Goerbig, Rev. Mod. Phys. **83**, 1193 (2011).

[32] N. G. M. K. Andrei Shytov, Mark Rudner and L. Levitov, Sol. State Comm. **149,**, 1087 (2008).

[33] Y. Barlas, K. Yang, and A. Macdonald, arXiv:1110.1069 (2011).

[34] R. Saito, G. Dresselhaus, and M. S. Dresselhaus, Physical Properties of Carbon Nanotubes (Imperial College Press, London, 1989).

[35] P. R. Wallace, Phys. Rev. **71**, 622 (1947).

[36] P. A. M. Dirac, Proceedings of the Royal Society of London. Series A **117**, 610 (1928).

[37] G. W. Semenoff, Phys. Rev. Lett. **53**, 2449 (1984).

[38] E. McCann and V. I. Fal'ko, Phys. Rev. Lett. **96**, 086805 (2006).

[39] P. L. McEuen, M. Bockrath, D. H. Cobden, Y.-G. Yoon, and S. G. Louie, Phys. Rev. Lett. **83**, 5098 (1999).

[40] C. R. Dean, A. F. Young, I. Meric, C. Lee, L. Wang, S. Sorgenfrei, K. Watanabe, T. Taniguchi, P. Kim, K. L. Shepard, and J. Hone, Nature Nanotechnology **5**, 722 (2010).

[41] Y. Barlas, R. Côté, K. Nomura, and A. H. MacDonald, Phys. Rev. Lett. **101**, 097601 (2008).

[42] B. I. Halperin, Helv. Phys. Acta **56**, 75 (1983).

[43] O. Klein, Zeitschrift fur Physik A Hadrons and Nuclei **53**, 157 (1929).

[44] C. D. Anderson, Phys. Rev. **43**, 491 (1933).

[45] F. Sauter, Zeitschrift für Physik A Hadrons and Nuclei **69**, 742 (1931).

[46] A. Calogeracos and N. Dombey, Contemporary Physics **40**, 313 (1999).

[47] M. I. Katsnelson, K. S. Novoselov, and A. K. Geim, Nat Phys **2**, 620 (2006).

[48] V. V. Cheianov, V. I. Falko, B. L. Altshuler, and I. L. Aleiner, Phys. Rev. Lett. **99**, 176801 (2007).

[49] A. V. Shytov, M. I. Katsnelson, and L. S. Levitov, Phys. Rev. Lett. **99**, 246802 (2007).

[50] P. G. Silvestrov and K. B. Efetov, Phys. Rev. B **77**, 155436 (2008).

[51] S. Barraza-Lopez, M. Vanevi, M. Kindermann, and M. Y. Chou, Phys. Rev. Lett. **104**, 076807 (2010).

[52] B. Huard, N. Stander, J. A. Sulpizio, and D. Goldhaber-Gordon, Phys. Rev. B **78**, 121402 (2008).

[53] J. Cayssol, Phys. Rev. Lett. **100**, 147001 (2008).

[54] J. Cayssol, B. Huard, and D. Goldhaber-Gordon, Phys. Rev. B **79**, 075428 (2009).

[55] T. Mueller, F. Xia, M. Freitag, J. Tsang, and P. Avouris, Phys. Rev. B **79**, 245430 (2009).

[56] Y.-M. Lin, C. Dimitrakopoulos, K. A. Jenkins, D. B. Farmer, H.-Y. Chiu, A. Grill, and P. Avouris, Science **327**, 662 (2010).

[57] V. V. Cheianov and V. I. Fal'ko, Phys. Rev. B **74**, 041403 (2006).

[58] B. Huard, J. A. Sulpizio, N. Stander, K. Todd, B. Yang, and D. Goldhaber-Gordon, Phys. Rev. Lett. **98**, 236803 (2007).

[59] J. R. Williams, L. DiCarlo, and C. M. Marcus, Science **317**, 638 (2007).

[60] B. Özyilmaz, P. Jarillo-Herrero, D. Efetov, D. A. Abanin, L. S. Levitov, and P. Kim, Phys. Rev. Lett. **99**, 166804 (2007).

[61] G. Liu, J. Jairo Velasco, W. Bao, and C. N. Lau, Applied Physics Letters **92**, 203103 (2008).

[62] R. V. Gorbachev, A. S. Mayorov, A. K. Savchenko, D. W. Horsell, and F. Guinea, Nano Letters **8**, 1995 (2008).

[63] N. Stander, B. Huard, and D. Goldhaber-Gordon, Phys. Rev. Lett. **102**, 026807 (2009).

[64] C.-H. Park, Y.-W. Son, L. Yang, M. L. Cohen, and S. G. Louie, Nano Letters **8**, 2920 (2008).

[65] J. Milton Pereira, V. Mlinar, F. M. Peeters, and P. Vasilopoulos, Phys. Rev. B **74**, 045424 (2006).

[66] C. Bai and X. Zhang, Phys. Rev. B **76**, 075430 (2007).

[67] J. Milton Pereira, Jr., P. Vasilopoulos, and F. M. Peeters, Appl. Phys. Lett. **90**, 132122 (2007).

[68] C. Bai, Y. Yang, and X. Zhang, Phys. Rev. B **80**, 235423 (2009).

[69] C. Bai, Y. Yang, and X. Zhang, Physica E: Low-dimensional Systems and Nanostructures **42**, 1431 (2010).

[70] J. Milton Pereira, F. M. Peeters, A. Chaves, and G. A. Farias, Semiconductor Science and Technology **25**, 033002 (2010).

[71] E. B. Sonin, Phys. Rev. B **79**, 195438 (2009).

[72] V. Lukose, R. Shankar, and G. Baskaran, Phys. Rev. Lett. **98**, 116802 (2007).

[73] F. Schwierz, Nat Nano **advance online publication**, (2010).

[74] V. G. Veselago, Soviet Physics Uspekhi **10**, 509 (1968).

[75] V. V. Cheianov, V. Fal'ko, and B. L. Altshuler, Science **315**, 1252 (2007).

[76] J. Cserti, A. Plyi, and C. Pterfalvi, Phys. Rev. Lett. **99**, 246801 (2007).

[77] C. Pterfalvi, A. Plyi, and J. Cserti, Phys. Rev. B **80**, 075416 (2009).

[78] M. M. Fogler, D. S. Novikov, L. I. Glazman, and B. I. Shklovskii, Phys. Rev. B **77**, 075420 (2008).

[79] E. A. Henriksen and J. P. Eisenstein, Phys. Rev. B **82**, 041412 (2010).

[80] D. B. Farmer, H.-Y. Chiu, Y.-M. Lin, K. A. Jenkins, F. Xia, and P. Avouris, Nano Letters **9**, 4474 (2009).

[81] K. Zou, X. Hong, D. Keefer, and J. Zhu, (2009).

[82] J. B. Oostinga, H. B. Heersche, X. Liu, A. F. Morpurgo, and L. M. K. Vandersypen, Nature Materials **7**, 151 (2008).

[83] M. F. Craciun, S. Russo, M. Yamamoto, J. B. Oostinga, A. Morpurgo, and S. Tarucha, Nature Nanotechnology **4**, 383 (2009).

[84] B. Özyilmaz, P. Jarillo-Herrero, D. Efetov, and P. Kim, Appl. Phys. Lett. **91,**, 192107 (2007).

[85] W. J. Liang, M. Bockrath, D. Bozovic, J. H. Hafner, M. Tinkham, and H. Park, Nature **411**, 665 (2001).

[86] A. V. Shytov, N. Gu, and L. S. Levitov, (2007).

[87] M. Lemme, T. Echtermeyer, M. Baus, and H. Kurz, Electron Device Letters, IEEE DOI - 10.1109/LED.2007.891668 **28**, 282 (2007).

[88] L. M. Zhang and M. M. Fogler, Phys. Rev. Lett. **100**, 116804 (2008).

[89] S. Ryu, M. Y. Han, J. Maultzsch, T. F. Heinz, P. Kim, M. L. Steigerwald, and L. E. Brus, Nano Letters **8**, 4597 (2008).

[90] K. I. Bolotin, K. J. Sikes, Z. Jiang, M. Klima, G. Fudenberg, J. Hone, P. Kim, and H. L. Stormer, Solid State Communications **146,**, 351 (2008).

[91] W. Kohn, Phys. Rev. **123**, 1242 (1961).

[92] A. Iyengar, J. Wang, H. A. Fertig, and L. Brey, Phys. Rev. B **75**, 125430 (2007).

[93] Y. A. Bychkov and G. Martinez, Phys. Rev. B **77**, 125417 (2008).

[94] E. A. Henriksen, P. Cadden-Zimansky, Z. Jiang, Z. Q. Li, L.-C. Tung, M. E. Schwartz, M. Takita, Y.-J. Wang, P. Kim, and H. L. Stormer, Phys. Rev. Lett. **104**, 067404 (2010).

[95] K. Shizuya, Phys. Rev. B **75**, 245417 (2007).

[96] E. A. Henriksen, Z. Jiang, L.-C. Tung, M. E. Schwartz, M. Takita, Y.-J. Wang, P. Kim, and H. L. Stormer, Phys. Rev. Lett. **100**, 087403 (2008).

[97] F. Keilmann and R. Hillenbrand, Philosophical Transactions of the Royal Society of London **362**, 787 (2004).

[98] S. Sorgenfrei, I. Meric, S. Banerjee, A. Akey, S. Rosenblatt, I. P. Herman, and K. L. Shepard, Appl. Phys. Lett. **94**, 053105 (2009).

[99] N. Gu, M. Rudner, and L. Levitov, Phys. Rev. Lett. **107**, 156603 (2011).

[100] T. Ando, J. Phys. Soc. Jpn. **75**, 074716 (2006).

[101] K. Nomura and A. H. MacDonald, Phys. Rev. Lett. **98**, 076602 (2007).

[102] E. H. Hwang, S. Adam, and S. Das Sarma, Phys. Rev. Lett. **98**, 186806 (2007).

[103] S. Adam, E. H. Hwang, V. Galitski, and S. D. Sarma, Proc. Natl. Acad. Sci. USA **104,**, 18392 (2007).

[104] S. Fratini and F. Guinea, Phys. Rev. B **77**, 195415 (2008).

[105] J.-H. Chen, C. Jang, S. Xiao, M. Ishigami, and M. S. Fuhrer, Nat Nano **3**, 206 (2008).

[106] M. I. Katsnelson and A. K. Geim, Phil. Trans. R. Soc. A **366,**, 195 (2007).

[107] S. V. Morozov, K. S. Novoselov, M. I. Katsnelson, F. Schedin, D. C. Elias, J. A. Jaszczak, and A. K. Geim, Phys. Rev. Lett. **100**, 016602 (2008).

[108] J. Martin, N. Akerman, G. Ulbricht, T. Lohmann, J. H. Smet, K. von Klitzing, and A. Yacoby, Nature Physics **4**, 144 (2008).

[109] K. I. Bolotin, K. J. Sikes, J. Hone, H. L. Stormer, and P. Kim, Phys. Rev. Lett. **101**, 096802 (2008).

[110] X. Du, I. Skachko, A. Barker, and E. Y. Andrei, Nat Nano **3**, 491 (2008).

[111] X. Hong, A. Posadas, K. Zou, C. H. Ahn, and J. Zhu, Phys. Rev. Lett. **102**, 136808 (2009).

[112] L. A. Ponomarenko, R. Yang, T. M. Mohiuddin, M. I. Katsnelson, K. S. Novoselov, S. V. Morozov, A. A. Zhukov, F. Schedin, E. W. Hill, and A. K. Geim, Phys. Rev. Lett. **102**, 206603 (2009).

[113] M. Lafkioti, B. Krauss, T. Lohmann, U. Zschieschang, H. Klauk, K. v. Klitzing, and J. H. Smet, Nano Letters **10**, 1149 (2010).

[114] L. Liao, J. Bai, Y. Qu, Y. Huang, and X. Duan, Nanotechnology **21**, 015705 (2010).

[115] G. Giovannetti, P. A. Khomyakov, G. Brocks, P. J. Kelly, and J. van den Brink, Phys. Rev. B **76**, 073103 (2007).

[116] C. H. Lui, L. Liu, K. F. Mak, G. W. Flynn, and T. F. Heinz, Nature **462**, 339 (2009).

[117] P. Blake, E. W. Hill, A. H. C. Neto, K. S. Novoselov, D. Jiang, R. Yang, T. J. Booth, and A. K. Geim, Applied Physics Letters **91**, 063124 (2007).

[118] T. Taniguchi and K. Watanabe, Journal of Crystal Growth **303**, 525 (2007).

[119] A. Reina, X. Jia, J. Ho, D. Nezich, H. Son, V. Bulovic, M. S. Dresselhaus, and J. Kong, Nano Letters **9**, 30 (2009).

[120] X. Hong, K. Zou, and J. Zhu, Phys. Rev. B **80,**, 241415(2009) (2009).

[121] B. E. Feldman, J. Martin, and A. Yacoby, Nature Physics **5**, 889 (2009).

[122] S. Adam and S. Das Sarma, Phys. Rev. B **77**, 115436 (2008).

[123] E. McCann, Phys. Rev. B **74,**, 161403 (2006).

[124] E. V. Castro, K. S. Novoselov, S. V. Morozov, N. M. R. Peres, J. M. B. L. dos Santos, J. Nilsson, F. Guinea, A. K. Geim, and A. H. C. Neto, Phys. Rev. Lett. **99**, 216802 (2007).

[125] Y. Zhao, P. Cadden-Zimansky, Z. Jiang, and P. Kim, Phys. Rev. Lett. **104**, 066801 (2010).

[126] J. P. Eisenstein and A. H. MacDonald, Nature **432**, 691 (2004).

[127] H. Min, R. Bistritzer, J.-J. Su, and A. H. MacDonald, Phys. Rev. B **78**, 121401 (2008).

[128] M. Y. Kharitonov and K. B. Efetov, Phys. Rev. B **78**, 241401 (2008).

[129] S. M. Girvin, in Ecole d'Ete Les Houches, July 1998 (PUBLISHER, ADDRESS, 1999).

[130] Perspectives in Quantum Hall effects: Novel quantum liquids in low dimensional semiconductor heterostructures, edited by S. Das Sarma and A. Pinczuk (Wiley-VCH, ADDRESS, 1997).

[131] X.-G. Wen, Advances in Physics **44**, 405 (1995).

[132] T. Ando, A. B. Fowler, and F. Stern, Rev. Mod. Phys. **54**, 437 (1982).

[133] Z. F. Ezawa, Quantum Hall Effects: Field Theoretical Approach and Related Topics (World Scientific (Singapore), ADDRESS, 2000).

[134] M. Shayegan, E. P. De Poortere, O. Gunawan, Y. P. Shkolnikov, E. Tutuc, and K. Vakili, phys. stat. sol. (b) **243**, 3629 (2006).

[135] Z. Jiang, E. A. Henriksen, L. C. Tung, Y.-J. Wang, M. E. Schwartz, M. Y. Han, P. Kim, and H. L. Stormer, Phys. Rev. Lett. **98**, 197403 (2007).

[136] J. G. Checkelsky, L. Li, and N. P. Ong, Phys. Rev. Lett. **100**, 206801 (2008).

[137] X. Du, I. Skachko, F. Duerr, A. Luican, and E. Y. Andrei, Nature **462**, 192 (2009).

[138] K. Yang, S. Das Sarma, and A. H. MacDonald, Phys. Rev. B **74**, 075423 (2006).

[139] J. Alicea and M. P. Fisher, Solid State Communications **143**, 504 (2007).

[140] M. O. Goerbig, R. Moessner, and B. Douçot, Phys. Rev. B **74**, 161407 (2006).

[141] R. L. Doretto and C. M. Smith, Phys. Rev. B **76**, 195431 (2007).

[142] L. Sheng, D. N. Sheng, F. D. M. Haldane, and L. Balents, Phys. Rev. Lett. **99**, 196802 (2007).

[143] I. A. Luk'yanchuk and A. M. Bratkovsky, Phys. Rev. Lett. **100**, 176404 (2008).

[144] D. A. Abanin, S. A. Parameswaran, S. A. Kivelson, and S. L. Sondhi, Phys. Rev. B **82**, 035428 (2010).

[145] D. V. Khveshchenko, Phys. Rev. Lett. **87**, 206401 (2001).

[146] E. V. Gorbar, V. P. Gusynin, V. A. Miransky, and I. A. Shovkovy, Phys. Rev. B **66**, 045108 (2002).

[147] D. A. Abanin, P. A. Lee, and L. S. Levitov, Phys. Rev. Lett. **96**, 176803 (2006).

[148] V. P. Gusynin, V. A. Miransky, S. G. Sharapov, and I. A. Shovkovy, Phys. Rev. B **74**, 195429 (2006).

[149] H. A. Fertig and L. Brey, Phys. Rev. Lett. **97**, 116805 (2006).

[150] J.-N. Fuchs and P. Lederer, Phys. Rev. Lett. **98**, 016803 (2007).

[151] I. F. Herbut, Phys. Rev. B **75**, 165411 (2007).

[152] D. A. Abanin, K. S. Novoselov, U. Zeitler, P. A. Lee, A. K. Geim, and L. S. Levitov, Phys. Rev. Lett. **98**, 196806 (2007).

[153] J. Jung and A. H. MacDonald, Phys. Rev. B **80**, 235417 (2009).

[154] K. Nomura, S. Ryu, and D.-H. Lee, Phys. Rev. Lett. **103**, 216801 (2009).

[155] E. Shimshoni, H. A. Fertig, and G. V. Pai, Phys. Rev. Lett. **102**, 206408 (2009).

[156] S. Das Sarma and K. Yang, Solid State Communications **149**, 1502 (2009).

[157] C.-Y. Hou, C. Chamon, and C. Mudry, Phys. Rev. B **81**, 075427 (2010).

[158] M. Kharitonov, arXiv:1105.5386 (2011).

[159] J. G. Checkelsky, L. Li, and N. P. Ong, Phys. Rev. B **79**, 115434 (2009).

[160] L. Zhang, J. Camacho, H. Cao, Y. P. Chen, M. Khodas, D. E. Kharzeev, A. M. Tsvelik, T. Valla, and I. A. Zaliznyak, Phys. Rev. B **80**, 241412 (2009).

[161] K. I. Bolotin, F. Ghahari, M. D. Shulman, H. L. Stormer, and P. Kim, Nature **462**, 196 (2009).

[162] L. Zhang, Y. Zhang, M. Khodas, T. Valla, and I. A. Zaliznyak, Phys. Rev. Lett. **105**, 046804 (2010).

[163] D. A. Abanin, P. A. Lee, and L. S. Levitov, Phys. Rev. Lett. **98**, 156801 (2007).

[164] R. J. H. J. P. Harrang, R. K. Goodall, P. R. Jay, M. Laviron, and P. Delescluse, Phys. Rev. B **32**, 8126 (1985).

[165] P. Coleridge, Phys. Rev. B **44**, 3793 (1991).

[166] E. V. Gorbar, V. P. Gusynin, and V. A. Miransky, **34**, 790 (2008).

[167] I. L. Aleiner, D. E. Kharzeev, and A. M. Tsvelik, Phys. Rev. B **76**, 195415 (2007).

[168] M. König, S. Wiedmann, C. Brüne, A. Roth, H. Buhmann, L. W. Molenkamp, X.-L. Qi, and S.-C. Zhang, Science **318**, 766 (2007).

[169] R. J. Nicholas, R. J. Haug, K. v. Klitzing, and G. Weimann, Phys. Rev. B **37**, 1294 (1988).

[170] S. L. Sondhi, A. Karlhede, S. A. Kivelson, and E. H. Rezayi, Phys. Rev. B **47**, 16419 (1993).

[171] H. A. Fertig, L. Brey, R. Cote;, and A. H. MacDonald, Phys. Rev. B **50**, 11018 (1994).

[172] A. Schmeller, J. P. Eisenstein, L. N. Pfeiffer, and K. W. West, Phys. Rev. Lett. **75**, 4290 (1995).

[173] A. J. Nederveen and Y. V. Nazarov, Phys. Rev. Lett. **82**, 406 (1999).

[174] Z. Papic, M. O. Goerbig, and N. Regnault, Phys. Rev. Lett. **105**, 176802 (2010).

[175] C. Toke and J. K. Jain, (2011).

[176] J. Furneaux, D. Syphers, J. Brooks, G. Schmiedeshoff, R. Wheeler, and P. Stiles, Surface Science **170**, 154 (1986).

[177] S. F. Nelson, K. Ismail, J. J. Nocera, F. F. Fang, E. E. Mendez, J. O. Chu, and B. S. Meyerson, Appl. Phys. Lett. **61**, 64 (1992).

[178] E. P. De Poortere, Y. P. Shkolnikov, E. Tutuc, S. J. Papadakis, M. Shayegan, E. Palm, and T. Murphy, Appl. Phys. Lett. **80**, 1583 (2002).

[179] A. Tsukazaki, S. Akasaka, K. Nakahara, Y. Ohno, H. Ohno, D. Maryenko, A. Ohtomo, and M. Kawasaki, Nat Mater **9**, 889 (2010).

[180] F. D. M. Haldane, Phys. Rev. Lett. **51**, 605 (1983).

[181] V. M. Apalkov and T. Chakraborty, Phys. Rev. Lett. **105**, 036801 (2010).

[182] C. Toke, P. E. Lammert, V. H. Crespi, and J. K. Jain, Phys. Rev. B **74**, 235417 (2006).

[183] V. M. Apalkov and T. Chakraborty, Phys. Rev. Lett. **97**, 126801 (2010).

[184] M. O. Goerbig and N. Regnault, Phys. Rev. B **75**, 241405 (2007).

[185] D. V. Khveshchenko, Phys. Rev. B **75**, 153405 (2007).

[186] C. Toke and J. K. Jain, Phys. Rev. B **75**, 245440 (2007).

[187] N. Shibata and K. Nomura, Phys. Rev. B **77**, 235426 (2008).

[188] N. Shibata and K. Nomura, Journal of the Physical Society of Japan **78**, 104708 (2009).

[189] F. Ghahari, Y. Zhao, P. Cadden-Zimansky, K. Bolotin, and P. Kim, Phys. Rev. Lett. **106**, 046801 (2011).

[190] A. F. Dethlefsen, E. Mariani, H.-P. Tranitz, W. Wegscheider, and R. J. Haug, Phys. Rev. B **74**, 165325 (2006).

[191] A. Kumar, G. A. Csathy, M. J. Manfra, L. N. Pfeiffer, and K. W. West, Phys. Rev. Lett. **105**, 246808 (2010).

[192] M. Padmanabhan, T. Gokmen, and M. Shayegan, Phys. Rev. B **81**, 113301 (2010).

[193] S. Kronmüller, W. Dietsche, K. v. Klitzing, G. Denninger, W. Wegscheider, and M. Bichler, Phys. Rev. Lett. **82**, 4070 (1999).

[194] M. Reznikov, A. Y. Kuntsevich, N. Teneh, and V. M. Pudalov, JETP Letters, **2010,**, Vol.92,No.7,pp.470 (2011).

[195] R. T. Weitz, M. T. Allen, B. E. Feldman, J. Martin, and A. Yacoby, Science **330**, 812 (2010).

[196] J. Martin, B. E. Feldman, R. T. Weitz, M. T. Allen, and A. Yacoby, Phys. Rev. Lett. **105**, 256806 (2010).

[197] J. Velasco, L. Jing, W. Bao, Y. Lee, P. Kratz, V. Aji, M. Bockrath, C. N. Lau, C. Varma, R. Stillwell, D. Smirnov, F. Zhang, J. Jung, and A. H. MacDonald, (2011).

[198] F. Freitag, J. Trbovic, M. Weiss, and C. Schönenberger, arXiv:1104.3816 (2011).

[199] A. S. Mayorov, D. C. Elias, M. Mucha-Kruczynski, R. V. Gorbachev, T. Tudorovskiy, A. Zhukov, S. V. Morozov, M. I. Katsnelson, V. I. Falko, A. K. Geim, and K. S. Novoselov, Science **333**, 860 (2011).

[200] D. A. Abanin, S. A. Parameswaran, and S. L. Sondhi, Phys. Rev. Lett. **103**, 076802 (2009).

[201] R. Cote, W. Luo, B. Petrov, Y. Barlas, and A. H. MacDonald, Phys. Rev. B **82**, 245307 (2010).

[202] V. M. Apalkov and T. Chakraborty, Phys. Rev. Lett. **107**, 186803 (2011).

[203] Z. Papic, D. A. Abanin, Y. Barlas, and R. N. Bhatt, Phys. Rev. B **84**, 241306 (2011).

[204] Z. Papic, R. Thomale, and D. A. Abanin, Phys. Rev. Lett. **107**, 176602 (2011).

[205] T. Ohta, A. Bostwick, T. Seyller, K. Horn, and E. Rotenberg, Science **313**, 951 (2006).

[206] Y. Zhang, T.-T. Tang, C. Girit, Z. Hao, M. C. Martin, A. Zettl, M. F. Crommie, Y. R. Shen, and F. Wang, Nature **459**, 820 (2009).

[207] K. F. Mak, C. H. Lui, J. Shan, and T. F. Heinz, Phys. Rev. Lett. **102**, 256405 (2009).

[208] K. Zou and J. Zhu, Phys. Rev. B **82**, 081407 (2010).

[209] T. Taychatanapat and P. Jarillo-Herrero, Phys. Rev. Lett. **105**, 166601 (2010).

[210] S. Luryi, Applied Physics Letters **52**, 501 (1988).

[211] B. I. S. M. S. Bello, E. I. Levin and A. L. Efros, Sov. Phys JETP **53**, 822 (1981).

[212] J. P. Eisenstein, L. N. Pfeiffer, and K. W. West, Phys. Rev. Lett. **68**, 674 (1992).

[213] J. P. Eisenstein, L. N. Pfeiffer, and K. W. West, Phys. Rev. B **50**, 1760 (1994).

[214] S. Ilani, L. A. K. Donev, M. Kindermann, and P. L. McEuen, Nature Physics **2**, 687 (2006).

[215] S. C. Dultz and H. W. Jiang, Phys. Rev. Lett. **84**, 4689 (2000).

[216] S. Ilani, A. Yacoby, D. Mahalu, and H. Shtrikman, Science **292**, 1354 (2001).

[217] B. Skinner and M. M. Fogler, Phys. Rev. B **82**, 201306 (2010).

[218] L. Li, C. Richter, S. Paetel, T. Kopp, J. Mannhart, and R. C. Ashoori, Science **332**, 825 (2011).

[219] Y. Kubota, K. Watanabe, O. Tsuda, and T. Taniguchi, Science **317**, 932 (2007).

[220] L. Jiao, X. Xian, Z. Wu, J. Zhang, and Z. Liu, Nano Letters **9**, 205 (2009).

[221] D. A. Abanin and L. S. Levitov, Science **317**, 641 (2007).

[222] J. Nilsson and A. H. Castro Neto, Phys. Rev. Lett. **98**, 126801 (2007).

[223] V. V. Mkhitaryan and M. E. Raikh, Phys. Rev. B **78**, 195409 (2008).

[224] P. Van Mieghem, Rev. Mod. Phys. **64**, 755 (1992).

[225] J. Li, I. Martin, M. Buttiker, and A. F. Morpurgo, Nat Phys **7**, 38 (2011).

[226] J. P. Eisenstein, H. L. Stormer, L. N. Pfeiffer, and K. W. West, Phys. Rev. B **41**, 7910 (1990).

[227] B. I. Shklovskii and A. L. Efros, Electronic Properties of Doped Semiconductors (Springer, New York, 1984).

[228] R. Nandkishore and L. Levitov, arXiv:1002.1966 (2010).

[229] J. Nilsson, A. H. Castro Neto, F. Guinea, and N. M. R. Peres, Phys. Rev. B **78**, 045405 (2008).

[230] D. S. L. Abergel, E. H. Hwang, and S. Das Sarma, Phys. Rev. B **83**, 085429 (2011).

[231] G. Borghi, M. Polini, R. Asgari, and A. H. MacDonald, Phys. Rev. B **82**, 155403 (2010).

[232] O. Vafek and K. Yang, Phys. Rev. B **81,**, 041401(2010) (2009).

[233] H. Min, G. Borghi, M. Polini, and A. H. MacDonald, Phys. Rev. B **77**, 041407 (2008).

[234] R. Nandkishore and L. Levitov, Phys. Rev. Lett. **104**, 156803 (2010).

[235] Y. Lemonik, I. L. Aleiner, C. Toke, and V. I. Falko, Phys. Rev. B **82**, 201408 (2010).

[236] J. Jung, F. Zhang, and A. H. MacDonald, Phys. Rev. B **83**, 115408 (2011).

[237] F. Zhang, H. Min, M. Polini, and A. H. MacDonald, Phys. Rev. B **81**, 041402 (2010).

[238] G. Steele, Ph.D. thesis, MIT, 2006.

[239] P. Lafarge, H. Pothier, E. R. Williams, D. Esteve, C. Urbina, and M. H. Devoret, Zeitschrift fr Physik B Condensed Matter **85**, 327 (1991).

[240] D. Berman, Ph.D. thesis, Massachussetts Institute of Technology, 1998.